UNIVERSITY OF CALIFORNIA SAN DIEGO

Exploring the Adsorption of Guest Molecules in Metal-Organic Frameworks: A Many-Body Formalism Approach

A dissertation submitted in partial satisfaction of the
requirements for the degree Doctor of Philosophy

in

Chemistry

by

Ching-Hwa Ho

Committee in charge:

Professor Francesco Paesani, Chair
Professor Michael Galperin
Professor Shyue Ping Ong
Professor Akif Tezcan
Professor Wei Xiong

2024

The Dissertation of Ching-Hwa Ho is approved, and it is acceptable in quality and form for publication on microfilm and electronically.

University of California San Diego

2024

DEDICATION

To my dearest family members, friends, and the land.

EPIGRAPH

Mathematicians do not deal in objects, but in relations among objects; they are free to replace some object by others so long as the relations remain unchanged. Content to them is irrelevant; they are interested in form only.

Henri Poincaré

TABLE OF CONTENTS

LIST OF FIGURES

LIST OF TABLES

ACKNOWLEDGEMENTS

A successful Ph.D. journey does not happen by fighting alone. I would like to acknowledge the many people who have assisted me in completing my dissertation and guided me in my research.

The most important figure in a Ph.D. career is undoubtedly the student's advisor. I am deeply grateful to my advisor, Francesco Paesani, for the efforts, guidance, and patience, which allow me to successfully complete the Ph.D. program. Given the highly competitive environment in academia, I am deeply grateful that Francesco was willing to take the risk and invest in me who had very limited experience in simulations at the time I just joined UC San Diego.

Another important factors associated with Ph.D. career lie in supports from people. I am grateful for the support of all group members in Paesani Lab. In particular, I would like to thank senior members Kelly Hunter, Saswata Dasgupta, Raja Ghosh, Marc Riera, and Kartik Rallapalli for their generous and direct help to my research and career. I would also like to express my gratitude to Professor Martina Lessio and Jierui Zhang at UNSW for the assistance in my research and career.

During my Ph.D. career, I was fortunate to receive external financial support through fellowships. I am sincerely grateful for the recognition from the Jackson Yang & Family Foundation and the UC San Diego Department of Chemistry and Biochemistry for my academic performance. Additionally, I am thankful for the financial and computational support provided by the National Science Foundation and the Department of Energy, which have greatly contributed to the advancement of our research progress.

Finally, I would like to thank my family members and friends in Taiwan, who have supported me in my Ph.D. journey in the United States. I am also thankful to my alma maters National Tsing Hua University and National Taiwan University for providing me with the training and cultivation of my professional knowledge and skills before my enrollment at UC San Diego, which enabled me to overcome countless challenges in my Ph.D. career.

May the God illuminate the path ahead.

Chapter 2, in full, is a reprint of the material as it appears in "Structure and thermodynamics of water adsorption in NU-1500-Cr", C.-H. Ho, M. L. Valentine, Z. Chen, H. Xie, O. Farha, W. Xiong, F. Paesani; Commun. Chem. 6, 70, 2023. The dissertation author was the primary investigator and author of this paper.

Chapter 3, in full, is a part of the material as it appears in "Reversible humidity-dependent pore breathing transformation in CALF-20, a resilient MOF physisorbent for CO_2 capture", Z. Chen, C.-H. Ho, X. Wang, S. M. Vornholt, T. Islamoglu, O. F. Farha, F. Paesani, K. W. Chapman; ACS Mater. Lett. 5, 2942, 2023. The dissertation author was the primary investigator and author of this paper.

Chapter 4, in full, is a reprint of the material as it appears in "Elucidating the competitive adsorption of H_2O and CO_2 in CALF-20: New insights for enhanced carbon capture metal-organic frameworks", C.-H. Ho, F. Paesani; Appl. Mater. Interfaces 41, 48287, 2023. The dissertation author was the primary investigator and author of this paper.

Chapter 5, in full, is a reprint of the material as it appears in "Cooperative Interactions with Water Drive Hysteresis in a Hydrophilic Metal-Organic Framework", J. J. Oppenheim, C.-H. Ho, D. Alezi, J. Andrews, T. Chen, B. Dinakar, F. Paesani, M. Dincă; Chem. Mater. 2024, 36, 3395. The dissertation author was the primary investigator and author of this paper.

Chapter 6, in full, is a reprint of the material as it is being prepared for publication in "Exploring Bulk Water Structure and Entropy Predicted by Two-Phase Thermodynamic Model", C.-H. Ho, F. Paesani. The dissertation author is the primary investigator and author of this paper.

VITA

2010–2014	Academic Counselor, Sigma Academy, Hsinchu, Taiwan
2014	Bachelor of Science, National Tsing Hua University, Hsinchu, Taiwan
2014-2015	Teaching Assistant, Department of Chemistry National Taiwan University, Taipei, Taiwan
2016	Master of Science, National Taiwan University, Taipei, Taiwan
2018–2019	Research & Teaching Assistant, Department of Chemistry National Tsing Hua University, Hsinchu, Taiwan
2019–2020	Teaching Assistant, Department of Chemistry and Biochemistry University of California San Diego, CA, USA
2024	Doctor of Philosophy in Chemistry, University of California San Diego, CA, USA

PUBLICATIONS

C.-H. Ho, F. Paesani, "Exploring Bulk Water Structure and Entropy Predicted by Two-Phase Thermodynamic Mode", *In preparation*.

J. J. Oppenheim[†], **C.-H. Ho**[†], D. Alezi, J. Andrews, T. Chen, B. Dinakar, F. Paesani, M. Dincă* "Cooperative interactions with water drive hysteresis in a hydrophilic metal-organic framework", *Chem. Mater.*, **2024**, *36*, 3395.

C.-H. Ho*, F. Paesani*, "Elucidating the competitive adsorption of H_2O and CO_2 in CALF-20: New insights for enhanced carbon capture metal-organic frameworks", *Appl. Mater. Interfaces* **2023**, *15*, 48287.

Z. Chen[†], **C.-H. Ho**[†], X. Wang[†], S. M. Vornholt, T. Islamoglu, O. F. Farha*, F. Paesani*, K. W. Chapman*, "Reversible humidity-dependent pore breathing transformation in CALF-20, a resilient MOF physisorbent for CO_2 capture", *ACS Mater. Lett.* **2023**, *5*, 2942.

C.-H. Ho*, M. L. Valentine, Z. Chen, H. Xie, O. Farha, W. Xiong, F. Paesani*, "Structure and thermodynamics of water adsorption in NU-1500-Cr", *Commun. Chem.* **2023**, *6*, 70.

Y. Pan, **C.-H. Ho**, F. Paesani*, R. Ghosh*. "Engineering flat and dispersive bands in 2D layered COFs via interlayer stacking and donor-acceptor strategy", *Chem. Mater.* **2023**, *16*, 6235.

AWARDS

2023-24 Distinguished Graduate Student Fellowship	Jan 2024
Jackson Yang Scholarship Award	May 2020
College of Science Elite Student Award	Apr 2012
Academic Achievement Scholarship ($\times$3)	Mar 2011, Oct 2011, Mar 2012

ABSTRACT OF THE DISSERTATION

Exploring the Adsorption of Guest Molecules in Metal-Organic Frameworks: A Many-Body Formalism Approach

by

Ching-Hwa Ho

Doctor of Philosophy in Chemistry

University of California San Diego, 2024

Professor Francesco Paesani, Chair

The utilization of metal-organic frameworks for adsorbing guest molecules has attracted significant interest due to their diverse physical and chemical properties. The capture of atmospheric water and carbon dioxide holds particular importance in addressing challenges related to climate change. In this dissertation, we employ the many-body potential energy functions of water and carbon dioxide to investigate their thermodynamic and dynamical properties as they are adsorbed within several metal-organic frameworks using molecular dynamics simulations. Our investigations not only serve to validate our molecular models through the agreement of experimental and simulation observations but also offer valuable molecular insights that are

challenging to obtain through experimental approaches. Furthermore, this research contributes to the advancement of methodologies for modeling metal-organic frameworks and represents a significant reference in the computational exploration of guest molecules within metal-organic frameworks.

Chapter 1

Introduction

1.1 Preface

The climate of the Earth is primarily regulated by water (H_2O) while the major components of the atmosphere on the Earth are nitrogen ($\sim$78%) and oxygen ($\sim$21%). Since the industrial revolution, the emission of greenhouse gases, such as carbon dioxide (CO_2) and methane (CH_4), due to anthropogenic activities has been recognized as a significant contributor to climate change.[1–5] Climate change poses a gradual threat to human survival, manifesting in rising sea levels,[6–9] water scarcity[10–13], extreme weather events[14–16], and crop failures[17–21]. Consequently, numerous governments and enterprises have committed to reducing greenhouse gas emissions and achieving carbon neutrality.[22,23]

Many research endeavors are dedicated to addressing the impacts of climate change. Among these, the study of metal-organic frameworks to capture specific molecules within their porous structures is a key focus. In addition to experimental efforts to optimize their performance, significant emphasis is placed on theoretical and simulation perspectives to provide molecular insights for rational design. The focus of this dissertation is to provide molecular insights into metal-organic frameworks for atmospheric water harvesting and carbon capture using molecular models developed based on the many-body formalism.

The dissertation is structured as follows: Chapter 1 outlines and introduces simulation approaches for modeling flexible metal-organic frameworks and introduction of many-body

potential energy functions for water and carbon dioxide. Chapters 2 to 5 present research on water, carbon dioxide, or their mixtures within various metal-organic frameworks. Chapter 6 discusses the entropy of various water models using the two-phase thermodynamic model, a simple theory to estimate the entropy of a liquid. Chapter 7 summarizes the research outcomes.

1.2 Metal-Organic Frameworks

Metal-organic frameworks (MOFs) are a class of porous materials comprising metal clusters, also known as secondary building units (SBUs), and organic linkers organized in 1-, 2-, or 3-dimensional networks. Due to their versatile physical and chemical properties, MOFs have found diverse applications in technology, including gas storage, water harvesting, drug delivery, catalysis, and electronic devices.

In molecular dynamics (MD) simulations, achieving realistic representations of MOFs has posed a challenge, as evidenced by the fact that they are still treated as rigid objects in numerous recent studies.[24–28] However, I have developed systematic approaches to parameterize MOFs of interest as flexible structures.

Bonded interaction energies describe the interactions between two atoms in a MOF that are either directly bonded by a chemical bond (1-2 position), separated by an atom commonly bonded to both (1-3 position), or separated by two atoms bonded to each other (1-4 position). The bonded components for all MOFs examined in this dissertation adhere to the following functional forms:

$$V_{bonded}(\vec{R}^N) = \sum_{bonds} \frac{k_b}{2}(r-r_0)^2 + \sum_{angles} \frac{k_a}{2}(\theta-\theta_0)^2 + \sum_{tortion} V_n\left[1+\cos\left(m\phi-\chi\right)\right], \qquad (1.1)$$

where k_b, k_a, and V_n are force constants for a bond, angle, or torsion, respectively, r_0 is the equilibrium bond length, θ_0 is the equilibrium angle, χ is equilibrium angle for a torsion and can only be 0 or π. While determining all force field parameters for a MOF may seem dauntingly challenging, the focus primarily lies on those necessary for describing the SBU, as parameters

for organic linkers can be obtained from existing databases. In this dissertation, all bonded force field parameters for organic linkers were obtained from the General Amber Force Field (GAFF)[29], unless explicitly stated otherwise.

To determine force field parameters for the SBU of interest, I prepared the molecular model representing the SBU. The molecular model was prepared from the optimized structure of the MOF, and the structure the structure followed chemical principles, such as the the octet rule, correct net charge, and spin multiplicity. I then used the prepared SBU to calculate the point charges of all atom according to the Charge Model 5 method. These calculations were carried out using a reliable density functional theory model combined with an appropriate basis set. I followed the same procedure for the organic linkers. The Lennard-Jones (LJ) parameters for all atoms belonging to the organic linkers were obtained from GAFF. For atoms not covered by GAFF, the parameters were obtained from the Universal Force Field (UFF).[30]

Reference configurations and energies are critical for determining the force field parameters of the SBU. In my work, these configurations were generated by systematically displacing the atom of interest within the SBU. All reference energies were calculated using Gaussian 16 with the ωB97X-D functional[31] in combination with the def2-TZVP basis set.[32] To ensure proper representation of the SBU distortion, I generated a number of reference configurations at least five times as large as the number of parameters that I have to fit.

With the point charges, Lennard-Jones parameters, reference configurations, and reference energies in place, I proceeded with the fitting process, which was performed using a genetic algorithm. In this process, I ensured that the scaling of 1-4 interactions was consistent with the approximations adopted by GAFF to avoid any unphysical behavior of the framework. To validate the fitted parameters, I conducted MD simulations of the empty MOF in the isothermal-isobaric (NPT = constant number of atoms, pressure, and temperature) ensemble to ensure that the cell parameters aligned with the experimental data. Subsequently, I performed MD simulations in the microcanonical (NVE = constant number of atoms, volume, and energy) ensemble to confirm proper conservation of the energy.

In my model, the nonbonded interactions between atoms in a MOF consisted of both electrostatic and van der Waals (vdW) interactions:

$$V_{nonbonded}(\vec{R}^N) = \sum_{i<j} \frac{q_i q_j}{4\pi\varepsilon_0 r_{ij}} + \sum_{i<j} 4\varepsilon_{ij} \left[\left(\frac{\sigma_{ij}}{r_{ij}} \right)^{12} - \left(\frac{\sigma_{ij}}{r_{ij}} \right)^{6} \right] \tag{1.2}$$

Here, where q_i represents the point charge of the ith atom, ε_0 is the vacuum permittivity, r_{ij} is the distance between atoms i and j, and σ_{ij} and ε_{ij} are LJ parameters for the i, j pair of atoms, which were calculated using the Lorentz-Berthelot rules:

$$\sigma_{ij} = \frac{\sigma_{ii} + \sigma_{jj}}{2}, \varepsilon_{ij} = \sqrt{\varepsilon_{ii}\varepsilon_{jj}} \tag{1.3}$$

. Here, σ_{ii} and ε_{ii} represent the Lennard-Jones parameters for atoms of the same type.

1.3 Many-body potential energy functions for water and carbon dioxide

The molecular model for water and carbon dioxide is developed based on the many-body formalism, which describes the total energy of the N-body system in terms of the sum of n-body energies[33]:

$$E_N = \sum_{i=1}^{N} V^{1B}(i) + \sum_{i<j}^{N} V^{2B}(i,j) + \sum_{i<j<k}^{N} V^{3B}(i,j,k) + \cdots + V^{NB}(1,2,...,N), \tag{1.4}$$

where the one-body ($1B$) energy corresponds to the energy of a monomer, and the n-body energies are defined recursively as follows:

$$V^{nB} = E_n - \left(\sum_{i=1}^{n} V^{1B}(i) + \sum_{i_1<i_2}^{n} V^{2B}(i_1,i_2) + \cdots + \sum_{i_1<\cdots<i_{n-1}}^{n} V^{(n-1)B}(i_1,\cdots,i_{n-1}) \right) \tag{1.5}$$

The potential energy for a molecule developed based on equations 1.4 and 1.5 is referred to as the many-body energy (MB-nrg) potentials. For water, such a many-body potential is known as

MB-pol.[34–36]

A natural question regarding the many-body formalism pertains to its applicability: which types of systems can be effectively modeled using this method? Due to the computational cost associated with n-body energy, we are essentially unable to explicitly parameterize the n-body short-ranged quantum-mechanical interaction energies to arbitrarily high bodies. Consequently, we must omit those terms at a certain point. Therefore, this modeling methodology is feasible for systems in which the electron clouds of monomers do not become excessively delocalized among all monomers as the number of monomers increases, as their n-body energy quickly converges with increasing n. In the context of water, it has been demonstrated that three-body contributions account for approximately 15%-20% of the total interaction energy, while four-body effects contribute approximately 1%.[37–40] Therefore, before developing a molecular model using the many-body formalism, it is essential to determine the point at which the n-body interaction energy can be neglected.

The one-body potential for water is developed based on the work of Partridge and Schwenke.[41] The corresponding one-body potential for CO_2 was developed using permutationally invariant polynomials (PIPs) with reference energies calculated at the coupled-cluster level of theory, including single, double, and perturbative triple excitations, i.e., CCSD(T). All n-body terms with $n > 1$ include classical induction, which describes the polarization of molecules in the presence of an electric field. The two-body energy consists of four terms:

$$V^{2B} = s_2 V^{2B}_{short} + V^{2B}_{elect} + V^{2B}_{disp} + V^{2B}_{ind}, \tag{1.6}$$

where V^{2B}_{ind} represents the classical two-body induction energy, V^{2B}_{elect} is the permanent electrostatic energy, V^{2B}_{disp} is the dispersion energy, V^{2B}_{short} represents short-ranged quantum-mechanical interactions arising from the overlap of monomer's electron densities, and s_2 is the switching function that smoothly turns off V^{2B}_{short} as the distance between two monomers increases. The

three-body energy consists of two terms:

$$V^{3B} = s_3 V^{3B}_{short} + V^{3B}_{ind}, \tag{1.7}$$

where V^{3B}_{ind} denotes the classical three-body induction energy and V^{3B}_{short} represents short-ranged quantum-mechanical interaction energy. The function s_3 serves as a switching function that gradually turns off V^{3B}_{short} depending on the distances between two monomers within the trimer. The V^{3B}_{ind} term is found to be crucial in accurately describing many-body interactions of neat water and ion-water systems.

1.4 Interactions between MOFs and guest molecules

In the context of MD simulations, the interactions between the framework and guest molecules are parameterized by non-bonded terms. Readers should note that the many-body formalism includes induction effects, which describe the distortion of electron density caused by an electric field. Consequently, the accuracy of framework-guest molecule interactions is significantly influenced by the point charges of all atoms in the framework.

As mentioned in section 1.2, all the point charges of atoms in the framework were determined using Charge Model 5. While other methods, such as Density Derived Electrostatic and Chemical (DDEC)[42] and Bader Charge Analysis[43], could also be employed to determine the point charges of the framework atoms, we evaluated these methods in the study of water in NU-1500-Cr (the system introduced in Chapter 2) and found that Charge Model 5[44] provided the best agreement with the experimental results. Possible reasons for the better performance of Charge Model 5 may be related to the fact that this model was designed to accurately reproduce the dipole moments of molecules. This feature potentially makes Charge Model 5 more compatible with the many-body formalism, leading to better agreement with experimental results.

The van der Waals interactions between the framework atoms and the guest molecules are commonly described by the Lorentz-Berthelot rules, as in equation 1.3, and they often serve

as a good approximation, which has been validated by *ab initio* calculations. However, these approximation fail to adequately describe framework-guest molecule interactions that cannot be represented by simple LJ potentials. In this context, the van der Waals interactions between water and the SBU of NU-1500-Cr were parameterized from *ab initio* energies using more sophisticated Buckingham potentials to overcome the limitations of LJ potentials.

Chapter 2

Structure and thermodynamics of water adsorption in NU-1500-Cr

2.1 Introduction

With a changing climate, water scarcity has become one of the most pressing global issues, which already affects almost two thirds of the world's population[45]. Various technologies (e.g., membrane and thermal desalination) have been developed to produce freshwater from seawater.[46,47] Due to the associated cost and infrastructure required, most of these technologies, however, are generally only viable for large-scale and centralized water production. Decentralized water production represents an alternative strategy to provide freshwater to areas that cannot be easily connected to a centralized distribution network. Since air contains $\sim 10^{21}$ liters of water as drops and vapor, atmospheric water harvesting (AWH) has emerged as a promising alternative approach to provide freshwater to areas of water scarcity, as well as for the development of other water-based technologies.[48]

Among porous materials that can efficiently adsorb water from air over a tunable range of relative humidity (RH), metal-organic frameworks (MOFs) have recently attracted particular interest.[49–51] Built from organic linkers and secondary building units (SBUs) composed of metal ions or clusters, MOFs exhibit large surface areas and a variety of physicochemical properties that can be tuned for specific applications through either pre- or post-synthetic approaches.[52,53] To act as an efficient water sorbent, a given MOF must satisfy the following requirements:

i) high hydrolytic stability for recycling performance, ii) large porosity and surface area for high water vapor uptake, iii) relatively mild regeneration conditions, iv) adsorption isotherm with a steep uptake at a specific RH value, and v) high deliverable capacity. Several MOFs with high stability and water sorption capacity have been reported in the literature.[54–62] While measurements and calculations of isotherms and enthalpies of adsorption provide information about the overall performance of a given MOF for water-sorption applications, a molecular-level understanding of the sorption mechanisms, which is key to the design of new MOFs with improved sorption capacities, remains elusive.[49–51] The major difficulty arises from the complexity of the water-framework interface which makes the realistic modeling of the adsorption mechanism particularly challenging. Several models have been developed to investigate the properties of water using computer simulations, which often rely on pairwise additive energy expressions that are empirically parameterized to reproduce a subset of experimental data (e.g., the TIPnP[63–65], SPC*[66,67] families of water models). Due to the difficulties in getting "the right results for the right reasons" in computer modeling of water as a function of temperature and pressure, establishing a reliable connection between computer simulations and experimental measurements of water confined in MOFs remains challenging. Another challenge arises from the intrinsic complexity of the MOF structures. Several water-adsorbing MOFs possess frameworks with various non-equivalent pores, which makes it difficult to unambiguously characterize the water sorption mechanisms at the molecular-level.[68–70]. Additional difficulties in computer simulations of water adsorption in MOFs are related to the approximations that are made for modeling the frameworks. Since MOF structures are determined by crystallography, molecular simulations typically only model perfect frameworks in which the unit cell is exactly repeated in each direction without including any defects. Although great efforts have been made to characterize defects in MOFs, little direct information is available about the chemical structure around defects[71–76]. In the context of computer simulations, ambiguities in the framework structure may lead to inaccurate representations of water-framework interactions which, in turn, may affect the overall description of the sorption mechanisms. Other experimental techniques

that are sensitive to defects could greatly improve our understanding to defects in MOFs and their interactions with water molecules.

In this study, we investigate the water sorption mechanism of NU-1500-Cr,[62] a high-performance MOF for AWH applications, using a combination of computational and spectroscopic approaches. NU-1500-Cr contains hexagonal pores connected by two types of channels that extend along orthogonal directions. Its well-defined single-step adsorption isotherm exhibits maximum capacity of water uptake exceeding 1.0 g/g, which remains effectively unchanged after 20 adsorption-desorption cycles.[62] The molecular mechanisms of water adsorption in NU-1500-Cr are unravelled from systematic analyses of both thermodynamic and dynamical properties of water that are calculated from advanced molecular dynamics (MD) simulations carried out with the MB-pol many-body potential.[34–36] We determine that the adsorption process begins with water molecules saturating the Cr(III) open sites of the framework and proceeds with the formation of water chains along one of the channels, which is then followed by sequential filling of the main pores.

2.2 Methods

2.2.1 Material preparation and characterization

NU-1500-Cr sample was prepared following literature method.[62] The sample was activated at 120 °C for 12 hours before sorption mesurements. The N_2 adsorption isotherm was measured on a Micromeritics ASAP 2420 (Micromeritics, Norcross, GA) instrument at 77 K (see Supplementary Figure 10). The pore volume was evaluated at $P/P_0 = 0.99$ as 1.24 cm^3/g and the Brunauer–Emmett–Teller (BET) surface area was calculated as 3575 m^2/g which correspond well with the reported values (1.24 cm^3/g and 3580 m^2/g respectively) in the literature. The water adsorption isotherm of NU-1500-Cr was measured on a micromeritics 3Flex at 25 °C (see Figure 1(a) and Supplementary Figure 11). Degased Millipore water was used as vapor source. The measurement temperature was controlled with a Micromeritics temperature controller.

2.2.2 Molecular model

NU-1500-Cr was modeled using a flexible force field. The structure of NU-1500-Cr was taken from crystallographic data,[62] with one Cr^{3+} atom in each SBU coordinated with a chloride ion and the other two Cr^{3+} coordinated with the oxygen atoms of two water molecules. The crystallographic structure was initially optimized in periodic boundary conditions using density functional theory (DFT) calculations carried out with the Vienna Ab initio Simulation Package (VASP),[77–80] using the PBE exchange-correlation functional[81] combined with the D3 dispersion correction.[82] The VASP calculations were carried out using the projector-augmented wave (PAW) method[83,84] with a 700 eV kinetic energy cutoff on a 2×2×2 k-point grid. The forces were converged to a tolerance of 0.03 eV/Å. The atomic point charges for the force field were obtained using the charge model 5 (CM5)[44] as implemented in Gaussian 16[85] by performing DFT calculations on a cluster model of NU-1500-Cr (see Supplementary Figures 1-2 for details) using the ωB97X-D functional[31] in combination with the def2-TZVP basis set.[32] The force field parameters for the bonded terms involving the Cr^{3+} atoms were fitted using the genetic algorithm to ωB97X-D/def2-TZVP single point energies calculated with Gaussian 16[85] for 249 distorted configurations of the same cluster model of NU-1500-Cr used in the CM5 calculations. The Lennard-Jones (LJ) coefficients for the Cr^{3+} atoms were taken from the Universal Force Field (UFF).[30] The force field parameters for the bonded and Lennard-Jones terms involving the linker atoms were instead taken from the General Amber Force Field (GAFF).[29]

Water was modeled using the MB-pol many-body potential[34–36] that accurately reproduces the properties of water from gas-phase clusters to liquid water and ice.[86,87] As in our previous studies, the framework–water interactions were represented by electrostatic and LJ terms, except for the Cr^{3+}–water interactions where the LJ potential was replaced by a Buckingham potential fitted to ωB97X-D/def2-TZVP energy scans of a water molecule relative to the same cluster model used in the CM5 calculations (see Supplementary Figure 3). The electrostatic term included both permanent and induced contributions where the water molecules

were allowed to be polarized by the point charges of the framework. LJ parameters between the framework atoms and the water molecules were obtained according the Lorentz-Berthelot mixing rules using the LJ parameters of the TIP4P/2005 water model, which was shown to be the closest point-charge model to MB-pol.[88]

2.2.3 Molecular dynamics simulations

All MD simulations were carried out under periodic boundary conditions for a system consisting of 2×2×2 primitive cells of NU-1500-Cr and various water loadings corresponding to RH values between 0% to 39.0%. MD simulations were performed in the isothermal-isobaric (constant number of atoms, pressure, and temperature, NPT); canonical (constant number of atoms, volume, and temperature, NVT); and microcanonical (constant number of atoms, volume, and total energy, NVE) ensembles to calculate various structural, thermodynamic, and dynamical properties. The temperature in the NVT and NPT simulations was controlled using a massive Nosé-Hoover chain thermostat where each degree of freedom was coupled to a Nosé-Hoover thermostat chain of length 4. The pressure in the NPT simulations was controlled by a Nosé-Hoover barostat based on the algorithm introduced in Ref.[89] The equations of motion were propagated according to the velocity-Verlet algorithm with a time step of 0.2 fs. The nonbonded interactions were truncated at an atom-atom distance of 9.0 Å, and the long-range electrostatic interactions were treated using the Ewald sum.[90] All MD simulations were carried out with in-house software based on the DL_POLY_2 simulation package. Assessments of the force field parameters are summarized in the Supplementary Tables 1-7.

At each loading, the initial configuration of the water molecules was prepared using Packmol, with a uniform distribution of the water molecules in all pores.[91,92] Each system was then further randomized in the NPT ensemble at 1 atm and 500 K for 100 ps, followed by 20 ps at 1 atm and 298.15 K. Lattice parameters, equilibrium bond distances, and enthalpies of adsorption were calculated from 1 ns trajectories carried out in the NPT ensemble at 1 atm and 298.15 K. Assuming that the water molecules in gas phase obey the ideal gas law, and the PV

terms of MOF loaded with water and empty MOF are approximately equal, the enthalpy of adsorption at a given RH is given by

$$\Delta H_{ads} = \frac{U(\mathrm{MOF}+\mathrm{H_2O}) - U(\mathrm{MOF}) - N \times U(\mathrm{H_2O}) - N \times \mathrm{RT}}{N}, \tag{2.1}$$

where N is the number of water molecules, R is the ideal gas constant, T is the temperature, U(MOF), U(H_2O), and U(MOF + H_2O) are the internal energies of empty MOF, single water molecule, and MOF loaded with water molecules at a given RH value, respectively. The dynamical properties and entropies were calculated by averaging over 20 independent 50 ps trajectories performed in the NVE ensemble, with the volume fixed at the average value calculated from the corresponding NPT simulations. The water entropy at each loading was calculated using the two-phase thermodynamic (2PT) model[93]. The theoretical infrared spectra were calculated from the autocorrelation function of the total dipole moment according to

$$I(\omega) = \left[\frac{2\omega}{3V\hbar c\varepsilon_0}\right] \tanh\left(\frac{\hbar\omega}{k_B T}\right) \int_{-\infty}^{\infty} \langle \mu(0)\mu(t)\rangle \, \mathrm{e}^{i\omega t} dt, \tag{2.2}$$

where V is the volume of the system, c is the speed of light in the vacuum, ε_0 is the vacuum permittivity, k_B is the Boltzmann constant, T is the temperature, and $\langle \mu(0)\mu(t)\rangle$ is the ensemble averaged dipole-dipole time correlation function, with μ being represented by the many-body dipole moment function (MB-μ)[94].

2.2.4 Infrared spectroscopy

NU-1500-Cr powder was mixed with KBr in a mass ratio of 1:20 and placed in a DiffusIR DRIFTS cell fitted to a Nicolet iS10 spectrometer. The humidity inside the DRIFTS cell was controlled by a humidity generator, which has previously been described[95], utilizing nitrogen gas and 18MΩ ultrapure water. The humidity inside the DRIFTS cell was monitored using a calibrated humidity meter, and each RH was maintained for 20 minutes before collecting a spec-

trum. Each measured FTIR spectrum was recorded immediately after collecting a background spectrum of KBr powder. A spectrum of activated NU-1500-Cr was obtained by activating the sample at 130 °C for several hours in a vacuum oven, transferring the sample to a nitrogen-filled DRIFTS cell while still above 120 °C, then acquiring the spectrum after the sample reached room temperature. Spectra of HOD in NU-1500-Cr were acquired by the same procedure as the H_2O spectra. Spectra were first acquired for a concentrated HOD solution made by combining ultrapure water and 99% D_2O (Cambridge Isotope Labs) in a 9:1 volume ratio. Spectra were then acquired for 99% D_2O without any added H_2O. The 99% D_2O spectra were used as backgrounds and subtracted from the concentrated HOD spectra to reduce the impact of C-H and other MOF peaks on the O-H band. The resulting background-subtracted spectra are shown in Supplementary Figure 8 and were used for the fitting presented in Supplementary Figure 9.

2.3 Results and Discussion

2.3.1 Thermodynamics of water adsorption

The experimental adsorption isotherm of water in NU-1500-Cr (Figure 2.1a) slowly increases up to ∼33% RH where it exhibits a sharp step that effectively ends at ∼37% RH, after which it only shows a moderate increase up to ∼70% RH. It should be noted that the adsorption isotherm shown in Figure 1a slightly differs from the adsorption isotherm reported in ref 62. The difference is due to the use of an incorrect value of the saturated vapor pressure of water at 298 K in the original study, which results to the original adsorption isotherm being shifted to slightly higher RH values relative the adsorption isotherm measured in the present study. To gain insights into the confining effects of the framework on the properties of water adsorbed in the pores, the enthalpy of adsorption (ΔH_{ads}) and water entropy (S_{wat}) calculated from MD simulations carried out as a function of RH are shown in Figure 2.1b and 2.1c, respectively. ΔH_{ads} becomes progressively more negative, indicating stronger framework–water interactions, as the RH increases and plateaus at a value of ~ -14.5 kcal/mol between 15% and 31% RH. After

this point, ΔH_{ads} rapidly increases to a value of ~ -12.5 kcal/mol in correspondence of the step in the adsorption isotherm between $\sim$33% and $\sim$37% RH and remains approximately constant at higher RH. At the lowest RH, the calculated enthalpy of adsorption is -13.4 kcal/mol, which is in a good agreement with the experimental values extracted from measurements of water adsorption in other MOFs using the Clausius–Clapeyron equation.[54,57,96,97] The decrease in ΔH_{ads} observed from 1.8% to 31% RH can be attributed to both the development of hydrogen bonds among water molecules and framework–water interactions. Since the hydrogen-bond network becomes more extended as the RH increases, the increase in enthalpy in correspondence of the adsorption step (i.e. $\sim$33% and $\sim$37%) suggests that framework–water interactions play a minor role at high RH values. It is worth noting that ΔH_{ads} at high RH values is more negative than the enthalpy calculated from MB-pol simulations of liquid water at 298 K (~ -10.96 kcal/mol), which suggests that the confinement of water molecules within the NU-1500-Cr framework is, overall, energetically favorable.

S_{wat} displays similar variation to ΔH_{ads} up to $\sim$31% RH, decreasing monotonically to a value of $\sim$19.6 cal/mol K. Contrary to ΔH_{ads}, S_{wat}, however, exhibits a steep drop at $\sim$36% RH, and remains approximately constant to a value of 16.5 cal/mol K at higher RH. The decrease in entropy as a function of RH is the result of both confinement effects caused by the framework and spatial constraints due to hydrogen bonding which restrict the motion of water molecules. Importantly, S_{wat} approaches a value of 16.5 cal/mol K at high RH beyond the adsorption step, which is very close to the entropy of liquid water at the same thermodynamic conditions (T = 298.15 K and P = 1 atm) 16.7 cal/mol K.[98] Although this similarity may suggest liquid-like behavior for water in the NU-1500-Cr pores at high RH, systematic analyses of local structure and hydrogen-bonding topologies reported in the next sections indicate that there are significant differences. The shape of the adsorption isotherm can directly be rationalized in terms of the competition between enthalpic and entropic effects of water. At low RH, ΔH_{ads} compensates for the loss of entropy that accompanies the transition of water molecules from the gas phase to the NU-1500-Cr pores and then becomes the dominant factor during pore filling that is triggered by

the formation of an extended hydrogen-bond network among the water molecules. A similar trend in enthalpy of adsorption as a function of RH was observed in UiO-66 and its functionalized derivatives, which have been well-known as atmospheric water harvesters.[99]

2.3.2 Structure and filling mechanism

To characterize the thermodynamic properties of water in NU-1500-Cr at the molecular level, we examine the structure of the framework and the distribution of water at different RH values. Figures 2.2(a-b) illustrates the structure of the empty framework, which is composed of $Cr_3(\mu\text{-}O)(H_2O)_2Cl$ SBUs linked by deprotonated peripherally extended triptycenes (PETs). Two Cr^{3+} metal ions in each SBU are saturated with water molecules, while the third Cr^{3+} metal ion is saturated with a chloride ion. Each SBU is connected with three PETs that build up a three-dimensional network with the 1-dimensional hexagonal pores of diameter $\sim$ 1.4 nm extending along the *c*-axis, as shown in Figure 2.2(a). The other two types of channels (hereafter referred to as type-A channel and type-B channel) orthogonal to the hexagonal pores allow water molecules to move across the hexagonal pores. A type-A channel is composed of two adjacent SBUs, which are parallel to the hexagonal pores, and the aryl groups of three PETs. A type-B channel is created from the stacking of two PETs along the direction of the hexagonal pores (Figure 2.2(b)).

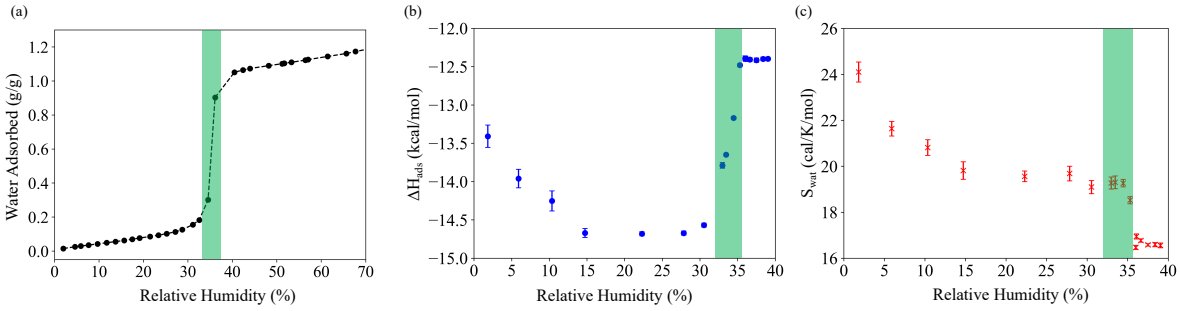

Figure 2.1. Thermodynamics of water adsorption in NU-1500-Cr. (a) Experimental water adsorption isotherm. (b) Enthalpy of adsorption ΔH_{ads} and (c) water entropy S_{wat} at different RHs. Green regions correspond to the adsorption step.

Figure 2.3(a) summarizes the statistics of different hydrogen-bonding topologies created by water molecules as a function of RH. Each water molecule is classified as donor (nD) or acceptor (mA) according to the type and number (n and m) of hydrogen bonds it engages in. The majority of water molecules acts as no donors-single acceptors (i.e., 0D-1A) at the lowest RH (1.8%), which suggests there exist interaction sites in the framework that serve as hydrogen-bond donors. Analyses of oxygen-oxygen radial distribution functions (RDFs) presented in Supplementary Figure 5 demonstrate that the first water molecule that enters the framework directly binds to one of the water molecules that saturate a Cr^{3+} open site. Therefore, the saturating water molecules are the primary interaction sites for initial hydration of the MOF pores. Similar conclusion were drawn from computer simulations of water in MIL-100(Fe), MIL-101(Cr), and Co_2Cl_2BTDD, and a recent experimental study of water in HKUST-1.[27,28,100,101] This similarity in the initial stages of the hydration process is associated with similarly strong interactions between water and the open metal sites of the frameworks, which give rise to dative bonds between the oxygen lone-pair of a water molecule and an empty d-orbital of the metal ions. It should be noted that the presence of open metal sites in the framework is not a necessary condition for a MOF to be able to adsorb water, since functional groups can also serve as interaction sites. For example, MOF-801 and ZIF-90 adsorb water via their μ_3-OH and carbonyl groups, respectively[54,102].

Figure 2.3(a) indicates that the 1D-1A hydrogen-bonding topology becomes dominant as the RH increases beyond 15%, while the 2D-2A topology is dominant after the adsorption step (i.e., at RH higher than 37%). As water molecules get adsorbed, they primarily form water chains that emanate from the saturating water molecules and extend into type-A channels. The spatial distribution of the water chains inside the framework at 14.7% RH shown in Figure 2.2(c-d) indicates that the water molecules are located in type-A channels and connect the adjacent SBUs, while leaving both the hexagonal pores and type-B channels empty. Similar spatial distributions are obtained for all RH values below 33%, indicating that type-A channels have sufficient space to accommodate up to 0.24 g/g of water. It should be noted that the relatively small diameters

(∼9.6 Å) of type-A channels prevent the water molecules from forming extended hydrogen-bond networks as in liquid water, which implies that favorable water–framework interactions must be responsible for the adsorption of water inside type-A channels at the early stages of the adsorption process. These results can be rationalized by considering the water-benzene dimer as a model system for describing the interactions between water and the PET linkers of type-A channels. As shown in Supplementary Figure 4, the benzene-water potential energy scan exhibits a binding energy of $\sim$ 2 kcal/mol when the water molecule point one of the OH bond towards the aromatic ring, which is consistent with previous *ab initio* calculations of benzene-water interactions [103]. As a consequence, the more negative values calculated for the enthalpy of adsorption from 1.8% to 31% RH can be attributed to the growing number of water molecules interacting with the PET linkers of type-A channels.

At RH values higher than 33%, the additional water molecules start filling the hexagonal pores as type-A channels are fully occupied, which corresponds to the adsorption step on the isotherm, and the abrupt changes in adsorption enthalpy and water entropy shown in Figures 2.1(b) and 2.1(c). Pore filling begins with the formation of water bridges connecting water molecules located in separate type-A channels, and continues with the development of extended hydrogen-bonding networks that emanate from the water bridges (see Supplementary Figure 6).

The hydrogen-bonding topologies in Figure 2.3(a) also indicate that the dominant topology changes from 1D-1A to 2D-2A as the hexagonal pores start being filled, suggesting that the majority of water molecules experience local environments resembling those found in liquid water. However, the percentage of 2D-2A topology (∼37%) is slightly smaller than the corresponding value predicted by MB-pol simulations of liquid water (∼45%) [104]. This difference can be attributed to the presence of the framework that constrains the development of hydrogen-bonding networks. Further insights into the structure of water adsorbed in the hexagonal pores of NU-1500-Cr is gained by analyzing the variation of the tetrahedral order parameter q_{tet} which

is defined as[105]

$$q_{tet} = 1 - \frac{3}{8} \sum_{j=1}^{3} \sum_{k=j+1}^{4} \left(\cos \psi_{ijk} + \frac{1}{3} \right)^2, \tag{2.3}$$

Here, ψ_{ijk} is the angle between the oxygen atom of the central water molecule with index i and two oxygen atoms in the neighbor with index j and k at a distance smaller than 3.5 Å. A value 0 for q_{tet} indicates a completely disordered arrangement of the water molecules (as in an ideal gas), while $q_{tet} = 1$ indicates a perfectly tetrahedral arrangement of water molecules. Figure 2.3(b) shows that the probability $P(q_{tet})$ of local structures with $q_{tet} > 0.6$ is negligible from 1.8% to 22.3% RH, indicating that a low relative humidity the water molecules are spatially arranged in a disordered manner. As RH increases, $P(q_{tet})$ acquires a bimodal distribution with two maxima at $q_{tet} \approx 0.4$ and $q_{tet} \approx 0.8$. Compared to $P(q_{tet})$ calculated with MB-pol for liquid water at 298 K (black curve in Figure 2.3(b)), $P(q_{tet})$ calculated for water in NU-1500-Cr at high RH displays a wider distribution at low q_{tet} values and significantly lower amplitude at high q_{tet} values, indicating a relatively more disordered hydrogen-bond network compared to liquid water.

From the analysis of the spatial distribution of water in NU-1500-Cr, which is shown in Figure 2.4 for 34.6% RH (corresponding to the middle of the step in the adsorption isotherm), it is possible to conclude that the hexagonal pores are filled sequentially. Similar mechanisms were reported for water adsorption in ZIF-90, MIL-100(Fe), and MIL-101(Cr).[27,28,95] Since the water molecules located in the main pores are far away from the framework and surrounded by other water molecules, the associated interaction energy mostly results from water-water interactions. As a consequence, water molecules fill up one pore at a time, preferentially entering pores that already contain other water molecules which can thus maximize the number of hydrogen bonds.

In summary, the evolution of the adsorption isotherm as a function of RH can be rationalized as a sequence of three stages. The Cr^{3+} metal sites of the SBUs provide the strongest binding sites for water adsorption. Upon saturation of the Cr^{3+} binding sites, given their hydrophilic nature, the metal-bound water molecules become new binding sites for other water molecules at the early stages of the adsorption process. Water chains connecting the metal-bound water

molecules then develop prior to the filling of the hexagonal pores. These chains extend along type-A channels where the water molecules can establish favorable interactions with the aromatic rings of the PET linkers. The steep uptake displayed by the adsorption isotherm between 33% and 37% RH result from all type-A channels being fully occupied by water, which thus determines the onset of the filling of the hexagonal pores. The mechanism of water adsorption derived from the MB-pol simulations suggests that in order to move the water adsorption step of NU-1500-Cr to lower RH values, the hexagonal pores should be decorated with hydrophilic functional groups that will prevent water molecules from filling the type-A channels at the early stages of the adsorption process.

2.3.3 Infrared spectra

To further characterize the water hydrogen-bond networks in the NU-1500-Cr pores, we examined infrared spectra of water in the MOF pores compared to liquid water, focusing on the bend+libration combination band and OH-stretch vibrational band. The bend+libration combination band is highly sensitive to water-water interactions, shifting to lower frequencies when the hydrogen-bond network of water is disrupted, and shifting to higher frequencies when the hydrogen-bond network of water is highly ordered[106]. As shown in Figure 2.5(a), the bend + libration combination band is not well defined at low humidities, but becomes apparent near 30% RH as the number of MOF-bound water molecules increases and water-water interactions become more significant. For all RH values above $\sim$30%, the bend+libration combination band for water in NU-1500-Cr is shifted to much lower frequencies than in liquid water, but the shift is smaller above 40% RH. This indicates a highly disrupted hydrogen-bond network that becomes more similar to liquid water as the pores fill. This qualitative trend matches the trends observed for hydrogen-bonds in the simulations shown in Figure 2.3(a) and the trend observed for the tetrahedral order parameters in Figure 2.3(b), and suggests that water-water hydrogen-bonds increase throughout the pore-filling process.

The OH-stretch vibrational band of water also reports on the strength of hydrogen bonds,

and can be decomposed into multiple peaks to analyze different local environments experienced by water molecules. Figure 2.5(b) shows the OH-stretch vibrational band of water in NU-1500-Cr measured at humidities between 20% RH and 55% RH compared to the corresponding band measured for liquid water. At low RH, the band consists primarily of an extremely broad tail below 3200 cm^{-1} that is not present in the infrared spectrum of liquid water, and a set of narrow sharp peaks around 3600 – 3700 cm^{-1}, at much higher frequencies than in liquid water. As the

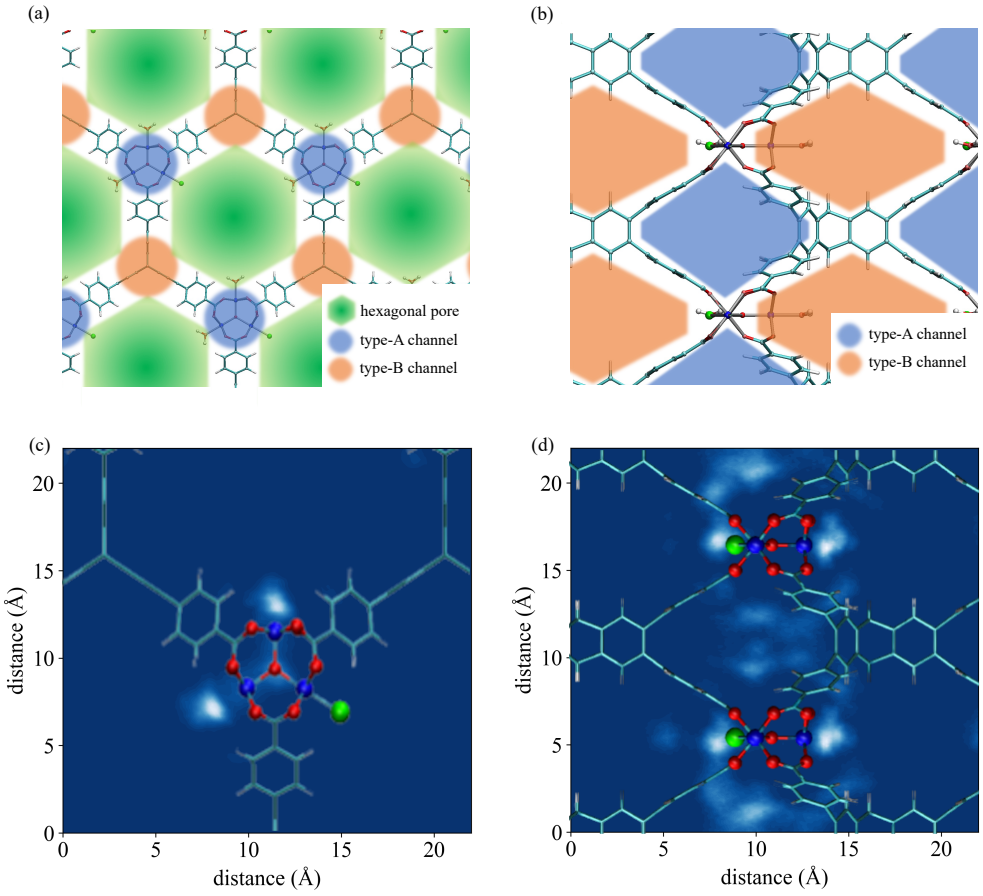

Figure 2.2. NU-1500-Cr structure and water density distribution. (a) Structure of NU-1500-Cr viewed along the hexagonal pore direction. The hexagonal pores are shown in green, while type-A and type-B channels are shown in blue and orange, respectively. (b) Structure of NU-1500-Cr viewed along a direction perpendicular to the hexagonal pore direction. The hexagonal pores are not displayed for the clarity, while type-A and type-B channels are shown in blue and orange, respectively, as in (a). Two-dimensional water density distribution calculated along (c) and perpendicular (d) to the hexagonal pore direction at 14.7% RH. Lighter regions correspond to higher water density. Color scheme: C = cyan, H = white, O = red, Cr = blue, Cl = green.

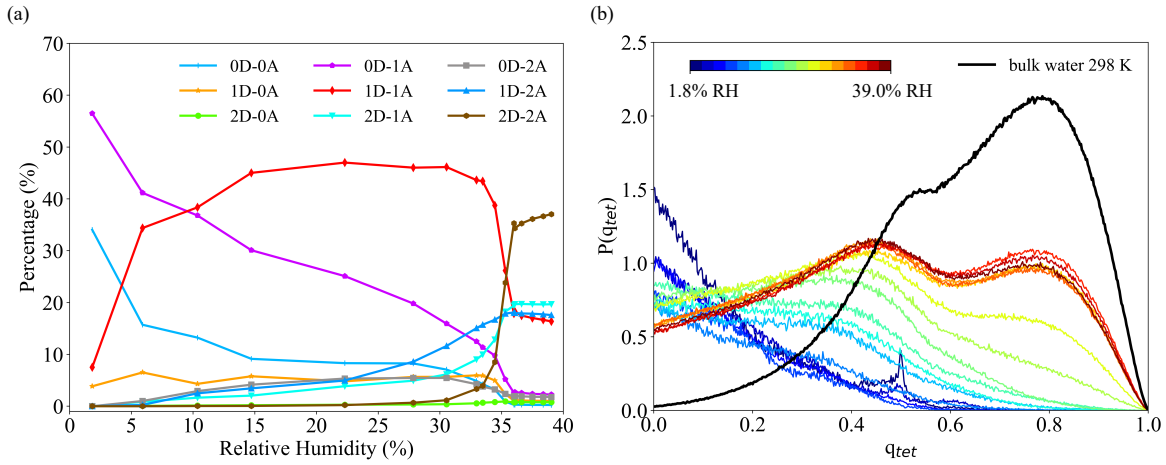

Figure 2.3. Water's hydrogen-bonding structure in NU-1500-Cr. (a) Hydrogen-bond topologies distribution. (b) Probability distributions of the tetrahedral order parameter, $P(q_{tet})$. Black curve shows $P(q_{tet})$ of liquid water calculated from MD simulations carried out with MB-pol at 298 K.[104]

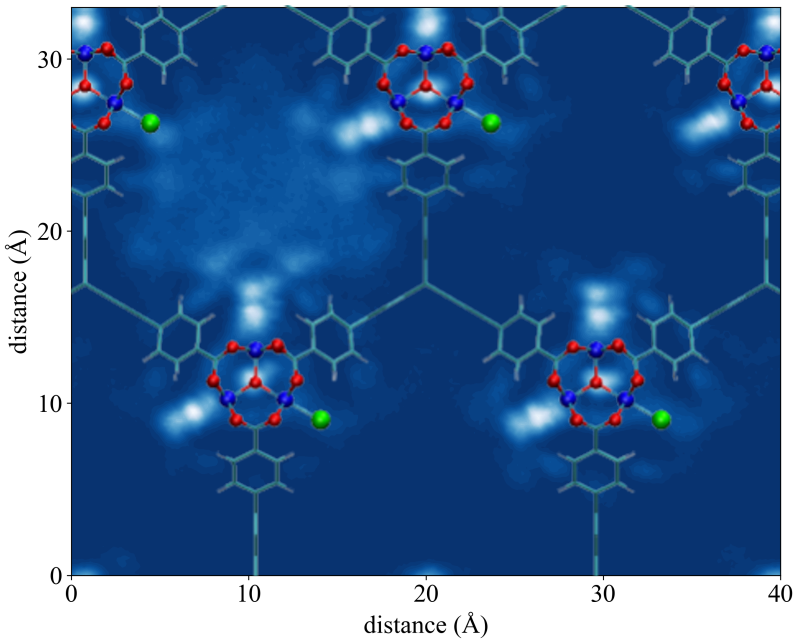

Figure 2.4. Water spatial distribution in NU-1500-Cr. Two-dimensional water density distribution in the hexagonal pores of NU-1500-Cr calculated at 34.6% RH. Color scheme: C = cyan, H = white, O = red, Cr = blue, Cl = green.

humidity increases, the sharp high-frequency peaks and broad low-frequency peaks become less prominent relative to the total OH-stretch band, but are still present at each relative humidity.

Control experiments using HOD diluted in D_2O provides simpler lineshapes, which still displays the same three features (see Supplementary Figure 8). In previous studies of water in confined environments, sharp high-frequency peaks have been assigned to "dangling" and interfacial OH bonds with relatively weak interactions[107–109], while peaks at lower frequencies have been assigned to water molecules in highly charged environments[110,111]. Spectral features between the high-frequency and low-frequency regions were found to more closely resemble those observed for liquid water. Throughout the pore filling process of NU-1500-Cr, the relative intensities of the broad low-frequency features and narrow high-frequency features decreases, and the spectrum progressively becomes more similar to that of liquid water when the pores are completely filled, which is consistent with the calculated hydrogen-bond and q_{tet} results, as well as trend observed for the bend + libration combination band. In the control experiments with HOD (see Supplementary Figure 8), the trend is even clearer due to the relative simplicity of the OH-stretch vibrational band associated with HOD molecules.

The significant intensity between 2800 and 3100 cm^{-1} at low RH, however, suggests the existence of highly charged atoms polarizing water molecules, which were not originally accounted for in simulations. In order to further elucidate the spectral signatures observed experimentally, Figure S7 shows the infrared spectrum of water in pristine NU-1500-Cr simulated at 20% RH following the procedure described in ref 95. In order to further elucidate the spectral signatures observed experimentally, Figure S7 shows the infrared spectrum of water in pristine NU-1500-Cr simulated at 25% RH following the procedure described in ref 95. While the simulated spectrum overall reproduces the experimental lineshape, the low-frequency tail below 3100 cm^{-1} is missing. This missing tail can be recovered from MD simulations carried out with modified SBUs as shown in Figure 2.6(a), where the charge of the Cr^{3+} atoms are increased by 50% and the charges of the oxygen atoms of the carboxylate groups are adjusted accordingly to guarantee charge neutrality. As the fraction of modified SBUs in the MD simulations is

increased, the intensity of the low-frequency portion of the simulated spectrum also increases while retaining all the other spectral signatures, which systematically improves the agreement with the experimental lineshape. This analysis suggests that highly charged Cr^{3+} may likely be present in the NU-1500-Cr samples used in the experiments, which may be attributed to undercoordinated Cr^{3+} sites due to structural disorder. The modified SBUs also account for the humidity-dependent trends observed in the relative intensity of the low-frequency features, which are most prominent at low RH when there are relatively few water molecules and they are clustered near the SBUs.

The infrared spectra of the water molecules that directly bind to the Cr^{3+} sites of both unmodified and modified SBUs are calculated in order to isolate their specific signatures from the overall spectra. Figure 2.6(b) demonstrates that the low-frequency tail in the experimental spectrum stems from the OH-stretch vibrations of the water molecules bound to the charge-modified Cr^{3+} sites (water #1 in the figure) which are involved in a hydrogen-bond with a neighboring water molecule. As shown in Figure 2.6(b), while still present in the infrared spectrum of water molecules bound to Cr^{3+} sites with unmodified charges, the spectral feature associated with the hydrogen bond between the metal-bound water molecule and a neighboring water molecule appears at relatively higher frequencies ($\sim$3450 cm^{-1}).

This analysis demonstrates that the extent of polarization affects the position of the low-frequency features of the infrared spectrum of water in NU-1500-Cr and is responsible for the significant infrared intensity between 2800 and 3100 cm^{-1}. This increased intensity can be explained by considering that the MB-pol dipole moment calculated for the water molecules bound to the charge-modified SBUs of NU-1500-Cr is $\sim$4.0 D which is significantly larger than the value of 2.7 D obtained from MB-pol simulations of liquid water.[104] Missing low-frequency tails in the infrared spectra of water adsorbed in Co_2Cl_2BTDD and ZIF-90 can also be observed in previous simulation studies[95,100]. However, in the case of Co_2Cl_2BTDD and ZIF-90 these low-frequency tails are less intense than in the infrared spectra of water in NU-1500-Cr which may possibly be attributed to the lower oxidation states of Co^{2+} and Zn^{2+} compared to Cr^{3+} as

well as to different degree of structural disorder in the experimental samples.

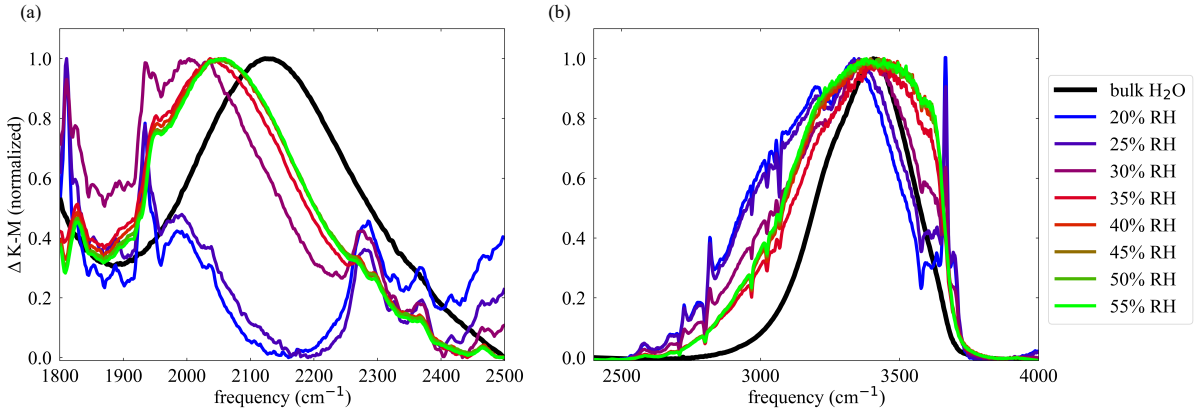

Figure 2.5. Infrared spectra of water confined in NU-1500-Cr as a function of RH compared to bulk water. Spectra were normalized to the maximum IR signal after subtracting a spectrum of activated NU-1500-Cr to reduce the influence of framework peaks in (a) the bend + libration combination band, and (b) the OH-stretch region region of the spectrum.

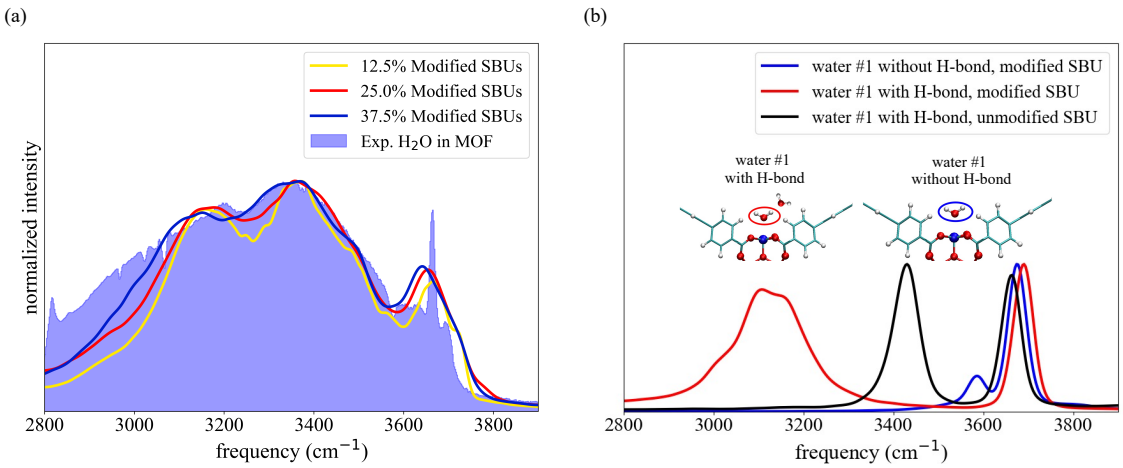

Figure 2.6. Simulated water spectra in NU-1500-Cr with modified SBUs. (a) Simulated water spectra with 12.5% (yellow), 25.0% (red), and 37.5% modified SBUs in the framework and experimental water spectrum (shaded purple) at 25% RH. (b) Spectra of water #1 binding to a modified SBU without (blue) and with (red) forming a hydrogen-bond with a neighboring water molecule, and binding to a unmodified SBU with forming a hydrogen-bond with a neighboring water molecule (black).

2.4 Conclusions

We used advanced molecular dynamics simulations in combination with infrared spectroscopy to investigate the adsorption mechanisms of water in NU-1500-Cr. We found that the confining effects of the framework modulate the thermodynamic properties of water as a function of relative humidity. In particular, the loss of entropy associated with the restricted motion of water molecules inside the NU-1500-Cr pores is compensated by favorable framework-water and water-water interactions at low and high RH, respectively. The variation of both adsorption enthalpy and water entropy directly correlates with the adsorption mechanism. The initial hydration stage occurs with water molecules saturating the Cr^{3+} open sites of the framework. With increasing RH, water molecules first form chain-like structures that emanate from the Cr^{3+}-bound water molecules and fill the narrow channels composed of two adjacent SBUs which are parallel to the hexagonal pores, and the aryl groups of the organic linkers. Due to favorable interactions between water the aryl groups of the framework, type-A channels accommodate all the adsorbed water molecules up to 33% RH. Above 33% RH, filling of the hexagonal pores begins with a steep adsorption step that ends at $\sim$37% RH.

Further insights into the confining effects of the framework and the properties of the hydrogen-bond networks developed by water inside the NU-1500-Cr pores were gained from monitoring the evolution of the infrared spectra of adsorbed water as a function of RH. The bend + libration combination band indicates that the hydrogen-bond networks become more developed as the RH increases, which is consistent with the decrease in water entropy and the formation of more tetrahedral spatial arrangements of water inside the pores. While the simulated spectra reproduce the main features of the experimental lineshapes, they miss intensity in the low-frequency region between 2800 and 3100 cm^{-1}. We found that the low-frequency tail in the experimental infrared spectra can be recovered by MD simulations carried out with charge-modified SBUs which can effectively mimic possible structural disorder in the experimental samples. We therefore demonstrated the power of combining MD simulations and IR

spectroscopy to gain molecular-level insights into the nature of framework–water interactions which are difficult to obtain from crystallography.

Since the steep uptake in the adsorption isotherm corresponds to the onset of pore filling, our results indicate that decorating the pores with hydrophilic functional groups may prevent water molecules from entering type-A channels at the early stage of the adsorption process which, in turn, can improve the ability of NU-1500-Cr to harvest water from air by shifting the adsorption step to lower RH values.

2.5 Supporting Information

Supplementary information is available for this paper at https://doi.org/10.1038/s42004-023-00870-0.

2.6 Data availability

Any data generated and analyzed for this study that are not included in this Article and its Supplementary Information are available from the authors upon request.

2.7 Code availability

The molecular models used in the MD simulations carried out with in-house software based on the DL_POLY_2 simulation package are publicly available on GitHub (https://github.com/paesanilab/ Data_Repository/tree/main/NU-1500) in the format for the MBX[112] interface with LAMMPS.[113] All computer codes used in the analysis presented in this study are available from the authors upon request.

2.8 Acknowledgment

We are grateful to Kelly Hunter, Hilliary Frank, Jierui Zhang, and Martina Lessio for stimulating discussions about computer simulations of MOFs, and Timur Islamoglu for

discussions about the characterization of NU-1500-Cr. **Funding:** This research was supported by the Department of Energy, Basic Energy Science (BES) Office through awards no. DE-SC0022332 (C.-H.H., H.X., Z.C, O.K.F, and F.P.) and DE-SC0019333 (M.L.V. and W.X.). All simulations used resources of the National Energy Research Scientific Computing Center (NERSC), supported by Department of Energy BES Office under contract DE-AC02-05CH11231 and the Triton Shared Computing Cluster (TSCC) at the San Diego Supercomputer Center (SDSC).

2.9 Author contributions

C.-H.H. performed simulations. M.L.V. performed infrared spectroscopy measurements. Z.C.and H.X. prepared and characterized the NU-1500-Cr sample. W.X. and F.P. conceived and designed research and administered the project. W.X., O.K.F, and F.P. acquired funding. C.-H.H., M.L.V., W.X., and F.P. analyzed and discussed the results and wrote the paper, with feedback from H.X., Z.C, and O.K.F.

2.10 Competing interests

The authors declare that they have no competing interests.

Chapter 2, in full, is a reprint of the material as it appears in "Structure and thermodynamics of water adsorption in NU-1500-Cr", C.-H. Ho, M. L. Valentine, Z. Chen, H. Xie, O. Farha, W. Xiong, F. Paesani; Commun. Chem. 6, 70, 2023. The dissertation author was the primary investigator and author of this paper.

Chapter 3

Humidity-responsive polymorphism in CALF-20: A resilient MOF physisorbent for CO_2 capture.

3.1 Introduction

There is a need for effective solutions to capture CO_2 from both industrial sources and the surrounding atmosphere to curb atmospheric CO_2 levels and mitigate climate change.[114,115] Selective CO_2 capture poses challenges due to the low partial pressure of CO_2 compared to other molecular species, which can hinder adsorption behavior by competing for adsorption sites or inducing changes in the sorbent itself.[116] This challenge is particularly pronounced in the direct capture of CO_2 from the air, where interference from more abundant molecules like water exacerbates the issue. Therefore, economically viable CO_2 solutions must exhibit high selectivity for CO_2 and durability in the presence of more abundant species, while also minimizing the energy cost for regeneration.

Metal-organic frameworks (MOFs) present promising porous sorbents for CO_2 due to their customizable structure and chemistry.[117–119] Their pore size and shape can be tailored to facilitate selective physisorption, thereby avoiding the high energy requirement associated with the regeneration of chemically selective chemisorption.[120–122] Among the various MOFs evaluated for CO_2 capture, CALF-20, a zinc-triazole-oxalate-based MOF, has emerged as a

promising candidate for large-scale CO_2 capture due to its robust sorption performance under industrially relevant conditions.[123] Specifically, it exhibits highly selective CO_2 physisorption with low energy requirements for regeneration, attributed to the hydrophobic nature of its pores. The CALF-20 structure comprises zinc triazole layers in the bc-plane connected in the c-direction by bis-bidentate oxalate anions, with the zinc cation coordinated by three nitrogen atoms from three triazole anions and two oxygen atoms from a bis-bidentate oxalate anion.

In the published paper titled "Humidity-responsive polymorphism in CALF-20: A resilient MOF physisorbent for CO_2 capture," extensive discussions on phase transformation and experimental details have been provided. However, this chapter places greater emphasis on computational insights into the thermodynamic and dynamic properties of CO_2 within different phases of CALF-20. Our study offers direct insights into the effects of unit cell volume on the thermodynamic and dynamic properties of CO_2, providing valuable information for the rational design of MOFs for guest molecule adsorption.

3.2 Methods

3.2.1 Molecular models

Both α- and β-CALF-20 are modeled using flexible force fields. The structure of α-CALF-20 was obtained from the Cambridge Structural Database (2084733.cif), whereas the crystallographic information of β-CALF-20 was acquired as described in the experimental section. The crystallographic structures were optimized using density functional theory (DFT) with the PBE exchange-correlation functional[81] combined with the D3 dispersion correction[82] in periodic boundary conditions, as implemented in the Vienna Ab initio Simulation Package (VASP).[77–80], VASP calculations were performed using projector-augmented wave (PAW) method[83,84] with 700 eV kinetic energy cutoff and a 3x3x3 k-point grid and convergence criterion of net atomic force less than 0.03 eV/Å. The point charges of the force field were obtained from Charge Model 5 (CM5)[44] calculations carried out with Gaussian 16 using the ωB97X-D

functional[31] in combination with def2-TZVP basis set[32] for a cluster model of α-CALF-20 (see Supplementary Figures S1 for details). The bonded parameters of the force field associated with the Zn atoms were obtained using a genetic algorithm by fitting to single-point energies calculated at the ωB97X-D/def2-TZVP level of theory with Gaussian 16 for 125 distorted configurations of the same α-CALF-20 cluster model used in the CM5 calculations. The Universal Force Field (UFF)[30] was used for the Lennard-Jones (LJ) coefficients of the Zn atoms, while the General Amber Force Field (GAFF)[29] was used for all bonded and LJ terms related to the linker atoms.

CO_2 was modeled using the many-body energy potential energy function (MB-nrg PEF) of reference 124 and 125, which has been shown to accurately reproduce several experimental data including the second virial coefficient and the structure of liquid CO_2 at different pressures. The LJ parameters between the CO_2 molecules and framework atoms were calculated according to the Lorentz-Berthelot mixing rules using the LJ parameters of the Transferable Potentials for Phase Equilibria (TraPPE) model for CO_2.[126]

3.2.2 Molecular dynamic simulations

All MD simulations were carried out with the Large-scale Atomic/Molecular Massively Parallel Simulator (LAMMPS) package[113] interfaced with the MBX library for a system consisting of 2x2x2 primitive cells of α- and β-CALF-20 in periodic boundary conditions and varying CO_2 loadings, ranging from 0.18 to 3.52 mmol/g (equivalent to 1 to 20 CO_2 molecules in a $2\times2\times2$ primitive cell). Various structural, thermodynamic, and dynamical properties were calculated by carrying out MD simulations in the isothermal-isobaric (constant number of atoms, pressure, and temperature, NPT); canonical (constant number of atoms, volume, and temperature, NVT); and microcanonical (constant number of atoms, volume, and total energy, NVE) ensembles. The temperature in the NPT and NVT simulations was controlled by a global Nosé-Hoover chain of four thermostats. The pressure in the NPT simulations was maintained by a global NosNosé-Hoover barostat. The equations of motion were propagated with a time step of 0.2 fs

according to the velocity-Verlet algorithm.

At each CO_2 loading, the initial positions of the CO_2 molecules were generated using Packmol[91,92], enforcing a uniform distribution of CO_2 molecules across all MOF pores. Each system was then randomized in the NVT ensemble at 343 K for 20 ps, which was followed by another 20 ps at 295 K. Each system was then further equilibrated in the NPT ensemble at 1 atm and 295 K for 100 ps. The lattice parameters and adsorption heat were calculated from 10 ns trajectories carried out in the NPT ensemble at 1 atm and 295 K. The adsorption heat at a given loading is calculated by

$$\Delta H_{ads} = \frac{U(\mathrm{MOF}+\mathrm{CO_2}) - U(\mathrm{MOF}) - N \times U(\mathrm{CO_2}) - N \times \mathrm{R}T}{N} \tag{3.1}$$

, where N is the number of CO_2 molecules, R is the ideal gas constant, T is the temperature, U(MOF), U(CO_2), and U(MOF+CO_2) are the internal energies of empty MOF, single CO_2 molecule, and MOF loaded with CO_2 molecules at a given loading, respectively. The diffusion coefficients were calculated by averaging over 200 independent 50 ps trajectories performed in the NVE ensemble according to the velocity autocorrelation fucntion,

$$D_{tot} = \frac{1}{3}\int_0^\infty \langle \vec{v}_c(0) \cdot \vec{v}_c(t) \rangle dt \tag{3.2}$$

, where $\langle \vec{v}_c(0) \cdot \vec{v}_c(t) \rangle$ is the ensemble-averaged classical velocity autocorrelation function. The diffusion coefficients along a given direction were calcu-lated by

$$D_u = \int_0^\infty \langle v_u(0) v_u(t) \rangle dt \tag{3.3}$$

, where v_u is the projected velocity to the unit vector of the given direction u.

3.3 Results and discussions

Figure 3.1(A) displays the adsorption heat calculated for CO_2 adsorbed in the α- and β-CALF-20 frameworks at different loadings. The adsorption heat calculated for the lowest loading of CO_2 in the α-phase (36.7 kJ/mol) agrees with the experimental zero-loading heat of adsorption 39 kJ/mol. The adsorption heat values within the same phase are not significantly affected by the CO_2 loading, suggesting that CO_2-CO_2 interactions play a minor role in the adsorption process. This behavior can be attributed to the non-polar nature of CO_2, which results in limited dipole-dipole interaction energies between CO_2 molecules present in the MOF pores. The β-phase exhibits a consistently higher adsorption heat than the α-phase. To gain insights into the difference in adsorption heat between α- and β-CALF-20, we analyzed the radial distribution functions (RDFs) of all possible atom pairs between CO_2 and the two frameworks at the lowest CO_2 loading (i.e., 0.18 mmol/g or 1 CO_2 molecule per $2\times2\times2$ primitive cell). The analysis of the RDFs suggests that both α- and β-phase frameworks attract CO_2 mainly through interactions with the oxygen atom of the oxalate group, as evident from the position of the first peak in the RDFs, which appears at the shortest distance among all atom pairs (see Supporting Information S7 for all RDFs). The RDFs representing the spatial correlation between the carbon atom of CO_2 and the oxalate oxygen in both α- and β-CALF-20 frameworks are shown in Figure 3.1(B). While the first peak appears at nearly 3 Å for both phases, the β-phase displays a higher peak than the α-phase. Moreover, the RDF for the α-phase displays two subsequent peaks at 4.2 Å and 5.6 Å, while the RDF for the β-phase only displays a single peak at 5.0 Å with similar amplitude to the peak observed at 5.6 Å for the α-phase. The difference between the RDFs of the α- and β-phases can be attributed to the difference in the distances between the two oxalate oxygens that interact with the CO_2 molecule. Based on the crystallographic data, we found that the distances between the two oxalate oxygens located across a pore are different for the α- and β-phases. Specifically, these distances range from 5.7 to 6.5 Å for the β-phase, which allows a CO_2 molecule to simultaneously be in close proximity to both oxalate oxygens across the pore.

In contrast, the distances between the two oxalate oxygens across the pore for the α-phase range from 7.0 to 8.1 Å, which implies that a CO_2 molecule can only be close to one of the two oxalate oxygens. It thus follows that the difference in adsorption heat between α- and β-CALF-20 can be attributed to the smaller unit cell volume of the β-phase.

Further insights into the effects that the different unit cell volumes of α- and β-CALF-20 have on the adsorption of CO_2 can be gained by examining the CO_2 diffusion in the pores of both phases. Figure 3.2(A) shows the total diffusion coefficients as a function of CO_2 loading for both α- and β-CALF-20. The total diffusion coefficients for both phases decrease as more CO_2 molecules are adsorbed, which can be explained by the increase in excluded volume. This trend is similar to the behavior observed for methane, hexane, and benzene at high loadings in IRMOF-1.[127] Interestingly, at low loading, CO_2 molecules in the α-phase diffuse more rapidly than in the β-phase, which can be attributed to smaller adsorption heat and larger unit cell volume of the α-phase. As the loading increases, the difference in total diffusion coefficients between α- and β-phases becomes smaller. Figure 4(B) shows that, due to confinement, the main direction for CO_2 diffusion is along the [100] direction (i.e., a-direction), with the CO_2 molecules at low loading moving faster in the α-phase than in the β-phase, as already inferred by the analysis of the total diffusion coefficient. The anisotropy in the CO_2 diffusion can be explained by considering that the pore along the [100] direction is significantly wider than in the other two directions.

In summary, the differences observed between α- and β-CALF-20 provide some general insights for the design of CO_2-capturing frameworks. It suggests that frameworks with small unit cell volume benefit from higher affinity to CO_2, but it comes at a cost of reduced diffusion rates of CO_2 inside the framework.

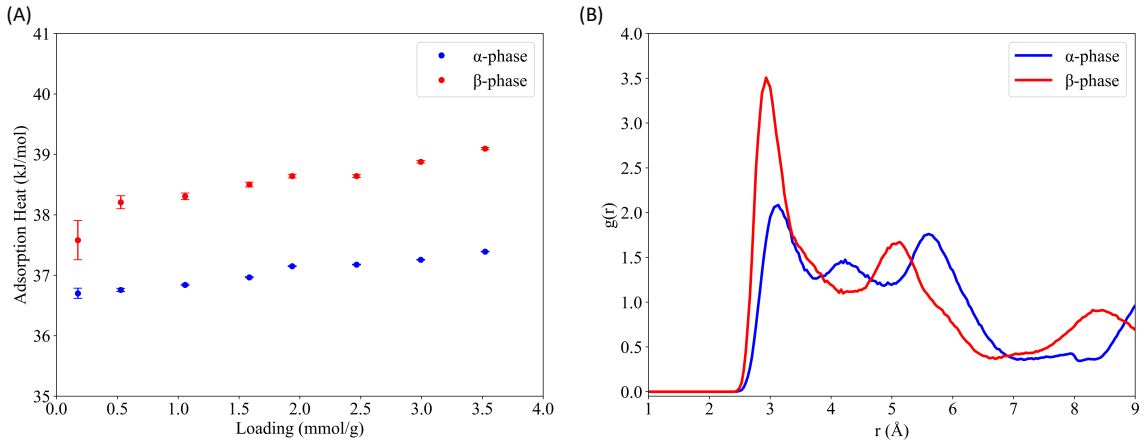

Figure 3.1. Simulated thermodynamic and dynamical properties of CO_2 confined in α- and β-CALF-20. (a) Adsorption heat as a function of CO_2 loading. (b) RDFs between the carbon atom in CO_2 and the oxygen atom in the framework in α- and β-CALF-20.

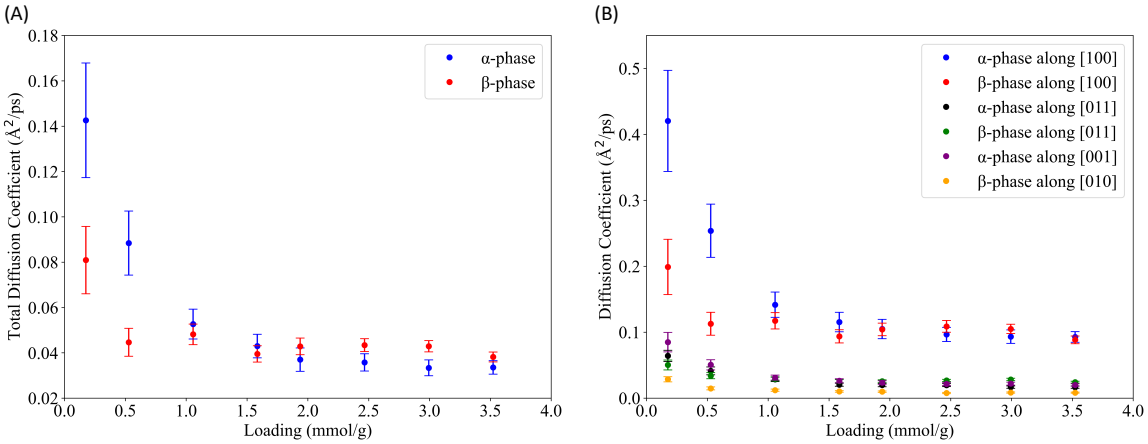

Figure 3.2. Diffusion coefficients of CO_2 within α- and β-CALF-20 (a) Total diffusion coefficients of CO_2 loading. (b) Diffusion coefficients of CO_2 along pore directions in α- and β-CALF-20.

3.4 Associated content

The Supporting Information is available free of charge at https://pubs.acs.org/doi/10.1021/acsmaterialslett.3c00930. Details of sample preparation, aging environments, X-ray scattering experiment and analysis, computation, and experimental gas adsorption isotherms (PDF), α-CALF-20 (CIF), β-CALF-20 (CIF).

3.5 Acknowledgement

This work was supported by the U.S. Department of Energy (DOE), Office of Science, Basic Energy Sciences (BES), DESC0022332 of Spatiotemporal Dynamics of CO_2 Capture by Sorbents: Multimodal, in situ and Operando Measurements. Use of beamlines 11-BM (mail-in) and 11-ID-B of the Advanced Photon Source at Argonne National Laboratory was supported by the U.S. Department of Energy, Office of Science, Office of Basic Energy Sciences, under Contract No. DE-AC02-06CH11357.

Chapter 3, in full, is a part of the material as it appears in "Reversible humidity-dependent pore breathing transformation in CALF-20, a resilient MOF physisorbent for CO_2 capture", Z. Chen, C.-H. Ho, X. Wang, S. M. Vornholt, T. Islamoglu, O. F. Farha, F. Paesani, K. W. Chapman; ACS Mater. Lett. 5, 2942, 2023. The dissertation author was the primary investigator and author of this paper.

Chapter 4

Elucidating the competitive adsorption of H_2O and CO_2 in CALF-20: New insights for enhanced carbon capture metal-organic frameworks.

4.1 Introduction

The increasing concentration of carbon dioxide (CO_2) in the atmosphere is a significant contributor to climate change.[128] Various strategies have been developed to reduce atmospheric CO_2 concentration, including leveraging the chemical properties of CO_2 to convert it into valuable chemicals.[129,130] Another strategy is the storage of CO_2, which involves long-term sequestration in geological media or sedimentary rocks.[131,132] However, the nonpolar nature of CO_2 poses challenges for effective and efficient storage, as high pressure is typically required to convert CO_2 from its gas phase to a supercritical fluid, complicating the engineering of storage systems.[133–135]

Metal-organic frameworks (MOFs) have emerged as a promising class of materials for CO_2 capture due to their versatile physical and chemical properties. Several MOFs, including Mg_2(dobpdc),[136] and SIFSIX-3-M,[137,138] have been shown to be promising materials for CO_2 capture. A recent study reported the synthesis of CALF-20, a Zn-based framework connected by triazolates and oxalate groups, which exhibits high scalability and stability for CO_2 capture.[123]

Unlike many MOFs tested for CO_2 capture that degrade in the presence of water,[139,140] CALF-20 stands out due to its accessibility in terms of the required synthesis reagents and its exceptional stability, even in the presence of steam. This unique combination of features has generated significant research interest in CALF-20 as a promising candidate for applications related to CO_2 capture.[141,142]

While experimental studies have demonstrated the potential of CALF-20 for CO_2 capture,[123,143] the performance of CALF-20 in real-world applications can be compromised due to the adsorption of other molecules present in the air, such as water (H_2O). Given the properties and partial pressure of H_2O in the atmosphere, it is thus crucial to evaluate the competitive adsorption of H_2O and CO_2 within the CALF-20 framework under realistic conditions. However, characterizing the underlying adsorption process at the molecular level poses experimental challenges due to the competing interactions between H_2O and CO_2 with the framework. Furthermore, although the amount of H_2O and CO_2 adsorbed within the framework is primarily influenced by the corresponding partial pressure of each species, it is also affected by the partial pressure of the other species due to cooperative effects. This interplay makes it challenging to control the adsorption of one species without affecting the other by independently regulating the partial pressure of each species. It follows that the competition between H_2O and CO_2 within the CALF-20 framework makes it difficult to experimentally study concentration-dependent thermodynamic and dynamic properties of both species.[127,144–146]

In this study, we investigate competing effects in the behavior of H_2O and CO_2 adsorbed in CALF-20 using advanced molecular dynamics (MD) simulations carried out with data-driven many-body potential energy functions (PEFs) that accurately predict the properties of water[34–36,86,87,147] and carbon dioxide[124,125] across a wide range of thermodynamic conditions and mixture compositions. CALF-20 is modeled as a flexible framework that can accommodate potential structural changes, which may yield distinct thermodynamic and dynamic properties of guest molecules as concluded in several studies.[148–150] These simulations allow us to precisely disentangle the competitive adsorption between H_2O and CO_2 and provide insights at the

molecular level, which can inform the design of MOFs specifically optimized for carbon capture applications.

4.2 Methods

4.2.1 Molecular models

CALF-20 was modeled using a flexible force field, with the structure of the framework taken from the crystallographic data reported in Ref. 123. The geometry optimization was carried out with the Vienna Ab initio Simulation Package (VASP)[77–80] in periodic boundary conditions using density functional theory (DFT). The PBE exchange-correlation functional[81] combined with the D3 dispersion correction[82] was used for these calculations. The VASP calculations were performed on a $3\times3\times3$ k-point grid with a 700 eV kinetic energy cutoff using the projector-augmented wave (PAW) method.[83,84]

The atomic point charges for the force field were obtained using the Charge Model 5 (CM5)[44] as implemented in Gaussian 16.[85] This was done by performing DFT calculations on a cluster model of CALF-20 (see Figure S1 of the Supporting Information) using the ωB97X-D functional[31] in combination with the def2-TZVP basis set.[32] Following Ref. 151, the bonded parameters of the force field associated with the Zn atoms were determined using a genetic algorithm.[152,153] A similar philosophy was also adopted in the development of MOF-FF parameters.[154] The parameterization involved fitting single-point energies calculated at the ωB97X-D/def2-TZVP level of theory with Gaussian 16 for 125 distorted configurations of the cluster model used in the CM5 calculations. The Lennard-Jones (LJ) parameters of the Zn atoms were acquired from the Universal Force Field (UFF)[30]. All bonded and LJ parameters of atoms other than Zn were acquired from the General Amber Force Field (GAFF).[29]

The MB-pol[34–36] and MB-nrg[124,125] data-driven many-body PEFs were used to model the H_2O and CO_2 molecules, respectively. Previous studies have demonstrated that these PEFs are transferable across the different phases of pure H_2O[86,87,104,147] and CO_2,[124,125] able to

reproduce the properties of H_2O and CO_2 mixtures,[124] and accurately predict the behavior of H_2O[95,102,146] and CO_2[119] molecules in MOFs.

Within our molecular models, framework–H_2O and framework–CO_2 interactions were described by electrostatic and LJ terms. By construction, the electrostatic terms of the MB-pol and MB-nrg PEFs include terms representing permanent and induced (i.e., polarization) contributions. The LJ parameters between the framework atoms and the water molecules were obtained by applying the Lorentz-Berthelot mixing rules using the LJ parameters of the TIP4P/2005 water model,[155] which was shown to be the closest point-charge model to the MB-pol PEF of H_2O.[156] Similarly, the LJ parameters between the CO_2 molecules and framework atoms were calculated according to the Lorentz-Berthelot mixing rules using the LJ parameters of the Transferable Potentials for Phase Equilibria (TraPPE) model for CO_2.[126]

4.2.2 Molecular dynamic simulations

All MD simulations were carried out with the Large-scale Atomic/Molecular Massively Parallel Simulator (LAMMPS)[113] package interfaced with the MBX C++ library.[112] The system consisted of 2×2×2 primitive cells (17.83 Å× 19.39 Å× 18.97 Å) in periodic boundary conditions. Various structural, thermodynamic, and dynamical properties were calculated by carrying out MD simulations in the isothermal-isostress ($N\sigma T$: constant number of atoms, temperature, and stress), canonical (NVT: constant number of atoms, volume, and temperature), and microcanonical (NVE: constant number of atoms, volume, and energy) ensembles. The temperature in the $N\sigma T$ and NVT simulations was controlled by a global Nosé-Hoover chain of four thermostats with a characteristic time of 20 fs. The pressure in the $N\sigma T$ simulations was maintained by a global Nosé-Hoover chain of three barostats with a characteristic time of 200 fs.[89] The equations of motion were propagated with a time step of 0.2 fs according to the velocity-Verlet algorithm.[157]

For the competitive adsorption simulations, the initial positions of the H_2O and CO_2 molecules were generated using Packmol,[91,92] enforcing a uniform distribution of both guest

species across all CALF-20 void spaces. For each system, the positions of the H_2O and CO_2 molecules were subsequently randomized. This was done by conducting a series of three short MD simulations in the NVT ensemble at 1000 K (50 ps), 500 K (20 ps), and 295 K (20 ps). Each system was then subjected to further equilibration in the $N\sigma T$ ensemble at 1 atm and 295 K for 100 ps. The average lattice parameters were calculated from 1 ns trajectories carried out at 1 atm in the $N\sigma T$ ensemble and are listed in Table S5 of the Supporting Information. We followed the same protocol to equilibrate the corresponding systems containing only H_2O or CO_2 molecules, with the lattice parameters fixed at the values obtained from the competitive adsorption simulations. The nonbonded interactions were truncated at an atom-atom distance of 9.0 Å, and the long-range electrostatic interactions were treated using the particle mesh Ewald method as implemented in MBX.[112,158,159] The entropy as well as all dynamical properties were calculated by averaging over 200 independent 50 ps trajectories performed in the NVE ensemble, with the volume fixed at the average value calculated from the corresponding competitive adsorption simulations. The entropy was calculated as a function of relative humidity (RH) using the two-phase thermodynamic (2PT) model, which decomposes the density of states of H_2O and CO_2 molecules into gas-like and solid-like components and enables the calculation of thermodynamic properties accordingly.[93] The diffusion coefficient as a function of RH was calculated by averaging over the 200 trajectories performed in the NVE ensemble according to the following Green-Kubo relation:[160]

$$D_{tot} = \frac{1}{3}\int_0^\infty \langle \vec{v}_c(0)\cdot\vec{v}_c(t)\rangle dt, \tag{4.1}$$

Here, $\vec{v}_c$ is the center-of-mass velocity, and the $\langle \vec{v}_c(0)\cdot\vec{v}_c(t)\rangle$ is the ensemble-averaged classical velocity autocorrelation function. The H_2O and CO_2 adsorption enthalpies were calculated by averaging 20 trajectories of 50 ps each performed in the $N\sigma T$ ensemble according to

$$\Delta H_{ads} = \frac{U(\mathrm{MOF}+\mathrm{H_2O/CO_2}) - U(\mathrm{MOF}) - N\times U(\mathrm{H_2O/CO_2}) - N\times \mathrm{R}T}{N}, \tag{4.2}$$

Here, N is the number of H_2O or CO_2 molecules, R is the ideal gas constant, T is the temperature, U(MOF), U(H_2O/CO_2), and U(MOF + H_2O/CO_2) are the averaged internal energies of the empty MOF, single H_2O or CO_2 molecule, and MOF loaded with H_2O or CO_2 molecules, respectively. The average interaction energy of CO_2 at a given RH values was calculated according to

$$E_{int} = \frac{U(\mathrm{MOF} + \mathrm{H_2O} + \mathrm{CO_2}) - U(\mathrm{MOF} + \mathrm{H_2O}) - N \times U(\mathrm{CO_2})}{N}, \tag{4.3}$$

where N is the number of CO_2 molecules, U(MOF + H_2O + CO_2), U(MOF + H_2O), and U(CO_2), are the average internal energies of MOF loaded with H_2O and CO_2, MOF loaded with H_2O, and single CO_2, respectively. The orientational correlation functions were calculated by averaging over the NVE trajectories according to[161]

$$C_2(t) = \langle P_2[\vec{e}(0) \cdot \vec{e}(t)] \rangle, \tag{4.4}$$

where $\vec{e}$ is a unit vector along one of the OH or CO bonds of a H_2O or CO_2 molecule, P_2 is the second order Legendre polynomial, and $\langle ... \rangle$ represents the ensemble average over all OH or CO bonds at a given time t.

For all properties derived from the $N\sigma T$ simulations, at each relative humidity the trajectory was divided in twenty blocks of equal length, and the error bars were calculated as 95% confidence intervals obtained from the standard error of the mean of the blocks. For all properties derived from the NVE simulations, the error bars were calculated as 95% confidence intervals obtained from the standard error of the mean of 200 independent trajectories.

4.3 Results and discussions

Figure 4.1A displays the experimental competitive adsorption of H_2O and CO_2 in CALF-20 as a function of relative humidity measured at 295 K and 97 kPa.[123] Notably, the amount of CO_2 adsorbed by the CALF-20 framework is influenced by the relative humidity, despite the

constant CO_2 pressure. To explore the factors contributing to the competitive behavior of H_2O and CO_2 within the CALF-20 framework, we examined the individual adsorption enthalpies as well as the H_2O and CO_2 radial distribution functions (RDFs). The adsorption enthalpies calculated for a single H_2O and a single CO_2 molecule in CALF-20 are -7.59 kcal/mol and -8.66 kcal/mol, respectively. These values align with the reported binding energies of H_2O and CO_2 within the CALF-20 framework 6.95 kcal/mol and 8.25 kcal/mol, respectively,[123] indicating that CALF-20 has a stronger affinity for CO_2 compared to H_2O. The H_2O–framework and CO_2–framework RDFs presented in Figure S3 of the Supporting Information indicate that the oxygen atoms of the oxalate groups of the framework serve as the most favorable binding sites for both H_2O and CO_2. Therefore, the competitive behavior of H_2O and CO_2 in CALF-20 can be attributed to the presence of similar preferred void regions and comparable interaction energies with the framework. Given the accuracy of the MB-pol and MB-nrg PEFs in describing the behavior of H_2O and CO_2, respectively, in heterogeneous environments, the disparity in permanent dipole moments between H_2O and CO_2 suggests that frameworks with less polarized charge distributions may exhibit higher affinities for CO_2 than H_2O. This observation implies

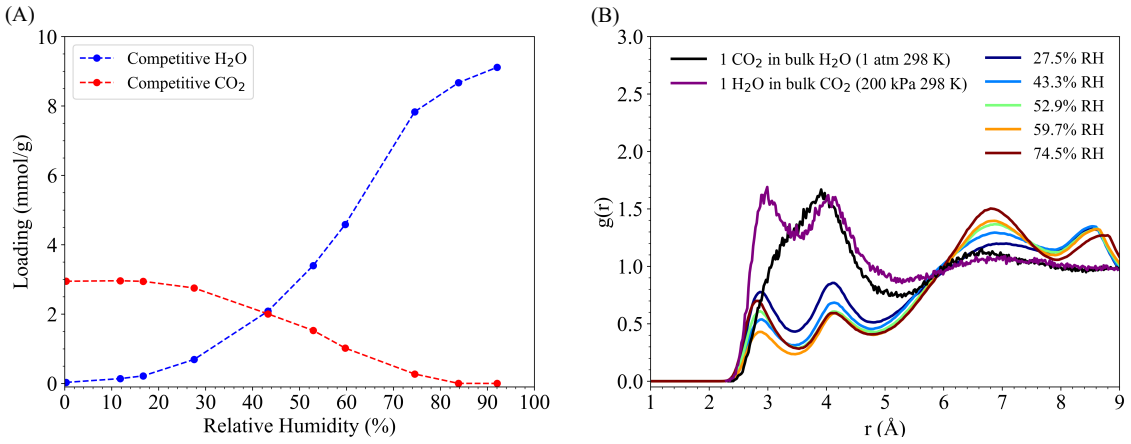

Figure 4.1. (A) Experimental competitive adsorption of H_2O and CO_2 in CALF-20 as a function of relative humidity.[123] (B) Radial distribution functions showing the probability of finding the oxygen atom (OW) of a H_2O molecule at a distance r from the carbon atom (CC) of a CO_2 molecule within the framework. For comparison, the corresponding radial distribution functions for dilute H_2O in liquid CO_2 and dilute CO_2 in liquid H_2O from Ref. 124 are also shown.

that frameworks composed of metal ions in a low oxidation state coordinated with atoms with low electronegativity may exhibit a higher affinity for CO_2.

Further insights into the influence of the framework on the adsorption of H_2O and CO_2 can be obtained by investigating H_2O and CO_2 mixtures across a broad range of relative humidity values (from 27.5% to 74.5%). As shown in Figure 4.1B, the general lineshapes of RDFs between the oxygen atom (OW) of any H_2O molecule and the carbon atom (CC) of any CO_2 molecule, are effectively independent of the RH values and reveal a notable structural reorganization of both H_2O and CO_2 molecules. The first peak at $\sim$ 3.0 Å corresponds to the most probable distance at which an OW atom directly interacts with a CC atom, while the second peak at $\sim$ 4.0 Å arises from water molecules that form hydrogen bonds with the CO_2 oxygen (OC). The RDFs remain structured at large OW–CC separations (greater than 6 Å) due to the formation of hydrogen-bonds among water molecules. This is influenced by the confining effects exerted by the framework, as well as volume exclusion effects exerted by the CO_2 molecules present within the framework. In contrast, the corresponding RDFs calculated for dilute CO_2 in liquid H_2O at 1 atm and dilute H_2O in liquid CO_2 at 200 kPa,[124] which correspond to the black and purple curves in Figure 1B, respectively, exhibit less pronounced structural features at long distances. At short distances, the RDF of dilute H_2O in liquid CO_2 displays a bimodal lineshape similar to that observed in the H_2O–CO_2 mixtures within the CALF-20 framework, while the RDF of dilute CO_2 in liquid H_2O lacks the peak at approximately 3.0 Å. Consequently, under ambient conditions, the confining effects of the CALF-20 framework result in a resemblance between the short-ranged structures of H_2O and CO_2 molecules and their high-pressure structures in bulk solutions, while also promoting the formation of long-ranged structural patterns. Furthermore, mutual volume exclusion effects between the H_2O and CO_2 molecules within the CALF-20 framework are evident from the OW–CC RDFs, as the oxygen atoms of the H_2O molecules are prevented from approaching closer than $\sim$2.1 Å to the carbon atoms of the CO_2 molecules.

To disentangle the effects resulting from mutual volume exclusion of H_2O and CO_2 molecules within the framework, we investigated systems composed solely of either H_2O or

CO_2, keeping their loadings as in the corresponding MD simulations described above for the mixtures at different RH values. In the following, these systems are labeled according to the RH values of the corresponding mixed systems analyzed in Figure 4.1. To prevent potential volume changes resulting from different amounts of guest molecules present within the framework, the lattice parameters for the systems composed solely of either H_2O or CO_2 were fixed at the average values obtained from the MD simulations of the corresponding mixed systems. Volume exclusion effects can be elucidated by comparing the hydrogen-bond topologies established by the H_2O molecules within the framework in the presence and absence of CO_2 molecules. In this analysis, each water molecule is classified as either a donor (nD) or an acceptor (mA) based on the type (D and A) and number (n and m) of hydrogen bonds it is engaged in. Figure 4.2A shows the probability of observing the 0D-0A topology (i.e., water molecules not engaged in any hydrogen bond) in the presence and absence of CO_2 molecules as a function of relative humidity. The percentage of the 0D-0A topology decreases with increasing RH, regardless of the presence of CO_2. This decrease can be attributed to the larger number of water molecules present within the framework, leading to the formation of more compact and connected hydrogen-bond networks. A similar trend was also observed for water adsorbed in NU-1500-Cr.[146] Across the range between 27.5% and 59.7% RH the differences in the percentages of the 0D-0A topology indicate that the water molecules tend to form a more connected hydrogen-bond network in the presence of CO_2 compared to when CO_2 is absent. The small difference in the percentage of the 0D-0A topology observed at 74.5% RH can be attributed to the overwhelmingly higher concentration of water, with a ratio of H_2O to CO_2 equal to 22:1. These findings indicate that the presence of CO_2 molecules within the framework pushes the H_2O molecules into more confined regions, consequently increasing the likelihood of establishing hydrogen bonds among them. A consistent conclusion can be drawn from Figure 4.2B, where the solid and dashed lines represent the OW–OW RDFs in the presence (solid line) and absence (dashed line) of CO_2 at different RH values, respectively. Although all RDFs exhibit a prominent peak at $\sim$2.8 Å, this peak is appreciably higher in the RDFs calculated in the presence of CO_2 across the range between

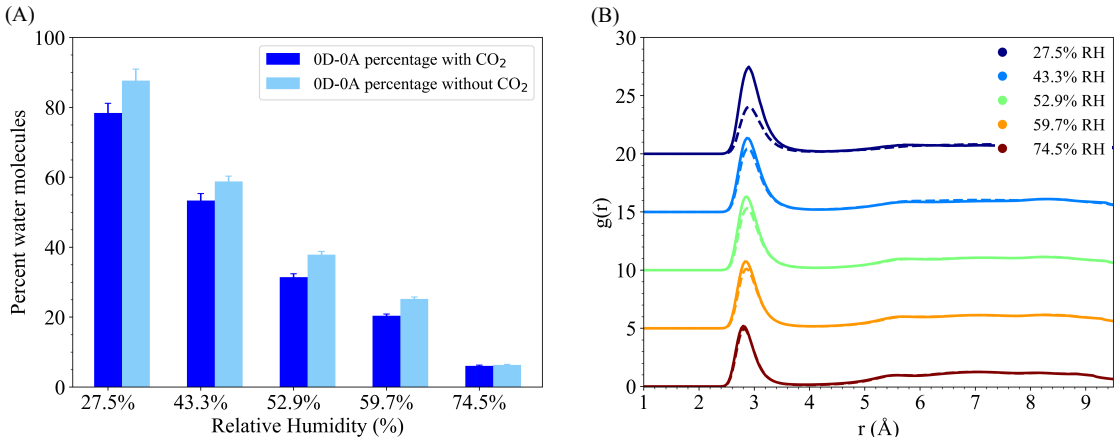

Figure 4.2. (A) Probability of the 0D-0A hydrogen-bond topology calculated as a function of relative humidity in the presence (dark blue) and absence (light blue) of CO_2 within the framework. (B) Water oxygen-oxygen (OW-OW) radial distribution function calculated as a function of relative humidity in the presence (solid line) and absence (dashed line) of CO_2 within the framework.

27.5% and 59.7% RH. The increased prominence of this peak can be attributed to the higher probability of finding H_2O molecules in close proximity to each other, which arises from the volume exclusion effects exerted by CO_2.

Additional insights into volume exclusion effects can be gained by examining the thermodynamics of H_2O and CO_2 adsorption in CALF-20. Figures 4.3A and 4.3B show the changes in entropy of H_2O and CO_2 molecules, respectively, as a function of relative humidity. As the relative humidity increases, the entropy of water decreases due to the formation of increasingly

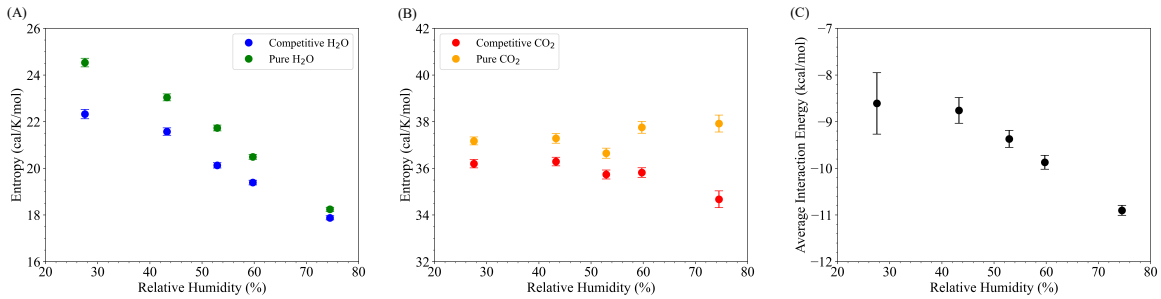

Figure 4.3. Entropy of H_2O (A) and CO_2 (B) molecules within the CALF-20 framework calculated as a function of relative humidity in the presence and absence of the corresponding competing species, i.e., CO_2 in (A) and H_2O in (B). (C) Average interaction energy of CO_2 molecules within the CALF-20 framework calculated as a function of relative humidity.

connected hydrogen-bond networks among a larger number of H_2O molecules, resulting in a more restricted motion, as indicated in the analyses of Figure 4.2A. A similar variation in the entropy of water was observed for water adsorbed in ZIF-90 and NU-1500-Cr.[102,146] As mentioned above, the presence of CO_2 molecules within the framework leads to a decrease in void space and the formation of a more connected hydrogen-bond network (Figure 4.2A). Consequently, the water entropy is consistently lower in the presence of CO_2 molecules within the framework, reflecting the more restricted motion of the H_2O molecules. In contrast, the entropy of CO_2 in the absence of H_2O is effectively independent of the amount of CO_2 present in the pore. Unlike H_2O molecules, which can form hydrogen bonds and engage in stronger interactions, CO_2 molecules mainly interact through weak van der Waals forces due to their nonpolar character. The entropy of CO_2 molecules issubstantially influenced by water only at high RH values, where most of the void space within the framework is occupied by water. Figure 4.3C shows that, as the relative humidity increases, the average interaction energy of the CO_2 molecules becomes more negative, indicating that the presence of water within the framework is energetically favorable for CO_2 adsorption. These favorable interactions can be traced back to the formation of weak hydrogen bonds between H_2O and CO_2 molecules, which is promoted by the confining environment provided by the CALF-20 framework as indicated by the RDFs shown in Figure 4.1B. As a result, the thermodynamic properties of CO_2 in the presence of H_2O indicate that the presence of H_2O is energetically favorable for CO_2 capture, but entropically unfavorable at high RH values.

The effects of framework confinement and volume exclusion on the dynamics of H_2O and CO_2 molecules within the framework can be better understood by examining the corresponding orientational correlation functions, $C_2(t)$ in Eq.4.4, shown in Figures 4.4A and 4.4B, respectively. The reorientation timescales for the H_2O molecules were determined by fitting $C_2(t)$ to a tri-exponential function,

$$C_2(t) = A_1 \cdot \exp(-t/\tau_1) + A_2 \cdot \exp(-t/\tau_2) + A_3 \cdot \exp(-t/\tau_3), \tag{4.5}$$

where τ_1, τ_2, and τ_3 listed in Table 4.1 can be assigned to the reorientation time scales associated with the librational motion, hydrogen-bond dynamics, and collective structural rearrangements, respectively. Due to the fact that the values of τ_3 exceed the total length of our NVE simulations, only the values of τ_1 and τ_2 can be precisely determined. As predicted by the time decay of $C_2(t)$ for water in Figure 4.4A, both τ_1 and τ_2 for water increase with increasing RH, regardless of the presence (solid line) or absence (dashed line) of CO_2 molecules within the framework.

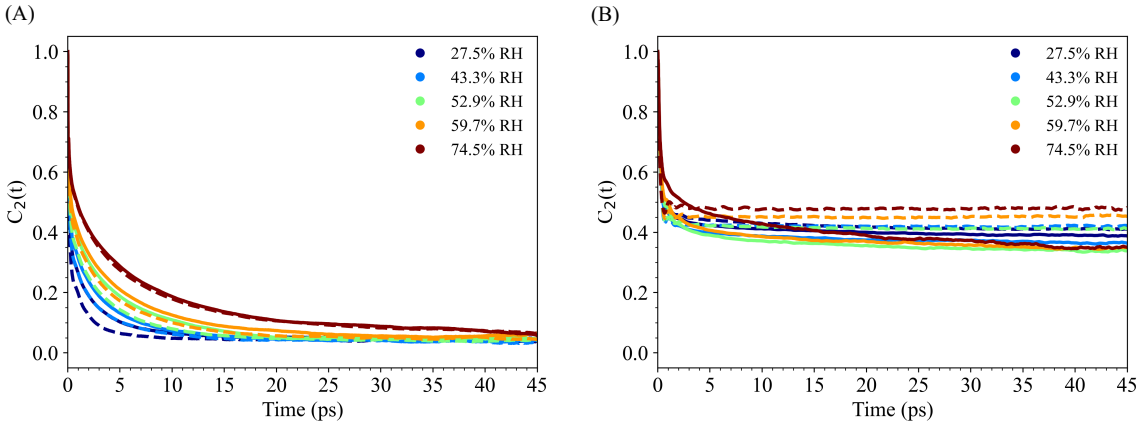

Figure 4.4. Orientational correlation functions of (A) H_2O and (B) CO_2 in the presence (solid line) and absence (dashed line) of the corresponding competing species, i.e., CO_2 in (A) and H_2O in (B), calculated as a function of relative humidity.

Table 4.1. Reorientation time scales (in ps) for H_2O molecules within the CALF-20 framework calculated from Eq.4.5. τ_1, τ_2, and τ_3 correspond to the reorientation time scales associated with the librational motion, hydrogen-bond dynamics, and collective structural rearrangements, respectively. The top and bottom entries for each τ_i ($i = 1,2,3$) correspond to the reorientation times for H_2O molecules in the presence or absence of CO_2 molecules within the framework, respectively, at a given RH value.

	RH				
	27.5%	43.3%	52.9%	59.7%	74.5%
τ_1	0.049 ± 0.001	0.056 ± 0.001	0.073 ± 0.001	0.069 ± 0.001	0.073 ± 0.001
	0.044 ± 0.001	0.055 ± 0.001	0.062 ± 0.001	0.064 ± 0.001	0.070 ± 0.001
τ_2	2.189 ± 0.007	2.902 ± 0.009	4.529 ± 0.014	4.346 ± 0.014	4.745 ± 0.015
	1.431 ± 0.005	2.410 ± 0.009	3.214 ± 0.009	3.693 ± 0.011	4.485 ± 0.013
τ_3	≥ 50	≥ 50	≥ 50	≥ 50	≥ 50

Since the water hydrogen-bond network in CALF-20 becomes more connected and connected as the relative humidity increases (Figure 4.2A), the slower reorientation of the H_2O molecules at high RH values can, therefore, be attributed to increasing water–water interactions. Similar conclusions were drawn in experimental and computational studies of water adsorbed in [Zn(*l*-L)(Cl)],[162] Co_2Cl_2BTDD,[100] and Ni_2Cl_2BTDD.[163] Interestingly, Table 4.1 indicates that the presence of CO_2 molecules within the framework leads to larger τ_2 for the H_2O molecules at each RH value. As discussed above, the presence of CO_2 molecules reduces the available void space and, consequently, limits the ability of the H_2O molecules to reorient. Furthermore, as observed in Figure 4.2A, the presence of CO_2 molecules within the framework promotes the formation of more connected hydrogen-bond networks that further contributes to slowing down the dynamics of the H_2O molecules. Conversely, the presence or absence of CO_2 molecules within the framework does not significantly influence the values of τ_1. This trend can be explained by considering two factors. First, the complexity of hydrogen-bond networks among water molecules varies more significantly across different RH values. Second, the presence of CO_2 molecules within the framework has a comparatively less pronounced influence at each RH value. On the other hand, in the absence of water, the reorientation dynamics of the CO_2 molecules (Figure 4.4B) remain largely independent of the amount of CO_2 present within the framework and exhibit long-time correlations. This behavior can be attributed to weak CO_2–CO_2 interactions that have limited impact on the reorientation dynamics of the CO_2 molecules. Interestingly, relatively stronger framework–CO_2 interactions restrict the motion of the CO_2 molecules in a similar way to that observed for H_2O molecules adsorbed in Co_2Cl_2BTDD.[100] Contrary to the behavior observed for H_2O molecules in the presence of CO_2 within the framework (Figure 4.4A), the presence of water within the framework slightly accelerates the reorientation dynamics of the CO_2 molecules, as indicated by the relatively faster long-time decays of the orientational correlation functions at different RH values in Figure 4.4B. The faster reorientation dynamics of CO_2 in the presence of water can be explained by considering that, due to the competition between CO_2 and H_2O molecules within the framework, not all CO_2 molecules can occupy their

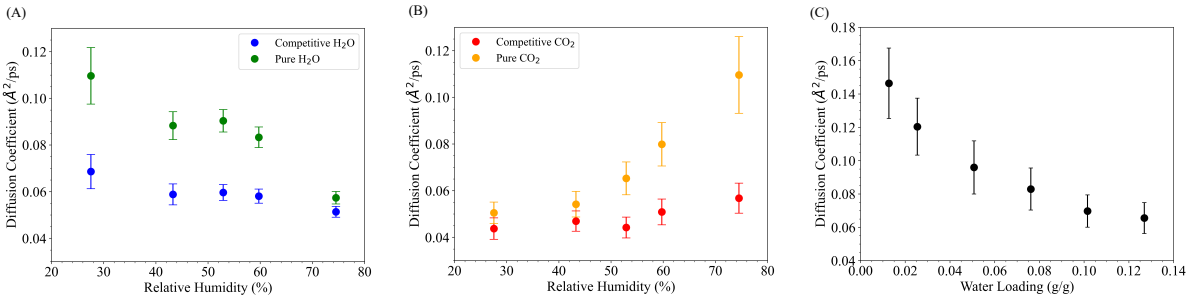

Figure 4.5. Diffusion coefficients calculated from Eq. 1 for H_2O (A) and CO_2 (B) molecules in the presence and absence of the corresponding competing species, i.e., CO_2 in (A) and H_2O in (B), calculated as a function of relative humidity. (C) Diffusion coefficients for a fixed number of CO_2 molecules at different H_2O loadings.

preferential interaction site when H_2O molecules are also present, resulting in less constrained environments for the motion of the CO_2 molecules (see Figure S4 in the Supporting Information). Based on these observations, it can be concluded that the confining environment provided by the CALF-20 framework results in slower reorientation dynamics for both H_2O and CO_2 molecules. Similar conclusions were reached in other studies exploring molecular confinement in diverse materials, including coronene in trimesic acid and 1,3,5-benzenetribenzoic acid self-assembled porous monolayers,[164] as well as the confinement of C_{84} in trimesic acid self-assembled porous monolayer.[165]

The impact of competitive adsorption on the dynamical properties of H_2O and CO_2 molecules within the CALF-20 framework can be further assessed from the analysis of their translational mobility. Figures 4.5A and 4.5B show the variation of the H_2O and CO_2 diffusion coefficients, respectively, calculated as a function of relative humidity. Both H_2O and CO_2 molecules exhibit consistently larger diffusion coefficient in the absence of the competing species across the range between 27.5% and 59.7% RH. It should be noted that although our MD simulations describe systems in equilibrium, the diffusion coefficients calculated for water in the presence of CO_2 within the framework are in qualitative agreement with the water breakthrough experiments of Ref. 123, in which the systems are, however, more akin to steady-state conditions. Importantly, when molecules of the competing species are absent, both H_2O and CO_2 diffusion

coefficients decrease as the total number of molecules present in the system increases. Similar trend was also found in previous computational studies of guest molecules in IRMOF-1 and Mg-MOF-74[127,144]. These findings suggest that the translational mobility of both H_2O and CO_2 molecules is directly impacted by the excluded volume associated with the total number of guest molecules present within the framework. Figure 4.5C shows the variation of the CO_2 diffusion coefficient calculated from MD simulations carried out for systems with the same CO_2 loading as found experimentally at 74.5% RH (Figure 4.1A) and varying H_2O loadings. As the number of H_2O molecules within the framework increases, the CO_2 diffusion coefficient progressively decreases. Given the constant volume exclusion from CO_2, the trend of a decreasing diffusion coefficient for CO_2 can be directly linked to the increasing presence of water within the framework. This observation underscores that the translational mobility of CO_2 within the CALF-20 framework is suppressed by the presence of H_2O molecules.

4.4 Conclusions

We employed data-driven many-body potential energy functions to investigate the competitive adsorption of H_2O and CO_2 within the CALF-20 framework. The competition between H_2O and CO_2 molecules within the CALF-20 framework can be attributed to two factors: 1) comparable interaction strength between H_2O and CO_2 molecules and the framework, and 2) preference of H_2O and CO_2 molecules for occupying similar void spaces within the framework.

The CALF-20 framework exerts confining effects that result in spatial arrangements of the H_2O and CO_2 molecules similar to those found in liquid H_2O and CO_2 at high pressure. Mutual volume exclusion and competing effects for the same binding sites within the framework between H_2O and CO_2 molecules have significant impact on the thermodynamic and dynamical properties of both guest species. The volume exclusion imposed by CO_2 molecules forces the H_2O molecules to occupy smaller void spaces, thereby promoting the formation of more connected hydrogen-bond networks which, in turn, slow down the reorientation dynamics of

the H_2O molecules. The presence of water molecules within the framework leads to faster reorientation dynamics of the CO_2 molecules due to some of the H_2O molecule occupying the same preferential binding sites, which results in less constrained environments for the motion of the CO_2 molecules. The variation of H_2O entropy is more influenced by the presence of CO_2 molecules within the framework, as relatively strong H_2O–H_2O interactions restrict the motion of the H_2O molecules and lower their entropy. In contrast, CO_2 entropy is only sensitive to the presence of water within the framework at high RH values, where most of the void spaces are occupied by water. Both confining effects associated with the CALF-20 framework and mutual volume exclusion effects between H_2O and CO_2 molecules promote the formation of hydrogen-bonds between H_2O and CO_2 molecules and result in more connected hydrogen-bond networks among H_2O molecules. In turn, this makes CO_2 adsorption by CALF-20 energetically more favorable when water is present within the framework. In the absence of their respective competitive molecules, both H_2O and CO_2 molecules exhibit faster translational dynamics as the number of molecules within the framework increases, while the presence of the the corresponding competing species (i.e., CO_2 for H_2O and H_2O for CO_2) further reduces the translational mobility of both species.

Based on the disparity in permanent dipole moments between H_2O and CO_2 molecules, our MD simulations indicate that frameworks with a less polarized charge distribution may exhibit stronger affinity for CO_2 compared to H_2O. Importantly, our analyses indicate that, while on the one hand the presence of water increases the energetic affinity of the CO_2 molecules for CALF-20 without substantially affecting their entropy at low relative humidity values, on the other hand it leads to a decrease in the CO_2 adsorption capacity of CALF-20 due to volume exclusion effects.

4.5 Associated content

The Supporting Information is available free of charge at https://pubs.acs.org/doi/10.1021/acsami.3c11092. Details about the molecular models used in the MD simulations along with the complete list of force field parameters used to describe the CALF-20 framework.

4.6 Acknowledgement

This research was supported by the Department of Energy, Basic Energy Science (BES) Office through award no. DE-SC0022332. All simulations used resources of the National Energy Research Scientific Computing Center (NERSC), supported by Department of Energy BES Office under contract DE-AC02-05CH11231 and the Triton Shared Computing Cluster (TSCC) at the San Diego Supercomputer Center (SDSC).

Chapter 4, in full, is a reprint of the material as it appears in "Elucidating the competitive adsorption of H_2O and CO_2 in CALF-20: New insights for enhanced carbon capture metal-organic frameworks", C.-H. Ho, F. Paesani; Appl. Mater. Interfaces 41, 48287, 2023. The dissertation author was the primary investigator and author of this paper.

Chapter 5

Cooperative Interactions with Water Drive Hysteresis in a Hydrophilic Metal-Organic Framework

5.1 Introduction

The capture and control of water vapor is critical for several applications including desiccation, thermal battery heat storage, heat pump energy transfer, humidity control, desalination, and atmospheric water capture.[51,166] Metal-organic frameworks (MOFs) have been proposed as promising sorbents for the reversible binding of water due to their high porosity, water stability, crystallinity, and chemical tunability. However, the exact relationship between the chemical composition and the behavior of water within pores remains ambiguous. With clear structure-function principles, it will be possible to simultaneously optimize the working capacity, relative humidity for the onset of pore condensation, slope of isotherm, water cycling hysteresis, kinetics of sorption, water cycling stability, and isosteric enthalpy for the adsorption of water. These physical parameters dictate the utility of the sorbent for the desired applications.[51]

Many systematic studies have been performed to elucidate structure-function correlations, with a dominant focus on controlling the onset of pore condensation, increasing working capacity, and increasing water stability.[61,167–169] In order to more easily determine these correlations, there has been interest in developing the chemistry of materials based on bistriazolylar- ene ligands

such as H_2BTDD = bistriazolodibenzodioxin, H_2BBTA = benzenebistriazole, and H_2bibta = bibenzotriazole. This family serves as an ideal model system due to exceptional hydrolytic stability derived from the kinetically inert late transition-metal-triazolate bonds.[170] The effects of isoreticular modification of pore size,[171] modification of the element in open metal sites,[57,172] modification of structural anion identity,[61] and the effect of pore shape[173] have been correlated with changes in the onset of pore condensation and working capacity.[172] Critically, the structure-function correlations determining the presence and size of hysteretic loops have not yet been fully delineated. Even though there is an understanding of the maximum pore size before the onset of capillary condensation-driven hysteresis, the relationship between structure and water supercluster-based hysteresis is still unclear. Herein, we utilize this isoreticular platform to investigate the relationship between the framework structure and adsorption-desorption hysteresis, specifically the relationship between the cooperative binding of water, caused by simultaneous interactions with the nickel site and quinone sites, and the thermodynamics for formation of strong wetting films/water superclusters.

We report a metal-organic framework, Ni_2Cl_2BBTQ (H_2BBTQ = 2H,6H-benzo[1,2-d][4,5-d']bistriazolequinone). This framework adopts a hexagonal topology, isoreticular to the previously described M_2X_2BBTA and M_2X_2BTDD frameworks. Due to the presence of the quinone functional group, the pores are more hydrophilic and bind water tightly. The structure of the hydrogen-bonding network is probed by a combination of variable humidity or variable temperature infrared and Raman spectroscopy, powder X-ray diffraction, and gravimetric analysis with detailed molecular dynamics simulations. We find that the quinone functional groups facilitate the binding of water below 0.5% relative humidity (RH) (at 25 °C) as a result of the cooperative binding of water to the open nickel site, concomitant with hydrogen bonding to the quinone groups. The framework has sluggish activation kinetics below 200 °C under high vacuum due to extreme hysteresis, leading to a reduction of the working capacity during 0-25% RH cycling at 25 °C with 2 h cycles from an ideal ∼0.20 to 0.11 g/g.

5.2 Results and Discussion

5.2.1 Synthetic and Structural Details

Previous syntheses of nonporous MOFs using benzobistriazolequinone ($BBTQ^{2-}$) have utilized the conjugate base under aqueous hydrothermal conditions.[174,175] We hypothesized that conditions mimicking those used in the synthesis of isoreticular Ni_2Cl_2BBTA, which utilize a neutral ligand in an organic solvent, would prevent the formation of metal-ketone coordination bonds and form the desired hexagonal phase (Figure 5.1). Reaction of H_2BBTQ with $NiCl_2$ in acidic N,N-dimethylformamide gives rise to a crystalline, turquoise-colored material with the desired structure type. The crystal structure of the framework was refined against a synchrotron powder X-ray diffraction pattern in space group $R\bar{3}m$ with a = b = 24.65 Å and c = 8.12 Å (Figures S4.1 and 1b). The diameter of the maximally included sphere is 10.7 Å. The oxygen of water bound to the nickel center is crystallographically resolvable, though all other waters in the pores are disordered.

5.2.2 MOF Activation

Due to the narrow and hydrophilic pores that facilitate pore condensation, Ni2Cl2BBTQ is difficult to be activated under dynamic vacuum (3 μmHg) at 135 °C, the activation conditions used for Ni_2Cl_2BBTA, where water desorption is kinetically limited. After 12 h of activation under these conditions, the N_2 isotherm displays type I behavior, with a measured BET surface area of 704 m^2/g and a pore volume of 0.29 cm^3/g. After 36 h of activation, the surface area increases to 1146 m^2/g, with the corresponding pore volume of 0.45 cm^3/g (Figure S6.1).

To improve the rate of activation, higher temperatures are used. Thermogravimetric analysis of Ni_2Cl_2BBTQ (measured under a dry nitrogen flow with 1 °C/min heating) reveals a substantial mass loss between 160 and 200 °C, corresponding to the removal of approximately four water molecules per nickel site (Figure 5.2c). To confirm the stability of the material at these elevated temperatures, we performed variable- temperature powder X-ray diffraction.

Upon heating to 250 °C, we observe the preservation of crystallinity, with an associated small irreversible decrease in the unit cell volume from ∼4200 to ∼4000 Å^3, consistent with the cell contraction upon solvent loss (Figure 5.2a).

Upon activation of the material under dynamic vacuum at 200 °C for 12 h, the material again displays a type I N_2 isotherm, with an increased BET surface area of 1258 m^2/g and a pore volume of 0.50 cm^3/g (Figure 5.2b). This measured surface area lies between the theoretical surface area for a model structure with no waters in the pores, at 1363 m^2/g, and a model structure with one water bound to each nickel site, at 1,218 m^2/g, suggesting that even heating at 200 ° for 12 h does not result in complete activation of the framework.

Upon activation of the framework at 200 °C, an irreversible chemical change occurs, char-

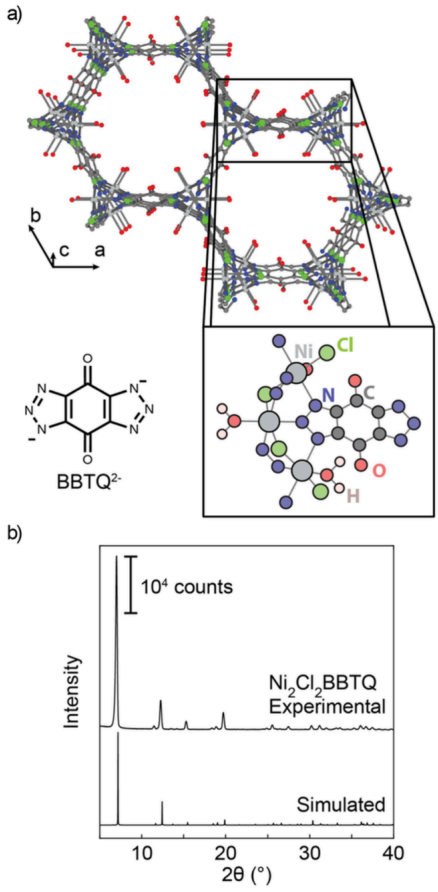

Figure 5.1. (a) Portion of the structure of Ni_2Cl_2BBTQ (with the central pore guest water molecules excluded). (b) Powder X-ray diffractogram of Ni_2Cl_2BBTQ (Cu K_α radiation).

acterized by a darkening in color, proceeding from green to purple to black. Variable-temperature ultraviolet-visible-near-infrared spectroscopy (under a flow of helium gas) reveals the appearance of two new absorption bands at 14,877 and 22,857 cm^{-1} (672 and 438 nm) upon heating, with the onset temperature below 80 ° (Figure 5.2d). We attribute these changes to the reduction of quinone to hydroquinone via water oxidation, where there is an equilibrium between quinone and hydroquinone with quinhydrone (i.e., quinone-hydroquinone dimer). These bands correspond to the quinhydrone charge-transfer excitation and hydroquinone π-π* excitation, respectively.[176] It is difficult to quantify precisely the ratio of quinone to hydroquinone as the equilibrium constant between quinone-hydroquinone and quinhydrone is not known, and ^{13}C-ssNMR spectra do not exhibit any features (likely due to paramagnetic broadening by spin polarization from the nickel sites). However, given that the quinhydrone band grows monotonically with temperature, we expect that the quinone content outnumbers hydroquinone (ideally at an equal quinone-hydroquinone content, the quinhydrone band would reach a maximum and decrease in intensity after hydroquinone exceeds quinone content).

The carbon 1s region of X-ray photoelectron spectra corroborate the assignment for partial reduction of quinone to hydroquinone. A spectrum of pristine material displays a small band at 288 eV and a larger band at 286 eV, corresponding to the C=O and C-N carbons, respectively (Figure S7.1). Upon activation, the relative intensity of the 288 eV band to the 286 eV band decreases, consistent with the reduction of quinone, as an aromatic alcohol also appears at around 286 eV. Additionally, the spectrum of the material that was cycled through many water isotherms and activated several times displays a weaker π-π* satellite band at 291 eV compared with the pristine Ni_2Cl_2BBTQ, consistent with the increasing amount of hydroquinone.

There is a slight decrease in the ratio of chloride/nickel from 1.0 to 0.77, as measured by X-ray photoelectron spectroscopy, which occurs only during the initial activation of the framework (Figures S7.3 and S7.4). The slight loss of chloride is attributed to the exchange of chloride to hydroxide, concomitant with the formation of hydrochloric acid, since there is no evidence of the reduction of nickel by X-ray photoelectron spectroscopy. Given that X-ray

photoelectron spectroscopy is a surface technique, this reactivity pattern may be considered as surface passivation that occurs during the first activation.

5.2.3 Water Sorption

The water isotherms of Ni_2Cl_2BBTQ display type I behavior, consistent with the water isotherm of a microporous framework (Figure 5.3a).[177] The maximum capacity of the framework after activation at 200 °C is 0.38 g/g (approximately four water molecules per nickel site). At 9.6% RH, the quantity of water adsorbed is 0.22 g/g, indicating that Ni_2Cl_2BBTQ adsorbs most of its maximal water uptake at extremely low relative humidity. The onset for pore condensation is consistent with other smaller pore frameworks, such as the isoreticular Ni_2Cl_2BBTA. There is a slight positive slope at a higher relative humidity, which we attribute to water condensation on the exterior of and in between crystallites.[178]

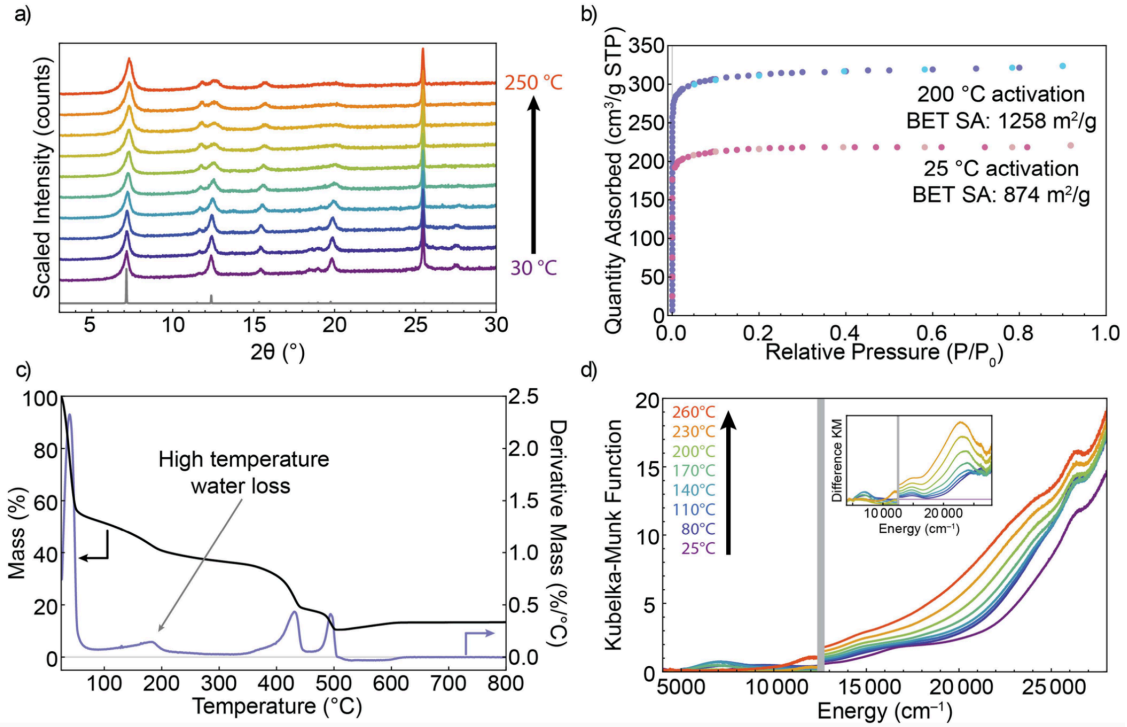

Figure 5.2. (a) Variable-temperature powder X-ray diffractogram (Cu K_α radiation). The gray trace is a simulated pattern. The reflection at 25.5° corresponds to the Al_2O_3 sample holder. (b) N_2 isotherms of Ni_2Cl_2BBTQ activated at 25 and 200 °C. (c) Thermogravimetric analysis for Ni_2Cl_2BBTQ. (d) Variable-temperature UV-vis-NIR spectra of Ni_2Cl_2BBTQ.

The high temperatures and extended activation times required to maximize the N_2 surface area are consistent with the expectation of a large hysteresis in the water isotherm. Kinetically hindered desorption may be caused by a large barrier for dissociating water due to the strong hydrogen- bonding network (this can be considered as a water supercluster or as thick pore wetting occurring prior to capillary condensation).[59,179] Indeed, upon desorption to 25 °C and 1.0% RH, there is still 0.16 g/g of adsorbed. This contrasts with the water isotherms for Ni_2Cl_2BBTA, which displays minimal hysteresis despite adsorbing water at lower RH.[171] The nature of the hysteresis with Ni_2Cl_2BBTQ differs from traditional ones, such as capillary condensation that occurs in frameworks with pores larger than 20 Å, or hysteresis caused by flexible pores that undergo expansion and contraction.[166]

Variable-temperature isotherms measured at 15, 25, and 35 °C were analyzed in order to measure the isosteric enthalpy of adsorption for water (Figure 5.3b). For this measurement, the sample was reactivated at 70 °C under dynamic vacuum (70 °C being chosen over 200 °C in order to prevent the possibility of slight framework degradation from affecting the calculation). The three isotherms display a similar uptake. The isosteric enthalpy of adsorption was calculated using linear interpolation, as none of the typical sorption models fit well to the data. It was not interpolated below 6 mmol/g due to insufficient data at very low RH. The isosteric enthalpy of adsorption was calculated to be roughly between 40 and 60 kJ/ mol, consistent with the isosteric enthalpy of adsorption of water in similar microporous MOFs. This value is higher than the enthalpy of vaporization for pure water at 40.7 kJ/mol, consistent with strong binding in the pore under confinement.[180] Given that this measurement was performed with activations at low temperature, it is difficult to experimentally bound the isosteric enthalpy of adsorption for the monolayer of water.

To test the stability of the framework for use as an adsorbent, cycling experiments were performed. In particular, the framework was cycled between 0 and 25.2% RH at 25 °C with 30 min for adsorption and 90 min for desorption. Whereas the kinetics of adsorption are fast ($<$5 min), the desorption process is slow: complete desaturation does not occur even after 1 h at

0% RH. The working capacity for 2 h adsorption-desorption cycles decreases by 11% over 52 cycles, with a mean working capacity of 0.11 g/g (Figures 5.3c,d and S8.1). We attribute the slight decrease to a combination of reduction of the quinone to hydroquinone during desorption, the small amount of chloride to hydroxide exchange, and any potential framework collapse that may occur as a result of the large internal forces the material undergoes during cycling. Importantly, the hysteresis is not responsible for the loss in working capacity: the isoreticular and nonhysteretic Ni_2Cl_2BBTA loses 8% of its capacity during temperature swing cycling, although the mechanism of capacity loss need not be the same.[171]

The cause of the sluggish desorption kinetics differs from that for typical materials, whose kinetics are limited by external diffusion. For a typical nonhysteretic sorbent during cycling, the rate of sorption is most significantly modified by the shape of the isotherm (which dictates the RH gradient between the sorbent bed and atmosphere), rather than by the intrinsic rate constant.[181] However, for Ni_2Cl_2BBTQ, the intrinsic rate of desorption is quite slow (even on the time scales for isothermal measurements), and we expect that the cycling is internally kinetics/diffusion limited. Certainly, this is not ideal for a practical sorbent, and identifying the physical property that causes such slow desorption is necessary such that it can be avoided for other sorbents.

5.2.4 Thermodynamics of Water Adsorption by Molecular Dynamics Simulation

To further probe the interaction between the framework and water at the lowest coverage, detailed molecular dynamics (MD) simulations were performed using the MB-pol many-body potential (details in Supplemental Section 1).[34–36] As the water loading increases from 0.056 to 3.0 mol H_2O/mol Ni, the adsorption enthalpy increases sharply from -15.3 to approximately -13.3 kcal/mol (-64 to -56 kJ/mol), and subsequently remains relatively constant (Figure 5.4a). This sharp increase in the adsorption enthalpy corresponds to the pore condensation step below 5% RH.

At the lowest loading (only one water molecule loaded within the framework), the most probable distance between the open nickel site and the oxygen atom in water is approximately 2.0 Å, as illustrated in the radial distribution function (RDF, Figure S10.1). This observation suggests that the nickel sites predominantly serve as the primary sites for the initial hydration and water capture. However, rigid coordinate scans indicate that the interaction energy between water and the open nickel site is only -8 kcal/mol, significantly smaller than the zero-coverage adsorption enthalpy of -15.3 kcal/mol (Figure S9.3). This suggests that the interaction energy between water and quinone also exerts a significant influence on adsorption. This secondary interaction is further indicated by the RDF between the quinone oxygen and water hydrogen, with a most probable distance of approximately 1.9 Å (Figure S10.1). This pair of key interactions that leads to strong water uptake at the monolayer level is illustrated in Figure 5.4c.

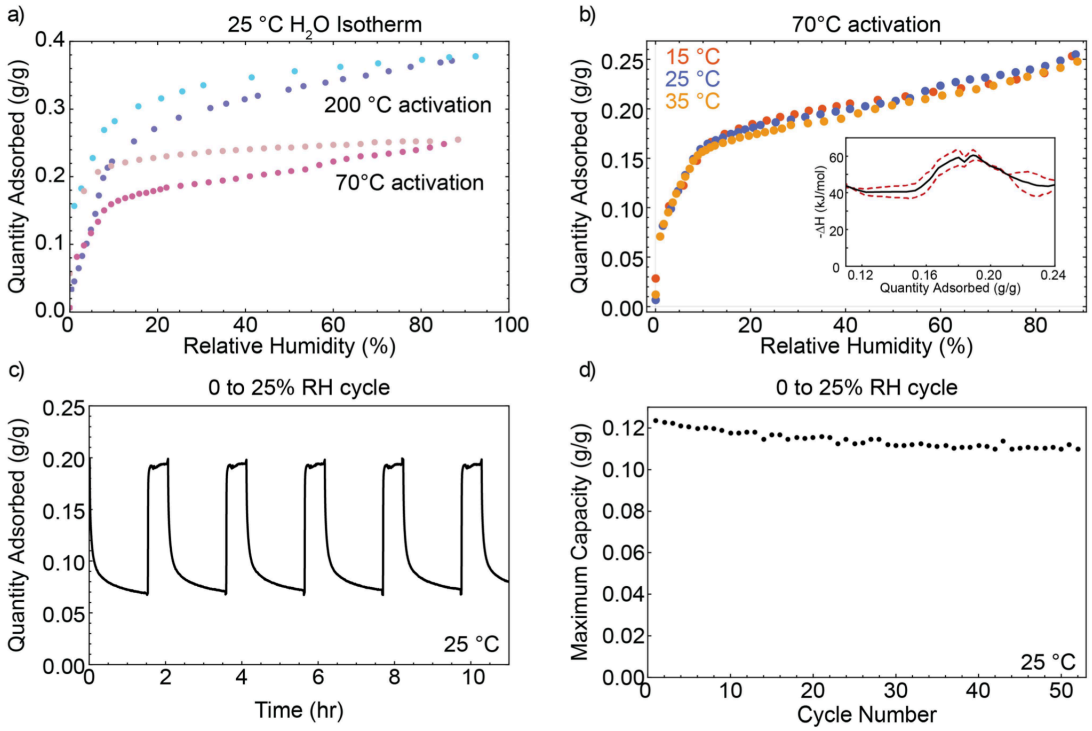

Figure 5.3. (a) Water isotherm of Ni_2Cl_2BBTQ with activation at 200 and 70 °C. (b) Variable-temperature water isotherm of Ni_2Cl_2BBTQ and the isosteric enthalpy of adsorption (dashed lines denote standard error). (c) Cycling at 25 °C between 0 and 8 mbar. (d) Working capacity during cycling over 52 cycles.

The entropy of water exhibits a trend similar to the adsorption enthalpy as a function of the water loading (Figure 5.4b). It displays a rapid increase from 14.8 to 17.6 cal/mol K as the loading increases from 0.056 to 1.2 mol of H_2O/mol of Ni, followed by a gradual decrease to 17.0 cal/mol K when the loading is further increased to 3.0 mol of H_2O/mol of Ni, which is attributed to the increasing complexity of the hydrogen-bond network. Remarkably, this behavior diverges from that observed for NU-1500-Cr (a framework previously studied by the same methods), in which the entropy rapidly decreases during capillary condensation.[146] This difference can be ascribed to the characteristics of the primary interaction sites during the initial hydration phase, resulting in distinct dynamic properties of water molecules, which will be further elaborated in the subsequent section.

While the entropy trend of water in Ni_2Cl_2BBTQ differs from that in NU-1500-Cr, both cases exhibit notable variations in adsorption enthalpy and entropy around the adsorption step on the isotherm, which correspond to filling the regions with the largest void space within the two frameworks. This observation offers a characteristic feature that can be employed in MD simulations to determine the relative humidity value corresponding to the adsorption step and characterize the pore filling mechanism within a given framework structure.

5.2.5 Dynamical Properties of Water Adsorption

To shed light on the difference in the water entropy at the early stage of hydration, several dynamical properties of water at different loadings were calculated by using MD simulations. The spatial distribution of water within the pores were calculated as a function of water loading (Figure 5.5a, defining nickel site occupation within 2.5 Å and quinone site occupation within 2.2 Å). Strong correlations between nickel and quinone site occupation suggest that water binding to open nickel sites is always accompanied by hydrogen bonding to the quinone oxygen, which notably contributes to the adsorption enthalpy at the early stage of hydration, as shown in Figure 5.4a. The confinement effects of Ni_2Cl_2BBTQ are further elucidated by comparing the orientational correlation function of a single water molecule within Ni_2Cl_2BBTQ with that of the

previously studied and larger-pore NU-1500-Cr (Figure 5.5b). We find that the reorientation rate of water in Ni_2Cl_2BBTQ is slower than that in NU-1500-Cr. This suggests that Ni_2Cl_2BBTQ imposes stronger constraints on the motion of a water molecule than does the chromium MOF, as the water molecule binds to the respective primary interaction sites in the initial hydration stage. With Ni_2Cl_2BBTQ, a water molecule binds to a single Ni site, and its rotation is constrained by hydrogen bonding to the nearby quinone. In contrast, for NU-1500-Cr, the first water molecules bind exclusively to Cr sites during the initial hydration stage and are overall less constrained than those in Ni_2Cl_2BBTQ. As a result, the different entropic behavior of water at low loadings between the two MOFs: increasing with RH for Ni_2Cl_2BBTQ, and decreasing for NU-1500-Cr, directly correlates with the constraint imposed on water molecules particularly by the neighboring quinone sites in the former.

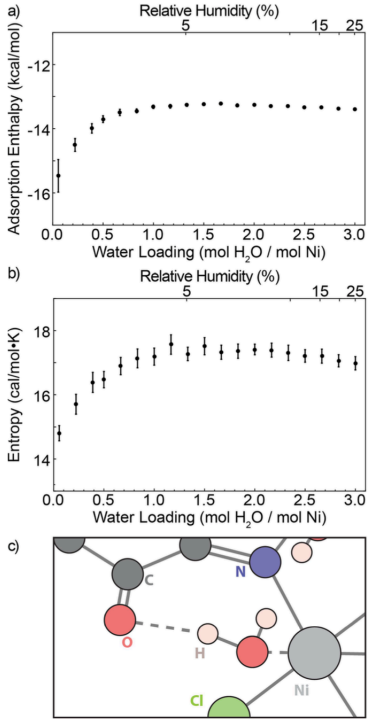

Figure 5.4. Thermodynamic properties of water within Ni_2Cl_2BBTQ at different loadings. (a) The adsorption enthalpy and (b) water entropy. (c) A representative structure from molecular dynamics simulations in which a water molecule is simultaneously bound to the nickel site and hydrogen bonds to the quinone site.

Analysis of the statistics of water molecules located near the center of the pore in Ni_2Cl_2BBTQ provides further insight into the confinement effects (Figure 5.5a). Notably, only $\sim$50% of the nickel sites are saturated with water upon loading of 1 mol H_2O/mol Ni. Even at the highest loading considered here, 3 H_2O/mol Ni, approximately 8% of the nickel sites remain unsaturated. At this highest loading, the remainder of the water that could be occupying the unsaturated nickel sites instead lies within the center of the pore. The water occupation at the central pore positions exhibits a seemingly linear growth with increasing water loading. As the pore water occupation increases, the hydrogen-bonding network becomes more connected (Figure 5.5c) with a distribution of water having multiple donor (D) or acceptor (A) partners. Consequently, as the water loading increases, the energy difference between saturating a nickel site and participating in the hydrogen- bonding network gradually diminishes. This suggests that entropic effects gradually become the main factor determining the percentage of Ni sites being saturated at a high water loading.

The confinement effects of Ni_2Cl_2BBTQ on water molecules are further reflected in the translational transport properties. The diffusion coefficient of water molecules along the pore direction (crystallographic c-direction) increases with the water loading (Figure 5.5d). This is consistent with a large population of water immobilized by nickel and quinone sites at low water loading, resulting in pronounced hindrance to water translational mobility. At higher water loading, there is a corresponding rise in the percentage of water molecules situated near the center of the pore, which reduces the constraints on translational mobility. A similar trend in diffusion coefficients at varying water loadings has been observed in other systems, such as Zn(*l*-L)Cl[162] and Co-MOF-74,[148] and has been suggested in the investigation of water in isoreticular Co_2Cl_2BTDD.[100] The analogous trend in diffusion coefficients observed in these MOFs can be attributed to their similarity in strong interactions with the framework at low water loadings, where most water molecules either saturate the metal sites or establish hydrogen bonds with the framework.

5.2.6 Vibrational Spectroscopic Characterization

Vibrational spectroscopy supports the structural assignments of confined water from MD simulations. Specifically, the symmetric and antisymmetric ν(C=O) quinoidal vibrational modes were used as spectroscopic handles to probe the water-MOF interaction. The shifts in these vibrational bands upon coordination to water directly report the spatial distribution of water as a function of RH. In situ infrared (IR) spectroscopy was performed under a controlled RH between 0.2 and 26% in both diffuse reflectance infrared Fourier transform spectroscopy (DRIFTS) and transmission geometries.

Upon heating the sample to 150 °C under a dry argon stream, sharp vibrational bands are displayed from 2400 to 3600 cm^{-1}, consistent with a hydrogen-bonding network of pore-

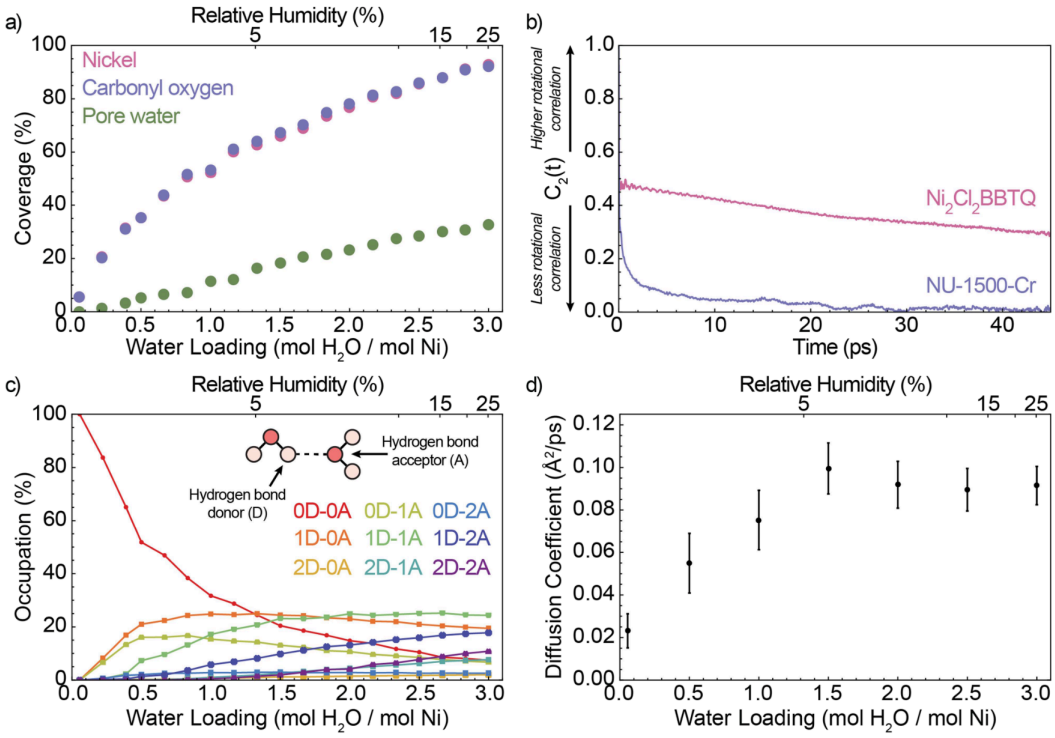

Figure 5.5. Dynamical properties of water within Ni_2Cl_2BBTQ. (a) Percentage of occupancy of Ni, carbonyl oxygen, and the center of the pore at different water loadings. (b) Orientational correlation function of a single water molecule confined in Ni_2Cl_2BBTQ (red). For comparison, the corresponding orientational correlation function confined in NU-1500-Cr (blue) calculated from ref 146 is shown. (c) Hydrogen-bond topologies of water and (d) diffusion coefficients of water along the pore direction at different loadings.

confined water. Upon activation at 220 °C, the bands at approximately 1610 and 1650 cm^{-1} disappear, while the band at 1700 cm^{-1} sharpens (Figure 5.6a). The intensity of the water bands also decreases, consistent with a more complete activation of the framework. Upon dosing the material to approximately 5% RH, the water bands and the bands at 1610 and 1650 cm^{-1} reappear (Figure S11.1). Above 5% RH, no further changes occur, indicating that the material was fully saturated with water. Upon reactivation of the material at 150 °C, the water bands around 3000 cm^{-1} as well as the 1610 and 1650 cm^{-1} bands decrease in intensity, indicating reversibility.

To determine the changes in the hydrogen-bonding network below 5% RH, we performed in situ IR spectroscopy in a transmission cell designed such that incremental quantities of water vapor could be dosed at known pressures. Upon activation of the framework at 240 °C, we observe a decrease in intensity of the bands between 1620 and 1660 cm^{-1}, as well as the conversion of a band from 1684 to 1716 cm^{-1}, with an isosbestic point near 1700 cm^{-1} (Figure S11.2). After activation, a few sharp bands in the water region remain, ranging from 2947 to 3558 cm^{-1}, consistent with the well-defined hydrogen-bond network of residual water in the pores, partial reduction of the quinone to hydroquinone, and/or a small amount of chloride-to-hydroxide anion exchange.

Two distinct features appear upon dosing with water up to 5% RH. First, a very broad band spanning from 3700 to approximately 2500 cm^{-1} increases in intensity. This band is associated with the ν(O-H) water vibrational modes. The broad features are diagnostic of a hydrogen-bond network that is not ordered. Second, there is a decrease in intensity for the band at 1716 cm^{-1} and an increase in intensity for both bands at 1684 and 1653 cm^{-1} (Figure 5.6b-d). The band at 1716 cm^{-1} is attributed to νasym(C=O), the frequency of the B_{1u} quinone stretching mode. In order to assign the 1684 and 1653 cm^{-1} bands, we repeated the experiment while dosing with D_2O. Isotopic labeling reduces the relative intensity of the 1653 cm^{-1} band (Figure S11.5), suggesting that it corresponds to the water bending mode, while the 1684 cm^{-1} corresponds to the νasym(C=O, H-bond) mode (the corresponding quinone stretching mode

with hydrogen bonding to water). The assignment of ν_{asym}(C=O) and ν_{asym}(C=O, H-bond) to the 1716 and 1684 cm^{-1} bands is in agreement with the observed isosbestic point, which indicates an interconversion between the two species.

Given these spectral assignments, structural information as a function of the RH may be extracted. Integration of the difference spectra for a particular vibrational band as a function of RH reveals changes in the distribution of molecules in the system. Comparisons of the difference spectra for the regions comprising the O-H (integrated from 2975 to 4000 cm^{-1}) and the asymmetric C=O stretching mode (intensity determined by Gaussian deconvolution, Figure S11.3) reveal the RH values where water coordinates and then saturates the quinone groups (Figure 5.7a). The integrated difference spectra before reaching 1.5% RH, in agreement with the predictions from MD simulations.

To probe the local structure of water around the quinones, we measured the depolarization ratios of the quinone symmetric vibrations using Raman spectroscopy (excitation wavelength of 785 nm) for the unactivated and activated Ni_2Cl_2BBTQ. The Raman spectrum of the unactivated framework displays bands at 1692 and 1712 cm^{-1}, whereas the spectrum of the activated framework displays bands at 1701 and 1723 cm^{-1}. The bands at 1712 and 1701 cm^{-1} in the unactivated and activated spectra are likely overtones, as they lie at approximately 2 times the energy of other observed bands, 855 and 852 cm^{-1}, respectively (with slight deviations likely due to anharmonicity). We can, therefore, attribute the band at 1723 cm^{-1} to the symmetric quinone vibrational mode ν_{sym}(C=O) and the band at 1692 cm^{-1} to the symmetric quinone vibrational mode where the quinone is hydrogen- bonding to water, ν_{sym}(C=O, H_2O) (Table 5.1).

Given these assignments, we measured the depolarization ratio, ρ, whose value is a measure of the symmetry for a vibrational mode, to gain insights into the local structure of the second water layer (Figures 5.7b, S12.1, and S12.2). For BBTQ, a molecule with local D_{2h} symmetry, the depolarization ratio for an A_g symmetric vibrational mode should be between 0 and 0.75, while the ratio for a vibrational mode with any other symmetry will be 0.75.[182,183] We find that the symmetric ν_{sym}(C=O) band at 1723 cm^{-1} is a polarized band with $\rho = 0.60$, which is

consistent with a totally symmetric vibrational mode. However, the symmetric ν_{sym}(C=O, H_2O) band at 1692 cm^{-1} is a depolarized band with ρ = 0.74, inconsistent with a totally symmetric vibrational mode. We attribute the depolarization to a breaking of symmetry at the quinone away from ideal D_{2h} symmetry due to strong coupling between the quinone vibrational mode and the water vibrational modes.

The assignments of quinone vibrational modes are consistent with the theoretical calculations. The nonscaled DFT-calculated vibrational modes of $BBTQ^{2-}$ and $2H_2O{\cdot}BBTQ^{2-}$ are ν_{sym}(C=O) = 1688 cm^{-1}, ν_{asym}(C=O) = 1684 cm^{-1}, ν_{sym}(C=O, H_2O) = 1681 cm^{-1}, and ν_{asym}(C=O, H_2O) = 1672 cm^{-1} antisymmetric. Experimentally and computationally, the symmetric vibrational mode is 5-10 cm^{-1} higher in energy than the antisymmetric vibrational mode, and there is a red shift upon coordination to water, measured 32 cm^{-1} experimentally and calculated at 10 cm^{-1} by using DFT.

5.3 Conclusion

In summary, isoreticular modification of Ni_2Cl_2BBTA to the quinoidal Ni_2Cl_2BBTQ greatly increases the interaction strength of the framework with water, causing monolayer wetting and formation of superclusters, pore condensation at extremely low relative humidity, and strong adsorption- desorption hysteretic behavior. In particular, the strong interaction strength is due to the cooperative interaction between water binding at the unsaturated nickel site and concomitant binding at the quinone sites, allowing for the formation of a hydrogen-bond network at low RH. Application of this principle of multiple neighboring adsorption sites to larger pore frameworks

Table 5.1. Assignment of the Quinone Vibrational Modes.

ν(C=O)	antisymmetric, B_{1u}	symmetric, A_{1g} (depolarization ratio)
activated	1716 cm^{-1}	1716 cm^{-1} (0.60)
bound to water	1684 cm^{-1}	1692 cm^{-1} (0.74)

may enable the design of frameworks with a high capacity and very low relative humidity onset for pore condensation, which may be useful in certain scenarios. Moreover, by designing sorbents that avoid multiple neighboring adsorption sites and instead achieve low RH adsorption through small pore sizes, hysteresis caused by strong wetting may be avoided.

5.4 Associated Content

The Supporting Information is available free of charge at https://pubs.acs.org/doi/10.1021/acs.chemmater.4c00172. General information, synthetic methods, nuclear magnetic resonance spectroscopy, powder X-ray diffractometry, scanning electron microscopy, N_2 isotherms, X-ray photoelectron spectroscopy, water isotherms and cycling, force field parameters, radial distribution function of water, infrared spectroscopy, and Raman spectroscopy (PDF) Crystallographic

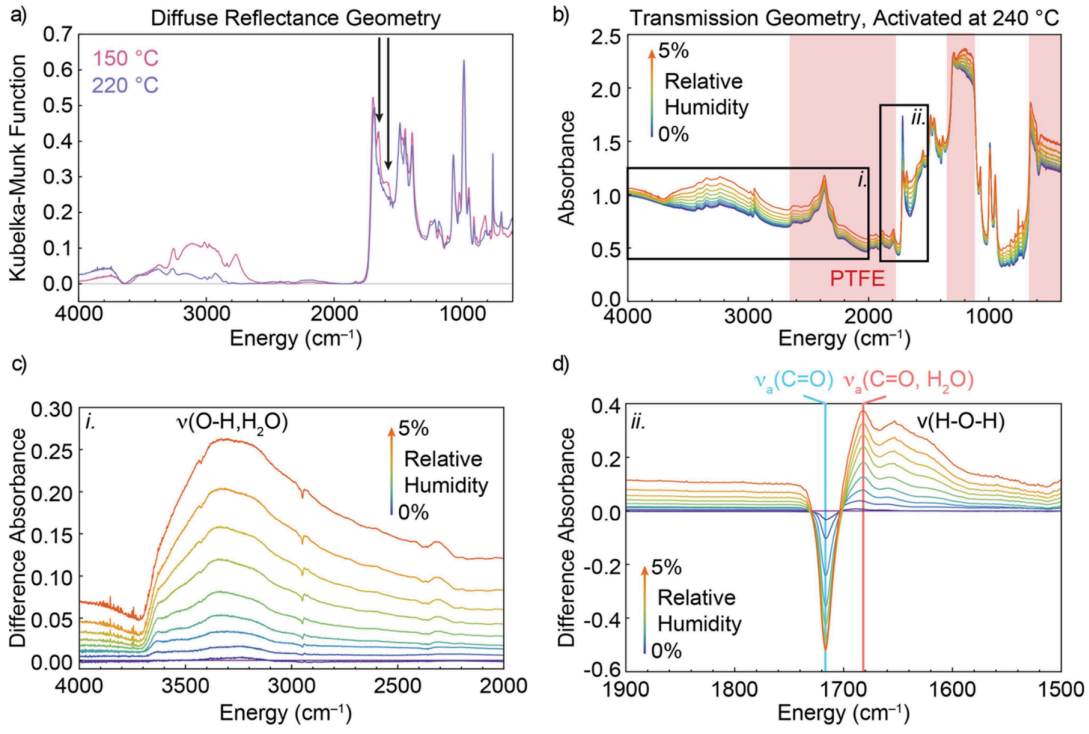

Figure 5.6. (a) DRIFT spectra of Ni_2Cl_2BBTQ upon activation at 150 and 220 °C. (b) Absorbance spectra upon dosing from 0 to 5% RH. Red areas highlight the vibrational modes of polytetrafluoroethylene. (c) Difference absorbance spectra of the water region. (d) Difference absorbance spectra of the quinone region.

data of Ni_2Cl_2BBTQ (cif)

5.5 Author Contributions

J.J.O.: investigation, methodology, visualization, and writing; C.-H.H.: investigation and writing; J.A.: investigation (supporting synthesis); D.A.: investigation (adsorption studies); T.C.: investigation (XPS); B.D.: investigation (infrared); F.P.: funding acquisition, supervision (theoretical and computational), and reviewing editing; and M.D.: funding acquisition, supervision, reviewing, and editing. All the authors discussed the results and commented on the manuscript. All authors have given approval to the final version of the manuscript. J.J.O. and C.-H.H. contributed equally to this work.

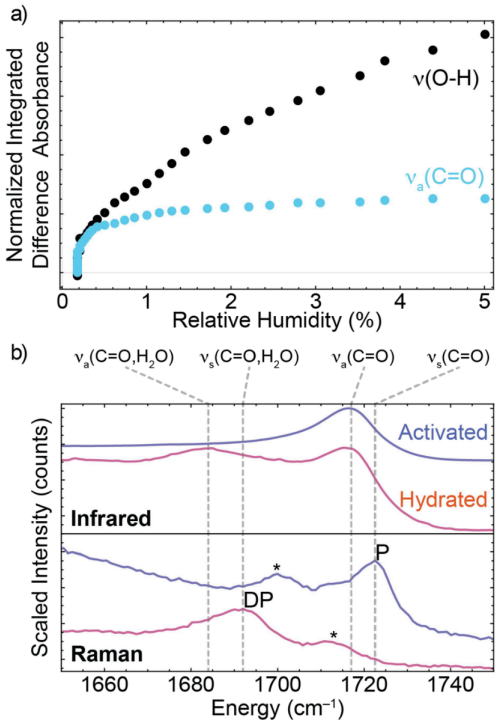

Figure 5.7. (a) Normalized integrated difference absorbance for the water ν(O-H) band and ν_{asym}(C=O) band. (b) Comparison of the IR and Raman spectra of activated and hydrated Ni2Cl2BBTQ. *Indicates an overtone, DP indicates a depolarized band, and P indicates a polarized band.

5.6 Funding

Work by the Dincă group was funded by the Brown Family Foundation. The computational component of this research was supported by the National Science Foundation through award no. 2311260. All simulations were carried out on Expanse at the San Diego Supercomputer Center (SDSC) through allocation CHE230052 from the Advanced Cyberinfrastructure Coordination Ecosystem: Services & Support (ACCESS) program, which is supported by NSF grants nos. 2138259, 2138286, 2138307, 2137603, and 2138296, as well as Triton Shared Computing Cluster (TSCC) at SDSC.

5.7 Acknowledgement

We would like to thank Dr. Gang Liu for assistance in repairing instrumentation.

Chapter 5, in full, is a reprint of the material as it appears in "Cooperative Interactions with Water Drive Hysteresis in a Hydrophilic Metal-Organic Framework", J. J. Oppenheim, C.-H. Ho, D. Alezi, J. Andrews, T. Chen, B. Dinakar, F. Paesani, M. Dincă; Chem. Mater. 2024, 36, 3395. The dissertation author was the primary investigator and author of this paper.

Chapter 6

Exploring Bulk Water Structure and Entropy Predicted by Two-Phase Thermodynamic Model

6.1 Introduction

Entropy plays a crucial role in physical science. The second law of thermodynamics states that the total entropy of the universe cannot decrease. Moreover, entropy has been shown to be associated with the spontaneity of physical or chemical reactions.[184,185] Understanding entropy changes for such processes, particularly in vivo, could be vital for designing medical treatments for diseases.[186–189] Therefore, the ability to calculate entropy changes for given reactions is critical. Given that 70% of the human body is composed of water, calculating the entropy of bulk water serves as the first step toward generalizing entropy calculations for reactions that occur in aqueous solutions.

Although the closed-form definition of entropy was proposed by Boltzmann around a century ago, only a very limited number of systems have closed mathematical expressions, and therefore acquiring the absolute entropy value remains challenging for most of the systems. However, the two-phase thermodynamic model (2PT) offers a simple method to estimate the entropy of a liquid by decomposing the total density of states into solid-like and gas-like components.[93,190,191] It approximates the solid-like component to describe a solid, whose normal

modes are harmonic, while the gas-like component is considered as a hard-sphere gas. Since the diffusion of the liquid can be fully attributed to the gas-like component, the decomposition of the total density of states can be uniquely determined. Consequently, the total entropy can approximately be obtained by summing the entropy contributions from each component.

Given that the density of states is associated with the molecular model employed in molecular dynamics simulations, comparing the entropy value calculated with a given model to the experimental value provides useful insights into the reliability of the model itself. Among all existing water models, MB-pol is a water model developed based on the many-body formalism with reference energies calculated at the coupled-cluster single, double, and perturbative triple excitation level of theory, *i.e.*, CCSD(T).[34–36] MB-pol has demonstrated excellent agreement with experiments in both gas and condensed phases[86,87,104,147], as well as within porous materials.[95,100,102,146,192–194] The recent development of MB-pol(2023) additionally demonstrates its sub-chemical accuracy in modeling the energetics of water hexamer isomers by incorporating a larger 2-body and 3-body training set, as well as explicit machine-learned 4-body energies.[195] As a result, MB-pol and MB-pol(2023) serve as meaningful references to assess the entropy value predicted by the 2PT model. On the other hand, simulating systems containing a large number of water molecules is only feasible when using less complicated water models, due to the complexity of the many-body formalism and the constraints dictated by current computational resources. Therefore, assessing and analyzing the entropy values and water structure of different models serve as an important guide for realistic simulations.

In this study, we analyze the structure of bulk water predicted by MB-pol, MB-pol(2023), and several common water models, and examine their relations with the entropy values predicted by the 2PT model using molecular dynamics simulations. As these water models have been widely used to simulate various aqueous systems, such as salts dissolved in water, biomolecules in water, and water penetrating through membranes,[196–203] our analyses on the relationship between water structure and entropy serve as an important step for realistic simulations in aqueous environments.

6.2 Methods

Water models belonging to the SPC family (SPC[67], SPC/E[66], SPC/Fw[204]), TIPnP family (TIP3P[63], TIP4P[63], TIP4P/2005[155], TIP4P/2005f[205], TIP4P/Ew[65], TIP5P[64]), MB-pol[34–36], and MB-pol(2023)[195] were investigated using classical molecular dynamics (MD) simulations. All simulations for the SPC family and TIPnP family were performed using the Large-scale Atomic/Molecular Massively Parallel Simulator (LAMMPS)[113]. Simulations for MB-pol and MB-pol(2023) were carried out by LAMMPS interfaced with the MBX C++ library.[112]

For each water model, the initial configuration comprised 256 water molecules enclosed within a cubic periodic simulation box using Packmol[91,92], with its volume set to align with the experimental density of water at 1 atm and 298 K. The equations of motion were propagated using the velocity-Verlet algorithm with a time step of 0.2 fs in the canonical ensemble (constant number of atoms, volume, and temperature, NVT).[206] The simulation temperatures were controlled using a global Nosé-Hoover chain consisting of four thermostats.[89] Nonbonded interactions were truncated at an atom-atom distance of 9.0 Å. The long-range electrostatic interactions for the SPC TIPnP families of models were calculated using the particle-particle particle-mesh solver as implemented in LAMMPS. The long-range electrostatic interactions for MB-pol and MB-pol(2023) were calculated using the particle mesh Ewald method as implemented in MBX.[112,158,159] The entropy of each water model was averaged by 20 independent 50 ps long trajectories in the NVT (constant number of molecules, volume, and temperature) ensemble using the 2PT model.[93] The tetrahedral order parameter, q_{tet}, was calculated according to[105]

$$q_{tet} = 1 - \frac{3}{8} \sum_{j=1}^{3} \sum_{k=j+1}^{4} \left(\cos \psi_{ijk} + \frac{1}{3} \right)^2, \tag{6.1}$$

where ψ_{ijk} is the angle between the oxygen atom of the central water molecule with index i and two neighboring oxygen atoms with index j and k within a distance of 3.5 Åfrom the central molecule. $q_{tet} = 0$ corresponds to a completely disordered arrangement as in an ideal gas, while

$q_{tet} = 1$ corresponds to a perfect tetrahedral arrangement. The orientational correlation functions were calculated by averaging over the trajectories according to[161]

$$C_2(t) = \langle P_2[\vec{e}(0) \cdot \vec{e}(t)] \rangle. \tag{6.2}$$

Here, $\vec{e}$ represents a unit vector along one of the OH bonds of a water molecule, P_2 is the second-order Legendre polynomial, and $\langle ... \rangle$ refers to the ensemble average over all OH bonds at a specific time t.

6.3 Results and Discussions

The entropy values calculated with all water models considered in this study are listed in Table 6.1 along with the experimental value. The entropy values obtained for SPC, SPC/E, SPC/Fw, TIP3P, TIP4P/2005, and TIP4P/Ew agree with those reported in previous studies.[93,191] Within the SPC and TIPnP families, SPC and TIP3P display the closest agreement with the experimental value, respectively. All other water models, on the other hand, exhibit similar entropy values that are consistently smaller than the experimental value. Despite water models belonging to the SPC family and TIPnP families being empirical and described by effective two-body potential energy terms, TIP4P and TIP5P exhibit slightly closer agreement with the experimental value than MB-pol and MB-pol(2023), which were developed based on a rigorous many-body formalism and CCSD(T) reference energies. To explore the potential influence of nuclear quantum effects on the entropy value, we also calculated the entropy value of MB-pol in the microcanonical ensemble using centroid molecular dynamics (CMD), an approximate method to represent quantum dynamics in the condensed phase, resulting in a value of 60.87 J/mol-K. Comparing the entropy value of MB-pol calculated using MD trajectories in the microcanonical ensemble (60.79 J/mol-K), we can conclude that nuclear quantum effects have a negligible influence on the entropy value calculated using the 2PT model. This observation aligns with the conclusion of statistical mechanics, indicating that entropy contributions from vibrational modes

are typically minor in comparison to those from translational and rotational motions. As a result, the difference in entropy values among all water models can be attributed to the structure and dynamics of water predicted by different water models.

To illuminate the relationship between the structure of water and the calculated entropy values, Figure 6.1 shows the oxygen-oxygen radial distribution function (RDF) calculated with each water model alongside the experimental data. While SPC and TIP3P exhibit the closest entropy values compared to the experiment within their respective families, their RDFs lack prominent long-range structural reorganization, which indicates a poor representation of water structure for the second hydration shell. On the other hand, all other models exhibit similar RDF profiles, providing robust representations of both first and second hydration shells. In particular, MB-pol and MB-pol(2023), which predict similar entropy values, show the closest agreement with the experimental RDF. In addition, the trend of entropy values of water models qualitatively follows the degree of order in the water structure obtained from the corresponding simulations. The high entropy values of SPC and TIP3P are reflected in the absence of structure in their second hydration shell. SPC/E, SPC/Fw, TIP4P/2005, TIP4P/2005f, and TIP4P/Ew exhibit smaller entropy values compared to MB-pol and MB-pol(2023), as their first hydration shells are overstructured but share similarities with MB-pol and MB-pol(2023) for the second hydration shell. Therefore, the superior agreement of entropy values for SPC and TIP3P with the experimental value compared to all other models likely indicates error cancellation between the approximations adopted by the 2PT model and intrinsic limitations of these water models in correctly representing the interactions in liquid water. Additionally, based on the consistency between the predicted water structure of MB-pol and the experiment, we can reasonably assume that, by construction, the 2PT model likely underestimates the entropy value in liquid water by approximately 7 J/mol-K. Furthermore, the trend of predicted entropy values for the various water models qualitatively reflects their ability to predict the structure of liquid water.

The relationship between the structure of water and the entropy is further supported by the analysis of the tetrahedral order parameter calculated using each water model shown in Figure 6.2.

Except for SPC and TIP3P, all water models exhibit a similar distribution, characterized by a small plateau at $q_{tet} \approx 0.5$ and a broad peak at $q_{tet} \approx 0.8$. On the other hand, the q_{tet} distributions calculated with the SPC and TIP3P models display a peak at $q_{tet} \approx 0.5$. The analyses of the RDFs shown in Figure 6.1 and the q_{tet} distribution in Figure 6.2 demonstrate that the SPC and TIP3P models are unable to accurately predict the structure of the first hydration shell, despite providing the closest agreement with the experimental value of the entropy. Moreover, the larger entropy values predicted by the SPC and TIP3P models compared to other models qualitatively align with their q_{tet} distributions, since SPC and TIP3P exhibit a greater portion of smaller q_{tet} values, which correspond to more disordered arrangements. In addition, the slightly higher entropy value predicted by TIP4P compared to MB-pol and MB-pol(2023) can be understood in terms of the differences in the corresponding q_{tet} distributions. Specifically, the q_{tet} distribution calculated with TIP4P is noticeably higher at $q_{tet} \approx 0.5$ and lower at $q_{tet} \approx 0.8$ compared to MB-pol and MB-pol(2023), while its RDF shares features common to all other water models belonging to the TIPnP family.

Further insights into the relations between entropy values and dynamical properties predicted by different water models can be gained by analyzing their orientational correlation functions, as shown in Figure 6.3. Following the same trend displayed by the entropy values, RDFs, and q_{tet} distributions, all water models except for SPC, TIP3P, and TIP4P, share a similar profile in their correlation functions as a function of time. The orientational relaxation time for each water model, τ_2, can be extracted by fitting the long-time decay of the orientational correlation functions to a single exponential function, as listed in Table 6.2. Among all τ_2 values, MB-pol and SPC/E predict the closest agreement with the experimental value, followed by MB-pol(2023), SPC/Fw, TIP4P/2005f, TIP4P/Ew, and TIP5P. Interestingly, while MB-pol and MB-pol(2023) share almost identical predictions in water structures as displayed in Figure 6.1 and Figure 6.2, slight differences in their orientational correlation functions can be observed. In addition, it is noteworthy that models with smaller τ_2 values generally exhibit larger entropy values as shown in Table 6.1. A small τ_2 implies a rapid decay of the correlation function,

indicating that the system quickly becomes uncorrelated with its initial state. Consequently, information about the system is rapidly lost over time. The trend of τ_2 and entropy values among all water models suggests that the entropy predicted by the 2PT model correctly reflects the essence of entropy: a quantity that quantifies the system's information content. Although the 2PT model does not perfectly align the entropy value of each water model based on their agreement with experimental data, it still provides useful insights into the behavior of water as predicted by different water models.

Table 6.1. Entropy values of water models predicted by the 2PT model at 298 K. All entropy values were averaged from 20 independent 50 ps long trajectories in NVT ensemble.

Model	Entropy (J/mol-K)
Experiment[98]	69.95 ± 0.03
MB-pol	62.92 ± 0.34
MB-pol(2023)	62.03 ± 0.49
SPC family	
SPC	66.85 ± 0.27
SPC/E	61.68 ± 0.25
SPC/Fw	61.41 ± 0.42
TIPnP family	
TIP3P	70.57 ± 0.24
TIP4P	64.34 ± 0.23
TIP4P/2005	58.25 ± 0.15
TIP4P/2005f	60.18 ± 0.22
TIP4P/Ew	59.85 ± 0.23
TIP5P	63.45 ± 0.27

Table 6.2. Orientation relaxation times of water models. The relaxation times, τ_2, were obtained by fitting long-time decay of correlation functions to an exponential function $C_2(t) = A\exp(-t/\tau_2)$.

Model	τ_2 (ps)
Experiment[207]	2.5
MB-pol	2.5526 ± 0.0014
MB-pol(2023)	2.7964 ± 0.0013
SPC family	
SPC	1.5257 ± 0.0007
SPC/E	2.5488 ± 0.0012
SPC/Fw	2.9763 ± 0.0015
TIPnP family	
TIP3P	1.0758 ± 0.0009
TIP4P	1.8020 ± 0.0011
TIP4P/2005	3.0603 ± 0.0018
TIP4P/2005f	2.7299 ± 0.0012
TIP4P/Ew	2.7187 ± 0.0013
TIP5P	2.3383 ± 0.0009

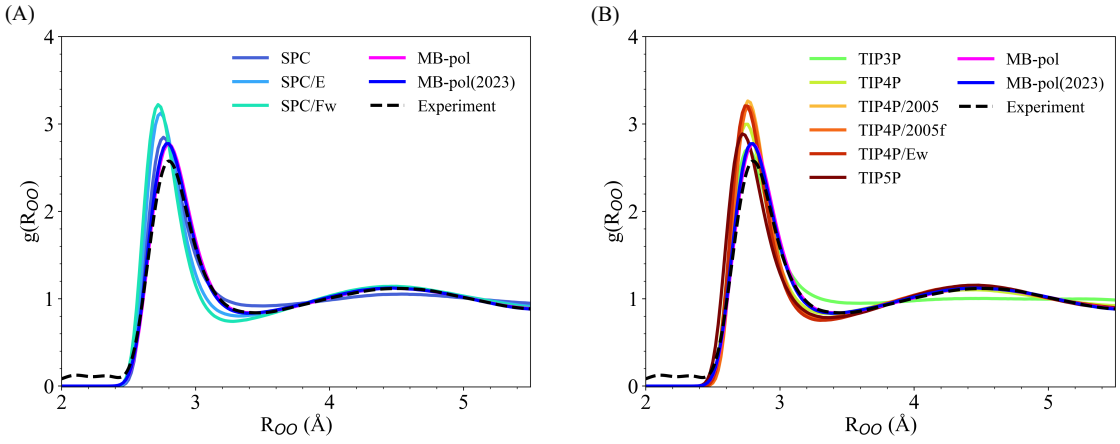

Figure 6.1. The oxygen-oxygen RDFs of MB-pol, MB-pol(2023), and models belonging to (A) SPC family (B) TIPnP family. Experimental data were taken from reference 208.

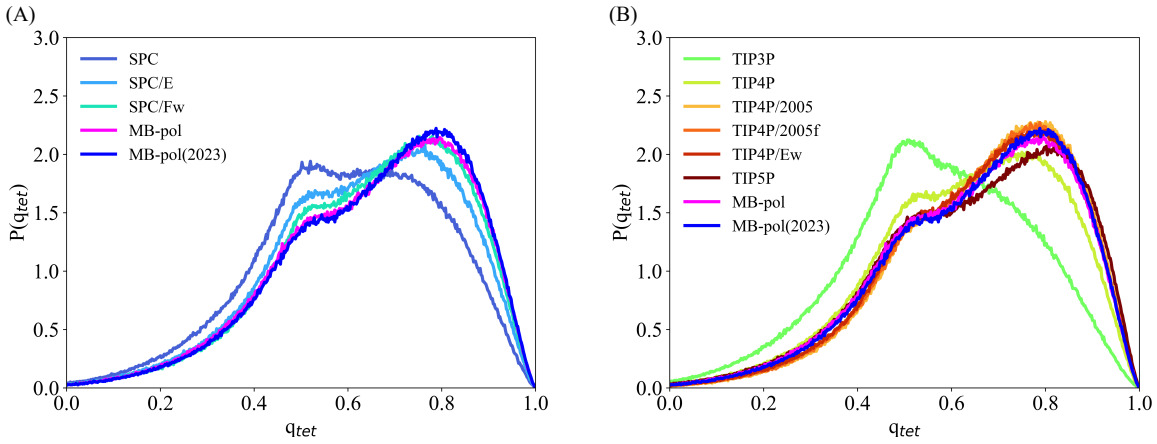

Figure 6.2. Probability distributions of the tetrahedral order parameter, $P(q_{tet})$, of MB-pol, MB-pol(2023), and models belonging to (A) SPC family (B) TIPnP family.

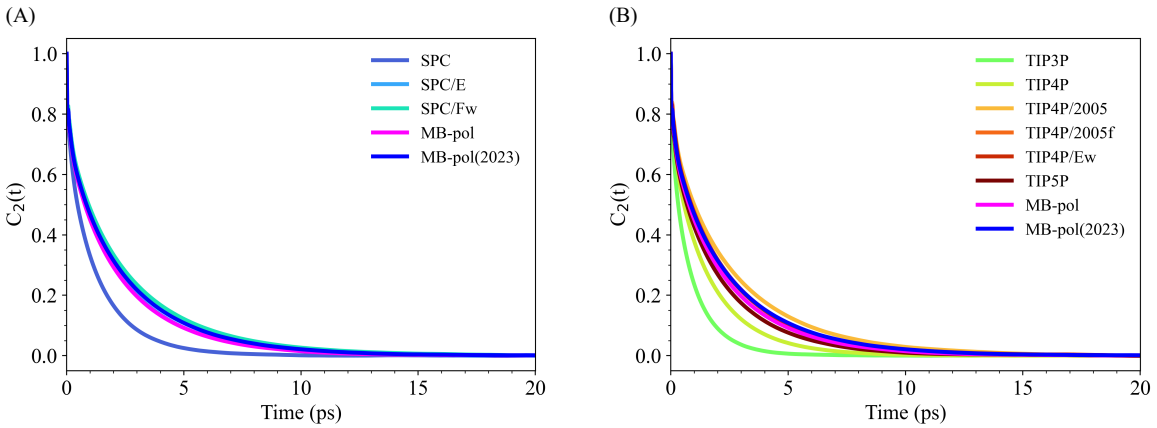

Figure 6.3. Orientational correlation functions of MB-pol, MB-pol(2023), and models belonging to (A) SPC family (B) TIPnP family.

6.4 Conclusions

In this study, we have explored the entropy values of various water models, including MB-pol, MB-pol(2023) and those belonging to the SPC family or TIPnP family, as predicted by the 2PT model. We have demonstrated that the entropy values calculated using the 2PT model qualitatively agree with the extent of ordered structure predicted by water models. Although MB-pol does not exhibit the best agreement with the experimental entropy value, we demonstrate that this discrepancy can be attributed to error cancellation between the formalism of the 2PT model and shortcomings in the ability of simpler water models to correctly predict structural and dynamical properties of water. Despite its simplicity, the 2PT model overall provides reasonable entropy values for water models that predict a robust description of both local structure and dynamics of liquid water at room temperature.

6.5 Acknowledgments

The authors are grateful to Dr. Tod Pascal and Alexandria Do for their insightful discussions at the early stage of this work. This research was supported by the Natural Science Foundation through award no. 2311260. All simulations were carried out on Expanse at the San Diego Supercomputer Center (SDSC) through allocation CHE230052 from the Advanced Cyberinfrastructure Coordination Ecosystem: Services & Support (ACCESS) program, which is supported by NSF grants nos. 2138259, 2138286, 2138307, 2137603, and 2138296, as well as Triton Shared Computing Cluster (TSCC) at SDSC.

6.6 Data availability

Any data generated and analyzed for this study that are not included in the Article are available from the authors upon request.

6.7 Code availability

The molecular models used in the MD simulations are publicly available on GitHub (https://github.com/paesanilab/Data_Repository/tree/main/water_entropy) in the format for LAMMPS or the MBX[112] interface with LAMMPS.[113] All computer codes used in the analysis presented in this study are available from the authors upon request.

Chapter 6, in full, is a reprint of the material as it is being prepared for publication in "Exploring Bulk Water Structure and Entropy Predicted by Two-Phase Thermodynamic Model", C.-H. Ho, F. Paesani. The dissertation author is the primary investigator and author of this paper.

Chapter 7

Conclusion

The emergence of MOFs has opened up new strategies for addressing issues associated with sustainability. Due to their porosity, numerous MOFs have been designed for atmospheric water harvesting to alleviate water scarcity. Additionally, MOFs have been engineered to capture carbon dioxide in order to mitigate carbon emissions. Despite dedicated experimental research efforts, the complex interactions between MOFs and guest molecules have left molecular insights into the adsorption of these molecules somewhat ambiguous. In particular, due to constraints in experimental methodologies, fully decoupling interactions among guest molecules and the framework presents a challenge. This ambiguity hinders the understanding of adsorption mechanisms and reduces the predictability for the rational design of MOFs. Therefore, it is essential to provide molecular insights through simulations to elucidate the behavior of guest molecules in different environments.

NU-1500-Cr is a newly synthesized MOF known for its stability and remarkable capacity in water adsorption. Notably, it exhibits a distinct adsorption step between 30% to 40% relative humidity (RH), indicative of the framework reaching full saturation with water at low RH values. Through molecular dynamics simulations, we have elucidated the thermodynamics of water molecules within the NU-1500-Cr framework, shedding light on the relationship among adsorption enthalpy, water entropy, and adsorption mechanisms. At the pore filling step, the adsorption enthalpy and entropy of water undergo significant changes as water molecules begin

to saturate the main pores in the framework. As these water molecules are relatively far from the framework atoms within the main pores, they do not directly interact with the framework. Additionally, being surrounded by other water molecules, those in the main pores experience stronger constraints in their mobility, resulting in lower entropy values. These observations are further supported by an analysis of the hydrogen-bond topology of water molecules and the distribution of tetrahedral order parameters across different hydration stages. Furthermore, experimental infrared spectra also corroborate our simulation results, as evidenced by the shift of the libration-bending band at different RH values.

CALF-20 is a newly synthesized MOF recognized for its CO_2 capture capability, which is attributed to its impressive stability in the presence of water. While it is experimentally feasible to transition between phases of CALF-20, maintaining a specific phase under ambient conditions poses experimental challenges. However, simulations offer a straightforward approach to studying CO_2 properties within different CALF-20 phases, as these phases can be easily controlled. Our study has demonstrated that phases with smaller unit cell volumes generally exhibit higher affinity to CO_2, albeit at the cost of slower translational mobility for CO_2 molecules.

In addition to studying CO_2 within different phases of CALF-20, we have also investigated the competitive adsorption of water and CO_2 within the same framework. The interplay between water and CO_2 presents significant experimental challenges in assessing how the presence of competitive species affects both thermodynamic and dynamical properties of guest molecules, as the concentration of a species depends on the partial pressures of both species. In our study, we have provided molecular insights into the affinity of water and CO_2 within CALF-20 by investigating their preferred interaction sites within the framework, as well as their binding affinity. We have also revealed specific confining effects induced by the framework on the structural reorganization of water and CO_2 mixtures within CALF-20. Our findings demonstrate that the presence of CO_2 forces water into more confined regions, resulting in a more connected hydrogen-bond network, slower reorientation dynamics, smaller entropy, and slower translational mobility. Conversely, the presence of water leads to a decrease in the

entropy of CO_2, faster reorientation dynamics, and slower translational mobility. These distinct differences in thermodynamic and dynamical properties of water and CO_2 can be primarily attributed to volume exclusion effects induced by the presence of species competing for the same voids spaces.

Ni_2Cl_2BBTQ is a recently synthesized MOF known for its exceptional performance in water harvesting, minimal water hysteresis between adsorption and desorption processes, and a sharp adsorption step at low RH values ($< 5\%$ RH). In our study, we have demonstrated that the distinct behavior of water within Ni_2Cl_2BBTQ and NU-1500-Cr at the early hydration stage can be attributed to differences in the water adsorption mechanisms. In Ni_2Cl_2BBTQ, water molecules are captured at the early hydration stage by unsaturated Ni atoms, leveraging cooperative effects from the organic linkers. Conversely, NU-1500-Cr attracts water molecules that can saturate the open Cr^{3+} sites of the framework. This leads to distinct trends in both thermodynamic and dynamical properties of water adsorbed in the MOF pores as a function of RH.

While calculating the entropy of water has long been recognized as a challenge, the 2PT model offers an approximate yet robust path towards estimating the absolute entropy of a liquid. In our study, we have investigated the entropy values predicted by the 2PT model for several common water models, as well as MB-pol and MB-pol(2023). Our findings demonstrate that the 2PT model is capable of providing semiquantitative entropy values based on the predicted water structure and dynamics at ambient conditions, although it can benefit from error cancellation. Despite its inherent approximations, given its simplicity, the 2PT model serves as a valuable approach for calculating entropy values for water models that can predict reliable water structure and dynamics.

Bibliography

[1] Pall, P.; Aina, T.; Stone, D. A.; Stott, P. A.; Nozawa, T.; Hilberts, A. G.; Lohmann, D.; Allen, M. R. *Nature* **2011**, *470*, 382–385.

[2] Friedlingstein, P.; O'Sullivan, M.; Jones, M. W.; Andrew, R. M.; Hauck, J.; Olsen, A.; Peters, G. P.; Peters, W.; Pongratz, J.; Sitch, S.; Le Quéré, C.; Canadell, J. G.; Ciais, P.; Jackson, R. B.; Alin, S.; Aragão, L. E. O. C.; Arneth, A.; Arora, V.; Bates, N. R.; Becker, M.; Benoit-Cattin, A.; Bittig, H. C.; Bopp, L.; Bultan, S.; Chandra, N.; Chevallier, F.; Chini, L. P.; Evans, W.; Florentie, L.; Forster, P. M.; Gasser, T.; Gehlen, M.; Gilfillan, D.; Gkritzalis, T.; Gregor, L.; Gruber, N.; Harris, I.; Hartung, K.; Haverd, V.; Houghton, R. A.; Ilyina, T.; Jain, A. K.; Joetzjer, E.; Kadono, K.; Kato, E.; Kitidis, V.; Korsbakken, J. I.; Landschützer, P.; Lefèvre, N.; Lenton, A.; Lienert, S.; Liu, Z.; Lombardozzi, D.; Marland, G.; Metzl, N.; Munro, D. R.; Nabel, J. E. M. S.; Nakaoka, S.-I.; Niwa, Y.; O'Brien, K.; Ono, T.; Palmer, P. I.; Pierrot, D.; Poulter, B.; Resplandy, L.; Robertson, E.; Rödenbeck, C.; Schwinger, J.; Séférian, R.; Skjelvan, I.; Smith, A. J. P.; Sutton, A. J.; Tanhua, T.; Tans, P. P.; Tian, H.; Tilbrook, B.; van der Werf, G.; Vuichard, N.; Walker, A. P.; Wanninkhof, R.; Watson, A. J.; Willis, D.; Wiltshire, A. J.; Yuan, W.; Yue, X.; Zaehle, S. *Earth Syst. Sci. Data* **2020**, *12*, 3269–3340.

[3] Howarth, R. W.; Santoro, R.; Ingraffea, A. *Clim. Change* **2011**, *106*, 679–690.

[4] Lüthi, D.; Le Floch, M.; Bereiter, B.; Blunier, T.; Barnola, J.-M.; Siegenthaler, U.; Raynaud, D.; Jouzel, J.; Fischer, H.; Kawamura, K.; Stocker, T. F. *Nature* **2008**, *453*, 379–382.

[5] Bousquet, P.; Ciais, P.; Miller, J.; Dlugokencky, E. J.; Hauglustaine, D.; Prigent, C.; Van der Werf, G.; Peylin, P.; Brunke, E.-G.; Carouge, C.; Langenfelds, R. L.; Lathière, J.; Papa, F.; Ramonet, M.; Schmidt, M.; Steele, L. P.; Tyler, S. C.; White, J. *Nature* **2006**, *443*, 439–443.

[6] Sweet, W. V.; Kopp, R. E.; Weaver, C. P.; Obeysekera, J.; Horton, R. M.; Thieler, E. R.; Zervas, C. *Global and regional sea level rise scenarios for the United States*; 2017.

[7] Saffioti, C.; Fischer, E. M.; Knutti, R. *Geophys. Res. Lett.* **2015**, *42*, 2385–2391.

[8] Van den Broeke, M. R.; Enderlin, E. M.; Howat, I. M.; Kuipers Munneke, P.; Noël, B. P.; Van De Berg, W. J.; Van Meijgaard, E.; Wouters, B. *The Cryosphere* **2016**, *10*, 1933–1946.

[9] Hurst, M. D.; Rood, D. H.; Ellis, M. A.; Anderson, R. S.; Dornbusch, U. *Proc. Natl. Acad. Sci. U.S.A.* **2016**, *113*, 13336–13341.

[10] Piao, S.; Ciais, P.; Huang, Y.; Shen, Z.; Peng, S.; Li, J.; Zhou, L.; Liu, H.; Ma, Y.; Ding, Y.; Friedlingstein, P.; Liu, C.; Tan, K.; Yu, Y.; Zhang, T.; Fang, J. *Nature* **2010**, *467*, 43–51.

[11] Schilling, J.; Freier, K. P.; Hertig, E.; Scheffran, J. *Agric. Ecosyst. Environ.* **2012**, *156*, 12–26.

[12] Krol, M. S.; Bronstert, A. *Environ. Model. Softw.* **2007**, *22*, 259–268.

[13] Carvalho-Santos, C.; Monteiro, A. T.; Azevedo, J. C.; Honrado, J. P.; Nunes, J. P. *Water Resour. Manag.* **2017**, *31*, 3355–3370.

[14] King, A. D.; van Oldenborgh, G. J.; Karoly, D. J.; Lewis, S. C.; Cullen, H. *Environ. Res. Lett.* **2015**, *10*, 054002.

[15] Reed, K. A.; Wehner, M. F.; Zarzycki, C. M. *Nat. Commun.* **2022**, *13*, 1905.

[16] Williams, A. P.; Seager, R.; Abatzoglou, J. T.; Cook, B. I.; Smerdon, J. E.; Cook, E. R. *Geophys. Res. Lett.* **2015**, *42*, 6819–6828.

[17] Zhang, X.; Cai, X. *Environ. Res. Lett.* **2011**, *6*, 014014.

[18] Myers, S. S.; Smith, M. R.; Guth, S.; Golden, C. D.; Vaitla, B.; Mueller, N. D.; Dangour, A. D.; Huybers, P. *Annu. Rev. Public Health* **2017**, *38*, 259–277.

[19] Deryng, D.; Conway, D.; Ramankutty, N.; Price, J.; Warren, R. *Environ. Res. Lett.* **2014**, *9*, 034011.

[20] Ward, P. S.; Florax, R. J.; Flores-Lagunes, A. *Eur. Rev. Agric. Econ.* **2014**, *41*, 199–226.

[21] Frank, D.; Reichstein, M.; Bahn, M.; Thonicke, K.; Frank, D.; Mahecha, M. D.; Smith, P.; van der Velde, M.; Vicca, S.; Babst, F.; Beer, C.; Buchmann, N.; Canadell, J. G.; Ciais, P.; Cramer, W.; Ibrom, A.; Miglietta, F.; Poulter, B.; Rammig, A.; Seneviratne, S. I.; Walz, A.; Wattenbach, M.; Zavala, M. A.; Zscheischler, J. *Glob. Change Biol.* **2015**, *21*, 2861–2880.

[22] Climate change: EU to cut CO_2 emissions by 55% by 2030. 2021; https://www.bbc.com/news/world-europe-56828383, Accessed: April 25 2024.

[23] Smith, B. Microsoft will be carbon negative by 2030. 2020; https://blogs.microsoft.com/

blog/2020/01/16/microsoft-will-be-carbon-negative-by-2030/, Accessed: April 25 2024.

[24] Wang, X.; Alzayer, M.; Shih, A. J.; Bose, S.; Xie, H.; Vornholt, S. M.; Malliakas, C. D.; Alhashem, H.; Joodaki, F.; Marzouk, S.; Xiong, G.; Del Campo, M.; Le Magueres, P.; Formalik, F.; Sengupta, D.; Idrees, K. B.; Ma, K.; Chen, Y.; Kirlikovali, K. O.; Islamoglu, T.; Chapman, K. W.; Snurr, R. Q.; Farha, O. K. *J. Am. Chem. Soc.* **2024**,

[25] Wang, R.; Bukowski, B. C.; Duan, J.; Zhang, K.; Snurr, R. Q.; Hupp, J. T. *ACS Appl. Mater. Interfaces* **2023**, *15*, 51854–51862.

[26] Wei, Y.; Qi, F.; Li, Y.; Min, X.; Wang, Q.; Hu, J.; Sun, T. *RSC Adv.* **2022**, *12*, 18224–18231.

[27] Fei, S.; Alizadeh, A.; Hsu, W.-L.; Delaunay, J.-J.; Daiguji, H. *J. Phys. Chem. C* **2021**, *125*, 26755–26769.

[28] Mileo, P. G.; Ho Cho, K.; Park, J.; Devautour-Vinot, S.; Chang, J.-S.; Maurin, G. *J. Phys. Chem. C* **2019**, *123*, 23014–23025.

[29] Wang, J.; Wolf, R. M.; Caldwell, J. W.; Kollman, P. A.; Case, D. A. *J. Comp. Chem.* **2004**, *25*, 1157–1174.

[30] Rappé, A. K.; Casewit, C. J.; Colwell, K.; Goddard III, W. A.; Skiff, W. M. *J. Am. Chem. Soc.* **1992**, *114*, 10024–10035.

[31] Chai, J.-D.; Head-Gordon, M. *Phys. Chem. Chem. Phys.* **2008**, *10*, 6615–6620.

[32] Weigend, F. *Phys. Chem. Chem. Phys.* **2006**, *8*, 1057–65.

[33] Stone, A. *The theory of intermolecular forces*; oUP oxford, 2013.

[34] Babin, V.; Leforestier, C.; Paesani, F. *J. Chem. Theory Comput.* **2013**, *9*, 5395–5403.

[35] Medders, G. R.; Babin, V.; Paesani, F. *J. Chem. Theory Comput.* **2014**, *10*, 2906–2910.

[36] Babin, V.; Medders, G. R.; Paesani, F. *J. Chem. Theory Comput.* **2014**, *10*, 1599–1607.

[37] Del Bene, J.; Pople, J. *Chem. Phys. Lett.* **1969**, *4*, 426–428.

[38] Ojamaee, L.; Hermansson, K. *J. Phys. Chem.* **1994**, *98*, 4271–4282.

[39] Xantheas, S. S. *J. Chem. Phys.* **1994**, *100*, 7523–7534.

[40] Góra, U.; Podeszwa, R.; Cencek, W.; Szalewicz, K. *J. Chem. Phys.* **2011**, *135*, 224102.

[41] Partridge, H.; Schwenke, D. W. *J. Chem. Phys.* **1997**, *106*, 4618–4639.

[42] Manz, T. A.; Sholl, D. S. *J. Chem. Theory Comput.* **2010**, *6*, 2455–2468.

[43] Henkelman, G.; Arnaldsson, A.; Jónsson, H. *Comput. Mater. Sci.* **2006**, *36*, 354–360.

[44] Marenich, A. V.; Jerome, S. V.; Cramer, C. J.; Truhlar, D. G. *J. Chem. Theory Comput.* **2012**, *8*, 527–541.

[45] Mekonnen, M. M.; Hoekstra, A. Y. **2016**, *2*, e1500323.

[46] Elimelech, M.; Phillip, W. A. *Science* **2011**, *333*, 712–717.

[47] Shannon, M. A.; Bohn, P. W.; Elimelech, M.; Georgiadis, J. G.; Marinas, B. J.; Mayes, A. M. *Nature* **2008**, *452*, 301–310.

[48] Yang, K.; Pan, T.; Lei, Q.; Dong, X.; Cheng, Q.; Han, Y. *Environ. Sci. Technol.* **2021**, *55*, 6542–6560.

[49] Canivet, J.; Fateeva, A.; Guo, Y.; Coasne, B.; Farrusseng, D. *Chem. Soc. Rev.* **2014**, *43*, 5594–5617.

[50] Burtch, N. C.; Jasuja, H.; Walton, K. S. *Chem. Rev.* **2014**, *114*, 10575–10612.

[51] Liu, X.; Wang, X.; Kapteijn, F. *Chem. Rev.* **2020**, *120*, 8303–8377.

[52] Peng, Y.; Huang, H.; Zhang, Y.; Kang, C.; Chen, S.; Song, L.; Liu, D.; Zhong, C. *Nat. Commun.* **2018**, *9*, 1–9.

[53] Li, Z.; Rayder, T. M.; Luo, L.; Byers, J. A.; Tsung, C.-K. *J. Am. Chem. Soc.* **2018**, *140*, 8082–8085.

[54] Furukawa, H.; Gandara, F.; Zhang, Y.-B.; Jiang, J.; Queen, W. L.; Hudson, M. R.; Yaghi, O. M. *J. Am. Chem. Soc.* **2014**, *136*, 4369–4381.

[55] Cadiau, A.; Lee, J. S.; Damasceno Borges, D.; Fabry, P.; Devic, T.; Wharmby, M. T.; Martineau, C.; Foucher, D.; Taulelle, F.; Jun, C.-H.; Hwang, Y. K.; Stock, N.; De Lange, M. F.; Kapteijn, F.; Gascon, J.; Maurin, G.; Chang, J.-S.; Serre, C. *Adv. Mater.* **2015**, *27*, 4775–4780.

[56] Fröhlich, D.; Pantatosaki, E.; Kolokathis, P. D.; Markey, K.; Reinsch, H.; Baumgartner, M.; van der Veen, M. A.; De Vos, D. E.; Stock, N.; Papadopoulos, G. K.; Henninger, S. K.; Janiak, C. *J. Mater. Chem. A* **2016**, *4*, 11859–11869.

[57] Rieth, A. J.; Yang, S.; Wang, E. N.; Dincă, M. *ACS Cent. Sci.* **2017**, *3*, 668–672.

[58] Gao, M.; Wang, J.; Rong, Z.; Shi, Q.; Dong, J. *RSC Adv.* **2018**, *8*, 39627–39634.

[59] Abtab, S. M. T.; Alezi, D.; Bhatt, P. M.; Shkurenko, A.; Belmabkhout, Y.; Aggarwal, H.; Weseliński, Ł. J.; Alsadun, N.; Samin, U.; Hedhili, M. N.; Eddaoudi, M. *Chem* **2018**, *4*, 94–105.

[60] Hanikel, N.; Prévot, M. S.; Fathieh, F.; Kapustin, E. A.; Lyu, H.; Wang, H.; Diercks, N. J.; Glover, T. G.; Yaghi, O. M. *ACS Cent. Sci.* **2019**, *5*, 1699–1706.

[61] Rieth, A. J.; Wright, A. M.; Skorupskii, G.; Mancuso, J. L.; Hendon, C. H.; Dincă, M. *J. Am. Chem. Soc.* **2019**, *141*, 13858–13866.

[62] Chen, Z.; Li, P.; Zhang, X.; Li, P.; Wasson, M. C.; Islamoglu, T.; Stoddart, J. F.; Farha, O. K. *J. Am. Chem. Soc.* **2019**, *141*, 2900–2905.

[63] Jorgensen, W. L.; Chandrasekhar, J.; Madura, J. D.; Impey, R. W.; Klein, M. L. *J. Chem. Phys.* **1983**, *79*, 926–935.

[64] Mahoney, M. W.; Jorgensen, W. L. *J. Chem. Phys.* **2000**, *112*, 8910–8922.

[65] Horn, H. W.; Swope, W. C.; Pitera, J. W.; Madura, J. D.; Dick, T. J.; Hura, G. L.; Head-Gordon, T. *J. Chem. Phys.* **2004**, *120*, 9665–9678.

[66] Berendsen, H.; Grigera, J.; Straatsma, T. *J. Phys. Chem.* **1987**, *91*, 6269–6271.

[67] Berendsen, H. J.; Postma, J. P.; van Gunsteren, W. F.; Hermans, J. *Intermolecular forces*; Springer, 1981; pp 331–342.

[68] Cavka, J. H.; Jakobsen, S.; Olsbye, U.; Guillou, N.; Lamberti, C.; Bordiga, S.; Lillerud, K. P. *J. Am. Chem. Soc.* **2008**, *130*, 13850–13851.

[69] Férey, G.; Mellot-Draznieks, C.; Serre, C.; Millange, F.; Dutour, J.; Surblé, S.; Margiolaki, I. *Science* **2005**, *309*, 2040–2042.

[70] Horcajada, P.; Surblé, S.; Serre, C.; Hong, D.-Y.; Seo, Y.-K.; Chang, J.-S.; Grenèche, J.-M.; Margiolaki, I.; Férey, G. *Chem. Commun.* **2007**, 2820–2822.

[71] Jajko, G.; Gutiérrez-Sevillano, J. J.; Sławek, A.; Szufla, M.; Kozyra, P.; Matoga, D.; Makowski, W.; Calero, S. *Microporous Mesoporous Mater.* **2022**, *330*, 111555.

[72] Grenev, I. V.; Shubin, A. A.; Solovyeva, M. V.; Gordeeva, L. G. *Phys. Chem. Chem. Phys.* **2021**, *23*, 21329–21337.

[73] Dissegna, S.; Epp, K.; Heinz, W. R.; Kieslich, G.; Fischer, R. A. *Adv. Mater. Lett.* **2018**, *30*, 1704501.

[74] Vandichel, M.; Hajek, J.; Ghysels, A.; De Vos, A.; Waroquier, M.; Van Speybroeck, V. *CrystEngComm* **2016**, *18*, 7056–7069.

[75] Ghosh, P.; Colón, Y. J.; Snurr, R. Q. *Chem. Commun.* **2014**, *50*, 11329–11331.

[76] Zhang, C.; Han, C.; Sholl, D. S.; Schmidt, J. *J. Phys. Chem. Lett.* **2016**, *7*, 459–464.

[77] Kresse, G.; Hafner, J. *Phys. Rev. B* **1993**, *47*, 558.

[78] Kresse, G.; Hafner, J. *Phys. Rev. B* **1994**, *49*, 14251.

[79] Kresse, G.; Furthmüller, J. *Comput. Mater. Sci.* **1996**, *6*, 15–50.

[80] Kresse, G.; Furthmüller, J. *Phys. Rev. B* **1996**, *54*, 11169.

[81] Perdew, J. P.; Burke, K.; Ernzerhof, M. *Phys. Rev. Lett.* **1996**, *77*, 3865.

[82] Grimme, S.; Antony, J.; Ehrlich, S.; Krieg, H. *J. Chem. Phys.* **2010**, *132*, 154104.

[83] Blöchl, P. E. *Phys. Rev. B* **1994**, *50*, 17953.

[84] Kresse, G.; Joubert, D. *Phys. Rev. B* **1999**, *59*, 1758.

[85] Frisch, M. J.; Trucks, G. W.; Schlegel, H. B.; Scuseria, G. E.; Robb, M. A.; Cheeseman, J. R.; Scalmani, G.; Barone, V.; Petersson, G. A.; Nakatsuji, H.; Li, X.; Caricato, M.; Marenich, A. V.; Bloino, J.; Janesko, B. G.; Gomperts, R.; Mennucci, B.; Hratchian, H. P.; Ortiz, J. V.; Izmaylov, A. F.; Sonnenberg, J. L.; Williams-Young, D.; Ding, F.; Lipparini, F.; Egidi, F.; Goings, J.; Peng, B.; Petrone, A.; Henderson, T.; Ranasinghe, D.; Zakrzewski, V. G.; Gao, J.; Rega, N.; Zheng, G.; Liang, W.; Hada, M.; Ehara, M.; Toyota, K.; Fukuda, R.; Hasegawa, J.; Ishida, M.; Nakajima, T.; Honda, Y.; Kitao, O.; Nakai, H.; Vreven, T.; Throssell, K.; Montgomery, J. A., Jr.; Peralta, J. E.; Ogliaro, F.; Bearpark, M. J.; Heyd, J. J.; Brothers, E. N.; Kudin, K. N.; Staroverov, V. N.; Keith, T. A.; Kobayashi, R.; Normand, J.; Raghavachari, K.; Rendell, A. P.; Burant, J. C.; Iyengar, S. S.; Tomasi, J.; Cossi, M.; Millam, J. M.; Klene, M.; Adamo, C.; Cammi, R.; Ochterski, J. W.; Martin, R. L.; Morokuma, K.; Farkas, O.; Foresman, J. B.; Fox, D. J. Gaussian 16 Revision C.01. 2016; Gaussian Inc. Wallingford CT.

[86] Paesani, F. *Acc. Chem. Res.* **2016**, *49*, 1844–1851.

[87] Reddy, S. K.; Straight, S. C.; Bajaj, P.; Pham, C. H.; Riera, M.; Moberg, D. R.; Morales, M. A.; Knight, C.; Götz, A. W.; Paesani, F. *J. Chem. Phys.* **2016**, *145*, 194504.

[88] Vega, C.; Abascal, J. L. *Phys. Chem. Chem. Phys.* **2011**, *13*, 19663–19688.

[89] Martyna, G. J.; Klein, M. L.; Tuckerman, M. *J. Chem. Phys.* **1992**, *97*, 2635–2643.

[90] Ewald, P. P. *Ann. Phys.* **1921**, *369*, 253–287.

[91] Martínez, L.; Andrade, R.; Birgin, E. G.; Martínez, J. M. *J. Comput. Chem.* **2009**, *30*, 2157–2164.

[92] Martínez, J. M.; Martínez, L. *J. Comput. Chem.* **2003**, *24*, 819–825.

[93] Lin, S.-T.; Maiti, P. K.; Goddard III, W. A. *J. Phys. Chem. B* **2010**, *114*, 8191–8198.

[94] Medders, G. R.; Paesani, F. *J. Chem. Theory Comput.* **2015**, *11*, 1145–1154.

[95] Hunter, K. M.; Wagner, J. C.; Kalaj, M.; Cohen, S. M.; Xiong, W.; Paesani, F. *J. Phys. Chem. C* **2021**, *125*, 12451–12460.

[96] Jeremias, F.; Fröhlich, D.; Janiak, C.; Henninger, S. K. *RSC Adv.* **2014**, *4*, 24073–24082.

[97] Tannert, N.; Ernst, S.-J.; Jansen, C.; Bart, H.-J.; Henninger, S. K.; Janiak, C. *J. Mater. Chem. A* **2018**, *6*, 17706–17712.

[98] Mallard, W. *http://webbook. nist. gov* **2000**, *69*.

[99] Jeremias, F.; Lozan, V.; Henninger, S. K.; Janiak, C. *Dalton Trans.* **2013**, *42*, 15967–15973.

[100] Rieth, A. J.; Hunter, K. M.; Dincă, M.; Paesani, F. *Nat. Commun.* **2019**, *10*, 1–7.

[101] Bae, J.; Park, S. H.; Moon, D.; Jeong, N. C. *Commun. Chem.* **2022**, *5*, 51.

[102] Wagner, J. C.; Hunter, K. M.; Paesani, F.; Xiong, W. *J. Am. Chem. Soc.* **2021**, *143*, 21189–21194.

[103] Ajala, A. O.; Voora, V.; Mardirossian, N.; Furche, F.; Paesani, F. *J. Chem. Theory Comput.* **2019**, *15*, 2359–2374.

[104] Gartner III, T. E.; Hunter, K. M.; Lambros, E.; Caruso, A.; Riera, M.; Medders, G. R.; Panagiotopoulos, A. Z.; Debenedetti, P. G.; Paesani, F. *J. Phys. Chem. Lett.* **2022**, *13*, 3652–3658.

[105] Errington, J. R.; Debenedetti, P. G. *Nature* **2001**, *409*, 318–321.

[106] Verma, P. K.; Kundu, A.; Puretz, M. S.; Dhoonmoon, C.; Chegwidden, O. S.; Londergan, C. H.; Cho, M. *J. Phys. Chem. B* **2017**, *122*, 2587–2599.

[107] Moilanen, D. E.; Fenn, E. E.; Wong, D.; Fayer, M. *J. Phys. Chem. B* **2009**, *113*, 8560–8568.

[108] Liang, C.; Jeon, J.; Cho, M. *J. Phys. Chem. Lett.* **2019**, *10*, 1153–1158.

[109] Hack, J. H.; Dombrowski, J. P.; Ma, X.; Chen, Y.; Lewis, N. H.; Carpenter, W. B.; Li, C.; Voth, G. A.; Kung, H. H.; Tokmakoff, A. *J. Am. Chem. Soc.* **2021**, *143*, 10203–10213.

[110] Yan, C.; Nishida, J.; Yuan, R.; Fayer, M. D. *J. Am. Chem. Soc.* **2016**, *138*, 9694–9703.

[111] Libowitzky, E. *Monatsh. Chem.* **1999**, *130*, 1047–1059.

[112] MBX v1.0. http://paesanigroup.ucsd.edu/software/mbx.html, 2023; Accessed: April 25 2024.

[113] Thompson, A. P.; Aktulga, H. M.; Berger, R.; Bolintineanu, D. S.; Brown, W. M.; Crozier, P. S.; in 't Veld, P. J.; Kohlmeyer, A.; Moore, S. G.; Nguyen, T. D.; Shan, R.; Stevens, M. J.; Tranchida, J.; Trott, C.; Plimpton, S. J. *Comput. Phys. Commun.* **2022**, *271*, 108171.

[114] Keith, D. W. *Science* **2009**, *325*, 1654–1655.

[115] Sanz-Pérez, E. S.; Murdock, C. R.; Didas, S. A.; Jones, C. W. *Chem. Rev.* **2016**, *116*, 11840–11876.

[116] Erans, M.; Sanz-Pérez, E. S.; Hanak, D. P.; Clulow, Z.; Reiner, D. M.; Mutch, G. A. *Energy Environ. Sci.* **2022**, *15*, 1360–1405.

[117] Darunte, L. A.; Oetomo, A. D.; Walton, K. S.; Sholl, D. S.; Jones, C. W. *ACS Sustain. Chem. Eng.* **2016**, *4*, 5761–5768.

[118] Kumar, A.; Madden, D. G.; Lusi, M.; Chen, K.-J.; Daniels, E. A.; Curtin, T.; Perry IV, J. J.; Zaworotko, M. J. *Angew. Chem. Int. Ed.* **2015**, *54*, 14372–14377.

[119] Rayder, T. M.; Formalik, F.; Vornholt, S. M.; Frank, H.; Lee, S.; Alzayer, M.; Chen, Z.; Sengupta, D.; Islamoglu, T.; Paesani, F.; Chapman, K. W.; Snurr, R. Q.; Farha, O. K. *J. Am. Chem. Soc.* **2023**, *145*, 11195–11205.

[120] Bhatt, P. M.; Belmabkhout, Y.; Cadiau, A.; Adil, K.; Shekhah, O.; Shkurenko, A.; Barbour, L. J.; Eddaoudi, M. *J. Am. Chem. Soc.* **2016**, *138*, 9301–9307.

[121] Mukherjee, S.; Sikdar, N.; O'Nolan, D.; Franz, D. M.; Gascón, V.; Kumar, A.; Kumar, N.;

Scott, H. S.; ; Madden, D. G.; Kruger, P. E.; Space, B.; Zaworotko, M. J. *Sci. Adv.* **2019**, *5*, eaax9171.

[122] Cui, X.; Chen, K.; Xing, H.; Yang, Q.; Krishna, R.; Bao, Z.; Wu, H.; Zhou, W.; Dong, X.; Han, Y.; Li, B.; Ren, Q.; Zaworotko, M. J.; Chen, B. *Science* **2016**, *353*, 141–144.

[123] Lin, J.-B.; Nguyen, T. T. T.; Vaidhyanathan, R.; Burner, J.; Taylor, J. M.; Durekova, H.; Akhtar, F.; Mah, R. K.; Ghaffari-Nik, O.; Marx, S.; Fylstra, N.; Iremonger, S. S.; Dawson, K. W.; Sarkar, P.; Hovington, P.; Rajendran, A.; Woo, T. K.; Shimizu, G. K. H. *Science* **2021**, *374*, 1464–1469.

[124] Riera, M.; Yeh, E. P.; Paesani, F. *J. Chem. Theory Comput.* **2020**, *16*, 2246–2257.

[125] Yue, S.; Riera, M.; Ghosh, R.; Panagiotopoulos, A. Z.; Paesani, F. *J. Chem. Phys.* **2022**, *156*, 104503.

[126] Potoff, J. J.; Siepmann, J. I. *AIChE J.* **2001**, *47*, 1676–1682.

[127] Ford, D. C.; Dubbeldam, D.; Snurr, R. Q.; Künzel, V.; Wehring, M.; Stallmach, F.; Kärger, J.; Müller, U. *J. Phys. Chem. Lett.* **2012**, *3*, 930–933.

[128] Pachauri, R. K.; Allen, M. R.; Barros, V. R.; Broome, J.; Cramer, W.; Christ, R.; Church, J. A.; Clarke, L.; Dahe, Q.; Dasgupta, P.; Dubash, N. K.; Edenhofer, O.; Elgizouli, I.; Field, C. B.; Forster, P.; Friedlingstein, P.; Fuglestvedt, J.; Gomez-Echeverri, L.; Hallegatte, S.; Hegerl, G.; Howden, M.; Jiang, K.; Cisneroz, B. J.; Kattsov, V.; Lee, H.; Mach, K. J.; Marotzke, J.; Mastrandrea, M. D.; Meyer, L.; Minx, J.; Mulugetta, Y.; O'Brien, K.; Oppenheimer, M.; Pereira, J. J.; Pichs-Madruga, R.; Plattner, G.-K.; Pörtner, H.-O.; Power, S. B.; Preston, B.; Ravindranath, N. H.; Reisinger, A.; Riahi, K.; Rusticucci, M.; Scholes, R.; Seyboth, K.; Sokona, Y.; Stavins, R.; Stocker, T. F.; Tschakert, P.; van Vuuren, D.; van Ypserle, J.-P. *Climate Change 2014: Synthesis Report. Contribution of Working Groups I, II and III to the Fifth Assessment Report of the Intergovernmental Panel on Climate Change*; IPCC, 2014.

[129] Lessio, M.; Senftle, T. P.; Carter, E. A. *ChemSusChem* **2018**, *11*, 1558–1566.

[130] Zhang, S.; Fan, Q.; Xia, R.; Meyer, T. J. *Acc. Chem. Res.* **2020**, *53*, 255–264.

[131] Bachu, S. *Prog. Energy Combust. Sci.* **2008**, *34*, 254–273.

[132] Gaus, I. *Int. J. Greenh. Gas Control* **2010**, *4*, 73–89.

[133] Soltanian, M. R.; Dai, Z. *Geomech. Geophys. Geo-Energy Geo-Resour.* **2017**, *3*, 221–223.

[134] Castelletto, N.; Gambolati, G.; Teatini, P. *J. Geophys. Res. Solid Earth* **2013**, *118*, 2417–

2428.

[135] Salvi, B. L.; Jindal, S. *SN Appl. Sci.* **2019**, *1*, 1–20.

[136] Caskey, S. R.; Wong-Foy, A. G.; Matzger, A. J. *J. Am. Chem. Soc.* **2008**, *130*, 10870–10871.

[137] Elsaidi, S. K.; Mohamed, M. H.; Schaef, H. T.; Kumar, A.; Lusi, M.; Pham, T.; Forrest, K. A.; Space, B.; Xu, W.; Halder, G. J.; Liu, J.; Zaworotko, M. J.; Thallapally, P. K. *Chem. Comm.* **2015**, *51*, 15530–15533.

[138] Forrest, K. A.; Pham, T.; Elsaidi, S. K.; Mohamed, M. H.; Thallapally, P. K.; Zaworotko, M. J.; Space, B. *Cryst. Growth Des.* **2019**, *19*, 3732–3743.

[139] Fracaroli, A. M.; Furukawa, H.; Suzuki, M.; Dodd, M.; Okajima, S.; Gándara, F.; Reimer, J. A.; Yaghi, O. M. *J. Am. Chem. Soc.* **2014**, *136*, 8863–8866.

[140] DeCoste, J. B.; Peterson, G. W.; Schindler, B. J.; Killops, K. L.; Browe, M. A.; Mahle, J. J. *J. Mater. Chem. A* **2013**, *1*, 11922–11932.

[141] Nguyen, T. T.; Lin, J.-B.; Shimizu, G. K.; Rajendran, A. *Chem. Eng. J.* **2022**, *442*, 136263.

[142] Al-Attas, T.; Nabil, S. K.; Zeraati, A. S.; Shiran, H. S.; Alkayyali, T.; Zargartalebi, M.; Tran, T.; Marei, N. N.; Al Bari, M. A.; Lin, H.; Roy, S.; Ajayan, P. M.; Sinton, D.; Shimizu, G.; Kibria, M. G. *ACS Energy Lett.* **2022**, *8*, 107–115.

[143] Nguyen, T. T.; Shimizu, G. K.; Rajendran, A. *Chem. Eng. J.* **2023**, *452*, 139550.

[144] Liu, A.; Peng, X.; Jin, Q.; Jain, S. K.; Vicent-Luna, J. M.; Calero, S.; Zhao, D. *ACS Appl. Mater. Interfaces* **2019**, *11*, 4686–4700.

[145] Skoulidas, A. I.; Sholl, D. S. *J. Phys. Chem. B* **2005**, *109*, 15760–15768.

[146] Ho, C.-H.; Valentine, M. L.; Chen, Z.; Xie, H.; Farha, O.; Xiong, W.; Paesani, F. *Commun. Chem.* **2023**, *6*, 70.

[147] Bore, S. L.; Paesani, F. *Nat. Commun.* **2023**, *14*, 3349.

[148] Terranova, Z. L.; Paesani, F. *Phys. Chem. Chem. Phys.* **2016**, *18*, 8196–8204.

[149] Shukla, P. B.; Johnson, J. K. *J. Phys. Chem. C* **2022**, *126*, 17699–17711.

[150] Yue, S.; Oh, C.; Nandy, A.; Terrones, G. G.; Kulik, H. J. *Mol. Syst. Des. Eng.* **2023**, *8*, 527–537.

[151] Grosch, J. S.; Paesani, F. *J. Am. Chem. Soc.* **2012**, *134*, 4207–4215.

[152] D.L. Carroll's FORTRAN Genetic Algorithm Driver v1.7a. https://cuaerospace.com/products-services/genetic-algorithm, 2001; Accessed: April 25 2024.

[153] Goldberg, D. E. *Genetic Algorithms in Search, Optimization and Machine Learning*, 1st ed.; Addison-Wesley Longman Publishing Co., Inc.: USA, 1989.

[154] Bureekaew, S.; Amirjalayer, S.; Tafipolsky, M.; Spickermann, C.; Roy, T. K.; Schmid, R. *physica status solidi (b)* **2013**, *250*, 1128–1141.

[155] Abascal, J. L. F.; Vega, C. *J. Chem. Phys.* **2005**, *123*, 234505.

[156] Medders, G. R.; Paesani, F. *J. Chem. Phys.* **2015**, *142*, 212411.

[157] Shinoda, W.; Shiga, M.; Mikami, M. *Phys. Rev. B* **2004**, *69*, 134103.

[158] Simmonett, A. C.; Brooks, B. R. *J. Chem. Phys.* **2021**, *154*.

[159] Simmonett, A. C.; Brooks, B. R. *J. Chem. Phys.* **2021**, *154*.

[160] Kubo, R. *J. Phys. Soc. Jpn.* **1957**, *12*, 570–586.

[161] Bakker, H.; Skinner, J. *Chem. Rev.* **2010**, *110*, 1498–1517.

[162] Terranova, Z. L.; Agee, M. M.; Paesani, F. *J. Phys. Chem. C* **2015**, *119*, 18239–18247.

[163] Valentine, M. L.; Yin, G.; Oppenheim, J. J.; Dincă, M.; Xiong, W. *J. Am. Chem. Soc.* **2023**, *142*, 212411.

[164] Eder, G.; Kloft, S.; Martsinovich, N.; Mahata, K.; Schmittel, M.; Heckl, W. M.; Lackinger, M. *Langmuir* **2011**, *27*, 13563–13571.

[165] Cheng, K.-Y.; Lee, S.-L.; Kuo, T.-Y.; Lin, C.-H.; Chen, Y.-C.; Kuo, T.-H.; Hsu, C.-C.; Chen, C.-h. *Langmuir* **2018**, *34*, 5416–5421.

[166] Zhang, B.; Zhu, Z.; Wang, X.; Liu, X.; Kapteijn, F. *Adv. Funct. Mater.* **2023**, 2304788.

[167] Lu, F.-F.; Gu, X.-W.; Wu, E.; Li, B.; Qian, G. *J. Mater. Chem. A* **2023**, *11*, 1246–1255.

[168] Zheng, Z.; Hanikel, N.; Lyu, H.; Yaghi, O. M. *J. Am. Chem. Soc.* **2022**, *144*, 22669–22675.

[169] Hanikel, N.; Pei, X.; Chheda, S.; Lyu, H.; Jeong, W.; Sauer, J.; Gagliardi, L.; Yaghi, O. M. *Science* **2021**, *374*, 454–459.

[170] Rieth, A. J.; Wright, A. M.; Dincă, M. *Nat. Rev. Mater.* **2019**, *4*, 708–725.

[171] Rieth, A. J.; Wright, A. M.; Rao, S.; Kim, H.; LaPotin, A. D.; Wang, E. N.; Dinca, M. *J. Am. Chem. Soc.* **2018**, *140*, 17591–17596.

[172] Wright, A. M.; Rieth, A. J.; Yang, S.; Wang, E. N.; Dincă, M. *Chem. Sci.* **2018**, *9*, 3856–3859.

[173] Alezi, D.; Oppenheim, J. J.; Sarver, P. J.; Iliescu, A.; Dinakar, B.; Dincă, M. *J. Am. Chem. Soc.* **2023**, *145*, 25233–25241.

[174] Bunzen, H.; Grzywa, M.; Aljohani, R.; Krug von Nidda, H.-A.; Volkmer, D. *Eur. J. Inorg. Chem.* **2019**, *2019*, 4471–4476.

[175] Bunzen, H.; Javed, A.; Klawinski, D.; Lamp, A.; Grzywa, M.; Kalytta-Mewes, A.; Tiemann, M.; von Nidda, H.-A. K.; Wagner, T.; Volkmer, D. *ACS Appl. Nano Mater.* **2018**, *2*, 291–298.

[176] Tong, L.; Chen, Q.; Wong, A. A.; Gómez-Bombarelli, R.; Aspuru-Guzik, A.; Gordon, R. G.; Aziz, M. J. *Phys. Chem. Chem. Phys.* **2017**, *19*, 31684–31691.

[177] Thommes, M.; Kaneko, K.; Neimark, A. V.; Olivier, J. P.; Rodriguez-Reinoso, F.; Rouquerol, J.; Sing, K. S. *Pure Appl. Chem.* **2015**, *87*, 1051–1069.

[178] Fuchs, A.; Knechtel, F.; Wang, H.; Ji, Z.; Wuttke, S.; Yaghi, O. M.; Ploetz, E. *J. Am. Chem. Soc.* **2023**, *145*, 14324–14334.

[179] AbdulHalim, R. G.; Bhatt, P. M.; Belmabkhout, Y.; Shkurenko, A.; Adil, K.; Barbour, L. J.; Eddaoudi, M. *J. Am. Chem. Soc.* **2017**, *139*, 10715–10722.

[180] Beaton, C. Heat Exchanger Design Handbook. 1986.

[181] Bezrukov, A. A.; O'Hearn, D. J.; Gascón-Pérez, V.; Darwish, S.; Kumar, A.; Sanda, S.; Kumar, N.; Francis, K.; Zaworotko, M. J. *Cell Rep. Phys. Sci.* **2023**, *4*, 101252.

[182] Porto, S. d. S. *J. Opt. Soc. Am.* **1966**, *56*, 1585–1589.

[183] Bernstein, H. *Philos. Trans. R. Soc. A* **1979**, *293*, 287–302.

[184] Silbey, R. J.; Alberty, R. A.; Papadantonakis, G. A.; Bawendi, M. G. *Physical chemistry*; John Wiley & Sons, 2022.

[185] Metiu, H. *Physical chemistry: kinetics*; Taylor & Francis, 2006.

[186] Avinery, R.; Kornreich, M.; Beck, R. *Phys. Rev. Lett.* **2019**, *123*, 178102.

[187] Reynolds, C. H.; Holloway, M. K. *ACS Med. Chem. Lett.* **2011**, *2*, 433–437.

[188] Dubey, A.; Takeuchi, K.; Reibarkh, M.; Arthanari, H. *J. Biomol. NMR* **2020**, *74*, 479–498.

[189] Chen, W.; Chang, C.-E.; Gilson, M. K. *Biophys. J.* **2004**, *87*, 3035–3049.

[190] Lin, S.-T.; Blanco, M.; Goddard III, W. A. *J. Chem. Phys.* **2003**, *119*, 11792–11805.

[191] Pascal, T. A.; Schärf, D.; Jung, Y.; Kühne, T. D. *J. Chem. Phys.* **2012**, *137*, 244507.

[192] Ho, C.-H.; Paesani, F. *ACS Appl. Mater. Interfaces* **2023**, *15*, 48287–48295.

[193] Zhang, J.; Paesani, F.; Lessio, M. *J. Mater. Chem. C* **2023**, *11*, 10247–10258.

[194] Frank, H. O.; Paesani, F. *J. Chem. Phys.* **2024**, *160*, 094703.

[195] Zhu, X.; Riera, M.; Bull-Vulpe, E. F.; Paesani, F. *J. Chem. Theory Comput.* **2023**, *19*, 3551–3566.

[196] Zhou, K.-G.; Vasu, K.; Cherian, C.; Neek-Amal, M.; Zhang, J. C.; Ghorbanfekr-Kalashami, H.; Huang, K.; Marshall, O.; Kravets, V.; Abraham, J.; Su, Y.; Grigorenko, A. N.; Pratt, A.; Geim, A. K.; Peeters, F. M.; Novoselov, K. S.; Nair, R. R. *Nature* **2018**, *559*, 236–240.

[197] Zeron, I.; Abascal, J.; Vega, C. *J. Chem. Phys.* **2019**, *151*, 134504.

[198] Mathew, C.; Weiß, R. G.; Giese, C.; Lin, C.-w.; Losfeld, M.-E.; Glockshuber, R.; Riniker, S.; Aebi, M. *RSC Chem. Biol.* **2021**, *2*, 917–931.

[199] Kav, B.; Grafmüller, A.; Schneck, E.; Weikl, T. R. *Nanoscale* **2020**, *12*, 17342–17353.

[200] Kav, B.; Weikl, T. R.; Schneck, E. *J. Phys. Chem. B* **2023**, *127*, 4081–4089.

[201] Grotz, K. K.; Schwierz, N. *J. Chem. Theory Comput.* **2021**, *18*, 526–537.

[202] Srivastava, A.; Malik, S.; Debnath, A. *Chem. Phys.* **2019**, *525*, 110396.

[203] Conde, M.; Rovere, M.; Gallo, P. *J. Mol. Liq.* **2018**, *261*, 513–519.

[204] Wu, Y.; Tepper, H. L.; Voth, G. A. *J. Chem. Phys.* **2006**, *124*, 024503.

[205] González, M. A.; Abascal, J. L. *J. Chem. Phys.* **2011**, *135*, 224516.

[206] Tuckerman, M. E. *Statistical mechanics: theory and molecular simulation*; Oxford university press, 2023.

[207] Rezus, Y.; Bakker, H. *J. Chem. Phys.* **2005**, *123*, 114502.

[208] Skinner, L. B.; Huang, C.; Schlesinger, D.; Pettersson, L. G.; Nilsson, A.; Benmore, C. J. *J. Chem. Phys.* **2013**, *138*, 074506.